Low Aspect Ratio Wing Flow Control at Low Reynolds Numbers

vorgelegt von
Dipl.-Ing.
Stefan Vey
aus Bad Soden am Taunus

von der Fakultät V — Verkehrs- und Maschinensysteme
der Technischen Universität Berlin
zur Erlangung des akademischen Grades

Doktor der Ingenieurwissenschaften
– Dr.-Ing. –

genehmigte Dissertation

Promotionsausschuss:

Vorsitzender:	Prof. Dr.-Ing. J. Thorbeck
Berichter:	Prof. Dr.-Ing. C.O. Paschereit
Berichter:	Prof. D. Greenblatt
Berichter:	Asst. Prof. K. Taira

Tag der wissenschaftlichen Aussprache: 21. November 2013

Berlin 2014
D 83

CONTENTS

Nomenclature

a	temporal coefficient (POD)
α	angle of attack [deg]
α'	corresponding AoA for AR-reduction [deg]
α_{stall}	stall angle of attack [deg]
A	wing area [m^2]
AR	aspect ratio [-]
AR_s	semispan aspect ratio [-]
b_{act}	actuator length [m]
b	wing span [m]
b_s	semispan [m]
b_{act}	length of actuator [m]
β	yaw angle [deg]
c	chord length [m]
C_L	lift coefficient [-]
$C_{L,\max}$	lift coefficient at α_{stall} [-]
$C_{L\alpha}$	$= \mathrm{d}C_L/\mathrm{d}\alpha$, lift curve slope [1/rad]
C_D	drag coefficient [-]
C_N	normal force coefficient [-]
C_μ	momentum coefficient [-]
d	electrode overlap [mm]
d_h	hydraulic diameter [m]
DBD	dielectric barrier discharge
ϵ	trajectory angle [rad]
dc	duty cycle [%]
f_{mod}	forcing/modulation frequency [Hz]
f_{ion}	ionization frequency [kHz]
F	normalized thrust [N/km]
F^+	$f \cdot c/U_\infty$, reduced forcing frequency [-]
F^*	$F^+ \cdot \sin(\alpha)$, reduced forcing frequency [-]

F_D	drag force [N]
F_L	lift force [N]
F_N	normal force [N]
F_T	tangential force [N]
h_G	Gurney flap height [% c]
HV	high voltage
k^*	total (turbulent) kinetic energy [m^2/s^2]
k'	incoherent kinetic energy [m^2/s^2]
$\tilde{k}$	coherent kinetic energy [m^2/s^2]
L	actuator length [m]
$\Delta\Phi$	Phase shift angle [deg]
P_{el}	normalized electric power [W/m]
$P_{el,bm}$	normalized electric power in burst mode [W/m]
R	shunt resistor [Ω]
Re	Reynolds number [-]
St	Strouhal number [-]
t	wing thickness [m]
Tu	turbulence level [%]
U_∞	freestream velocity [m/s]
$U_{\infty,t}$	tangential velocity component [m/s]
$U_{\infty,n}$	normal velocity component [m/s]
U_s	separation velocity [m/s]
U_Φ	phase velocity [m/s]
$U(t)$	high voltage applied to DBD [V]
$U_R(t)$	voltage drop accross resistor [V]
V_{p2p}	peak-to-peak voltage [kV]
LE	leading edge
TE	trailing edge
WT	wing tip
Ψ_POD	phase angle of POD snapshot [rad]
Φ	basis vector (POD)
ρ_∞	freestream air density [kg/m^3]
σ	singular value (POD)

LIST OF FIGURES

LIST OF TABLES

1. INTRODUCTION

Past research in the field of low aspect ratio wing aerodynamics was mainly focused on delta wing configurations at high Reynolds and Mach numbers. Practical application was seen for these kind of wing configurations in the field of civilian (Concorde, TU-144) as well as numerous military airplanes. Historically there has been little to no interest in low aspect ratio wings operating at low flight Reynolds numbers. Since the advent of micro air vehicles (MAVs) a growing interest in the topic can be observed. MAVs are mainly used for surveillance, law enforcement assistance, inspection of confined spaces, and environmental data sampling. The advancing miniaturization of electronic components, power supplies, and electrical motors sped up the development of ever smaller flying vehicles. The reduction in size necessarily leads to the adoption of low aspect ratio wing configurations in an attempt to maximize the lift-generating surface – the geometrical optimum shape being the circular wing. In contrast to conventional high aspect ratio wings, the tip vortices dominate the flow field of low aspect ratio wings. The superposed velocity field of the tip vortices generates a down-wash above the wing, in-between the vortices. This has several effects: the lift curve slope $C_{L,\alpha}$ is reduced compared to higher aspect ratio wings, a smaller maximum lift $C_{L,\max}$ is obtained, and the stall angle of attack α_{stall} shifts towards higher angles. Defining a *low aspect ratio* is somewhat arbitrary, commonly AR ≤ 3 is defined as the boundary.

The operational envelope of micro air vehicles is characterized by extended periods of low speed flight, such as circling a certain location for prolonged time and low speed loitering. Additionally, speed for takeoff and landing should be as low as possible, yet a certain stall margin should be retained. In order to extend the operational envelope to these low speed, high α regions hinged, moving control surfaces in the form of flaps and slats are attached to the wings. These control surfaces add a weight penalty to the vehicle which could be avoided by utilizing

modern flow control methods. Of the many known flow control methods a simple, integrateable technique should be chosen. Carrying heavy tanks of pressurized air or chemicals to supply the actuators does not seem practical. An interesting alternative actuator type has become popular and widely distributed in recent years within the flow control research community: the dielectric barrier discharge (DBD) actuator, also termed *plasma actuator* in popular culture. This actuator type combines several advantages compared to other actuators. Among others these include: lack of moving parts, highly intergrateable, instantaneous response to input signals, wide operating frequency range, and low power consumption. Its flexibility in terms of geometrical shape and adaptability to complex surfaces, combined with its retrofittability to existing structures or wind tunnel models make it a predestined actuator for experimental flow control studies. For example the forcing location can be varied on a wind tunnel model without the need to build a whole new model. Furthermore the complexity of wind tunnel models can be highly reduced as practically no internal fittings are required to operate the actuator, leaving more space for installing measurement equipment. However, where there is light, there is also shadow: currently only relatively small velocities can be induced by this kind of actuator, the high voltage generator needs to be further miniaturized in order to be economically integrated into a MAV, the durability of the dielectric material (here: Kapton®) needs to be improved, and the high-voltages involved in the actuator operation could cause electromagnetic interference (EMI). Nonetheless in the field of basic research the overall balance is positive and a variety of different flow control parameters can be comfortably studied using DBDs. This includes the variation of actuation location, amplitude, and frequency (including continuous actuator operation).

2. OBJECTIVES & SCOPE OF THE THESIS

The overall goal was to maximize the lift increase ΔC_L as well as the stall angle of attack α_{stall} of low aspect ratio wings through periodic excitation of the flow at the leading edge, trailing edge, and wing tip, respectively. The driving control parameters are identified and the effect of actuation on the flow field variables is studied in detail by the methods described below. This thesis contributes to the understanding of low aspect ratio wing aerodynamics in general and to the knowledge of low actuation frequency flow control at low flight Reynolds numbers. The main objectives can be summarized as follows:

1. A detailed investigation of actuator performance through an actuator calibration study.

2. An identification and optimization of the parameters that maximize C_L and α_{stall} through aerodynamic force measurements.

3. The investigation of the lift enhancing mechanism through optical flow field measurements and time resolved surface pressure measurements.

4. A classification of the separated flow field above the wings.

The aforementioned aspects were studied experimentally on a number of different wing configurations through force and surface pressure measurements as well as particle image velocimetry (PIV). Initially half span (2.5D) wings were studied in a small (0.28 m $\times$ 0.4 m) wind tunnel. In this risk reduction phase mainly force measurements on a custom-made two-component wind tunnel balance were conducted. Several plan-form shapes with varying aspect ratios were studied with actuators located along the leading edge (LE), trailing edge (TE), and wing tip (WT). The flow control effect was quantified by measuring the lifting force while

the actuation frequency was varied in a frequency scan. The experiences gained from these measurements were then applied to three dimensional wings mounted on a support arm in a 1.4 m × 2.0 m wind tunnel. Again forces were measured while the forcing frequency was varied and the results were then compared to those of the half span wing study.

In order to gain further insight into the driving mechanisms of the lift enhancement effect the flow dynamics of the actuated flow fields were studied using the results from PIV measurements. The control cases were then compared to the unactuated (baseline) cases. This was accomplished by performing a triple decomposition of the velocity field into a mean, a coherent, and a stochastic component. The coherent structures were extracted using a proper orthogonal decomposition (POD). A POD is a statistical method which performs a projection of a data-set onto a new, energetically optimal basis, i.e. a principal axis transformation. It is a commonly used statistical tool in the field of turbulence and allows the identification of energetic (dynamic) structures within a flow field. The respective spatial distribution of the coherent kinetic energy reveals how the flow dynamics are affected by the actuation. Several visualization techniques were used to communicate the experimental results and their physical meaning. Apart from presenting the quantitative spatial distributions of several flow field variables a qualitative visualization technique based on line-integral convolution (LIC) was utilized. This technique can be used to visualize structures in the mean flow field which helped in categorizing the separation type.

With a view on a possible practical application of the control methods used in this study hinge-less roll control by means of DBD actuators was applied to one of the three dimensional wing plan-forms. The emphasis was on the determination of the obtainable roll control authority in terms of the roll-rate. A possible additional application for MAVs would be gust alleviation.

The flow dynamics were additionally studied through time resolved pressure measurements performed on a two-dimensional wing with LE control. These were then compared to the results of the PIV study. In both investigations a similar mechanism was identified and related to the vortex dynamics.

A reoccurring topic in this study is the scaling of the actuation frequency. The emphasis here is on the estimation of the dominating length scale that should be

used for the nondimensionalisation of the actuation frequency. It will be shown that the optimum forcing frequencies for flat plate wings at post-stall angles of attack are in the range of typical bluff body shedding frequencies. Moreover it is reasoned why forcing at bluff body frequencies necessarily results in maximum lift increase.

In studying flow control the actuator output needs to be considered in order to put the experimental study into the context of the results reported in the literature. The momentum coefficient C_μ relates the momentum induced by the actuator to the momentum contained within the free stream and is the most widely used parameter for characterizing actuator output in a flow control studies. The DBD actuators were characterized in a detailed calibration study, where the actuator output was determined by measuring the induced thrust and relating this to the input into the actuator, i.e. the peak-to-peak voltage V_{p2p} or the consumed electrical power P_{el}. The investigated parameter range was limited by the high voltage (HV) generator operational limits and can not be generalized. Nonetheless they do represent and quantify the actuator configurations that were utilized within the scope of this study.

3. STATE OF THE ART & LITERATURE REVIEW

There has been a growing interest in small unmanned aircraft or micro air vehicles (MAVs) over the last years ([MKIS07]). Possible applications for MAVs are sensing and surveillance missions. For example a MAV equipped with biochemical-sensors could explore environments dangerous or toxic to humans in case of emergencies. When utilized in swarms MAVs can be used to locate and track clouds of toxic fumes or for building up emergency relay communications networks ([LZF07]). Furthermore, environments inaccessible to humans or earth-bound robots could be explored by MAVs in order to locate survivors in case of catastrophes.

3.1 Definition of MAVs, Plan-Form Shapes

The typical mission description implies that a significant fraction of the mission is characterized by relatively low loiter speeds in the range of 6 to 20 m/s (Mueller (ed.)[Mue06]). According to the author the long term goal is to develop MAVs with a span of 8 cm that weigh less than 30 g, though the original goal was a MAV with 15cm maximum dimension weighing less than 90 g. The corresponding chord Reynolds number is in the range $50\,000 \leq \mathrm{Re} \leq 150\,000$. At these low Reynolds numbers conventional airfoils suffer from low aerodynamic efficiency. The flow field is dominated by a laminar separation bubble on the airfoils upper surface. At sub-critical Reynolds numbers the transition to turbulence does not occur and the flow already separates at low angles of attack. As previously mentioned the research on low aspect ratio wings has been dominated by investigations on delta wing configurations at high Reynolds and Mach numbers. The reason was that in the past no application for low aspect ratio wings at low Reynolds numbers existed. This has changed with the miniaturization of avionics, which led to the

feasibility of MAVs.
The design features of these wings can be described as follows:

- Aspect ratio typically AR < 2; ideally AR $= 1$.
- Flat plate or s-shaped airfoil section.
- Planform shapes: rectangular, semi-circular, Zimmerman, inverse Zimmerman, and elliptical.

A compilation on low Reynolds number aerodynamics with an emphasis on MAVs is presented in the two reviews edited by Mueller ([Mue01] and [MKIS07]). In another paper by Mueller et al. [MTS06] the aerodynamic characteristics of several flat plate wing planform shapes are investigated at Reynolds numbers in the range $70\,000 \leq \mathrm{Re} \leq 140\,000$. Aspect ratios ranged from 0.5 to 2.0. Nonlinear lift effects were observed at the lower aspect ratios. These are related to an increased fraction of lift being generated by the tip vortices. The aspect ratio was found to be the dominating aerodynamic parameter followed by the planform shape and Reynolds number.
Torres & Mueller [TM01] investigated several low aspect ratio wing configurations in the Reynolds number range $70\,000 \leq \mathrm{Re} \leq 100\,000$. These included rectangular, elliptical and Zimmerman planforms (see Zimmerman [Zim32]) of various aspect ratios. With growing WT vortex strength the lift curves were found to become increasingly nonlinear with decreasing aspect ratio. The WT vortex arrangement is discussed for the different planform shapes. For AR ≤ 1.0 the inverse Zimmerman planform shape was found to be most efficient. The inverse Zimmerman was the planform shape with the smallest influence of the WT vortices on the flow field above the wing.
More recently Morse [Mor09] performed a detailed time-resolved stereo PIV study of a rectangular AR $= 0.5$ wing for Reynolds numbers between 15 000 and 66 000 and angles of attack between 14° and 20°. Although active flow control was not considered in this study, the baseline flow field and the interaction of LE and WT vortex were discussed in detail.

3.2 Flow Control on Wings

Aerodynamic performance of airfoils or wings, respectively, can be enhanced by means of flow control. In its simplest form this can be accomplished by a simple tripping wire to force the transition to turbulence and thus avoid the laminar separation on the wings upper surface. For the wing configurations discussed here this will not work as we are considering sharp LEs, which fix the location of separation and forces transition via the (reattaching) bubble. A more appropriate approach is to use active flow control methods to alter the aerodynamic characteristics and to increase the aerodynamic efficiency and maximum attainable lift of wings. Active control methods can be categorized by steady and unsteady excitation of usually separated shear layers above wings or deflected flaps.

Greenblatt & Wygnanski [GW00] discuss in their review article flow control by periodic excitation. The governing parameters of flow control for a deflected flap with periodic excitation at the flap shoulder and the influence of excitation frequencies and amplitudes on flow control efficiency are discussed. Furthermore the application of flow control to a multitude of wing configurations and actuator types are presented in detail.

Detailed active flow control studies have been performed on delta wing configurations and were reviewed by Mitchell & Delery [MD01]. Delta wings have fixed separation locations at the LEs. The flow separates and forms two stable, large vortices above the wing, which generate high lift up to large angles of attack. Periodic forcing along the LEs leads to higher lift, larger stall angle of attack and delayed vortex breakdown (Deng & Gursul [DG97], Gursul et al. [GSB95]). Hinge-less roll control authority can be obtained by applying asymmetric control to a wing (Margalit et al. [MGSW05]). This is especially interesting for MAVs as it would simplify their construction complexity.

Active flow control studies on low aspect ratio wings at low Reynolds numbers is hitherto very limited. The interaction of LE and WT vortices as well as the influence of flow control on the wake vortex system of a rectangular low aspect ratio wing at Re = 300 was recently studied numerically by Brunton et al. [BRT$^+$08] and Taira & Colonius[TC09b]. Steady trailing edge (TE) blowing

was found to be most effective in enhancing lift. The authors reason that the tip vortices are strengthened and thus the down-wash on the LE vortex is increased. This resulted in the LE vortex with its low pressure core to move closer to the wing surface and thus enhancement in lift.

In [TC09c] the authors numerically investigated the flow about rectangular and non-rectangular (Delta wing, elliptical wing, and semicircular wing) low aspect ratio wings at $300 \leq \mathrm{Re} \leq 500$. The study was focused on the vortex dynamics at $\alpha > \alpha_{\mathrm{stall}}$ and flow control was not considered. A wing-wake characterization was introduced with a steady, periodic, and aperiodic wake state depending on α, AR, and Re. In the periodic case the natural shedding frequency is clearly defined and for an $\mathrm{AR} = 3$ wing was found to be $\mathrm{St} = 0.12$ at $\alpha \leq 30°$. For the 2D case a higher Strouhal number of $0.14 \leq \mathrm{St} \leq 0.16$ was found. The authors emphasize the importance of the tip vortices on the wake dynamics, but found that the vorticity transport in the tip vortices of the non-rectangular planform shapes under consideration was not sufficient to prevent them from shedding. One interesting observation made by the authors was that even at a relatively high aspect ratio of $\mathrm{AR} = 4$ the flow did not show the characteristics of von Kármán vortex shedding that would be observed in a 2D case. They attribute this to the occurrence of span-wise stall-cells.

In a follow-up study Taira & Colonius [TC09a] simulated flow control at $\mathrm{Re} = 300$ by means of steady blowing tangentially to the wings upper surface at the leading edge, trailing edge, and at mid-chord. Blowing directions were varied between upstream, downstream, and sideways direction with a momentum coefficient of $C_\mu = 1.0\%$. The actuator was modeled as a body force and the actuators direct contribution to lift was found to be only a small fraction of the overall increase in lift. The authors focus their discussion on the interaction of leading edge, tip, and trailing edge vortices and how this interaction is modified by steady blowing at the respective locations. As the most effective configuration a trailing edge actuator blowing in the downstream direction was identified. This increases the lift by a factor of two through modification of the wake structure and mutual interaction with the leading edge vortex. Specifically it is claimed that the strengthening of the tip vortices is beneficial in the sense that it induces a velocity component that is directed towards the wings upper surface (i.e. a downwash),

which aids in pushing the leading edge vortex with its low pressure core closer to the wing and thus increase lift.
A personal discussion with Tim Colonius in May 2010 inspired the investigation of continuous trailing edge upstream blowing along the wings lower surface. The results were encouraging and are presented in section 7.3.1. This flow control method can be categorized as circulation control (CC) and requires a rather high momentum input in order to be effective.
The study of Taira et al. [TRCW10] focused on a AR = 2 wing at $\alpha = 30°$. Based on the results of their previous numerical simulations the trailing edge actuator location with blowing directed in downstream was considered to be superior to other locations in terms of maximum lift increase. The applied actuation frequency f is given as a fraction of the natural shedding frequency f_n as f/f_n, which ranged from 0.1 to 10. Highest lift increase occurred when the flow was forced at $f/f_n = 0.75$. Lift deviations from the mean value are also reported and at a slightly higher frequency of $f/f_n \approx 0.85$ these deviations are significantly smaller than when forcing at $f/f_n = 0.75$ with only a marginal decrease in mean lift. This aspect will be further discussed in chapter 8.4. Similarities to the lift enhancing mechanism of continuous blowing discussed in the authors 2009 paper are observed in that the forced trailing edge vortex sheet is rolled up into the tip vortices which in turn affect the shedding of the leading edge vortex.
Experimental results of trailing edge actuation are presented in chapter 7.3. The superiority of trailing edge actuation over leading edge actuation at the same forcing conditions could not be confirmed here. Trailing edge actuation was always inferior to leading edge actuation.

3.3 Similarities to Flapping Wing Flight, Dynamic Stall, and Vortical Lift Generation

The periodic generation and shedding of span-wise vortices also plays an important role in flapping wing flight and rotor aerodynamics. Although the same physical phenomenon is involved it is beneficial in the one case and detrimental in the other. Especially in insect flight the dynamic stall vortex (DSV) is an integral part of

lift generation. The low pressure core of the vortices generates an additional lift component. In fact, insect flight would not be possible at those low Reynolds numbers without the lift generating effect of DSVs. Ellington et al. [EBWT96] emphasize the importance of LE vortices for the unsteady lift generation in insect flight. They performed an experimental study on a hawk-moth and a flapping wing model. The generation and shedding of LE vortices in flapping flight are discussed and visualized by smoke wire visualization. Similarities to dynamic stall are drawn and the phases of a flapping cycle and the accompanying vortical structures are discussed in detail.

The typical timescales that were observed for natural flyers and swimmers are within the narrow band of $0.2 < \mathrm{St} < 0.4$ [SLT+08]. Here, the Strouhal number was calculated according to (3.1).

$$\mathrm{St} = \frac{2fh_a}{U_\infty} \tag{3.1}$$

The factor "2" in the nominator of equation (3.1) appears due to the fact that a *full* wing-stroke equals two times the flapping amplitude h_a.

In the field of rotor aerodynamics dynamic stall effects are usually considered detrimental, especially for wind turbines and helicopter rotors. The periodic vortex shedding induces periodical, dynamic loads on the rotor system. In wind energy these dynamic loads are the primary limiting factor for the lifetime of wind turbines. Considerable research is currently underway in order to reduce these dynamic effects by means of active flow control methods. In helicopter aerodynamics DSVs are avoided by the rotor-heads cyclic pitch system. The typical time scale for dynamic stall on helicopter rotors is $\kappa \approx 0.1$ [Lei06], with the dimensionless frequency κ according to (3.2)

$$\kappa = \frac{\pi f c}{U_\infty} \tag{3.2}$$

and if the same scaling parameters were used

$$\mathrm{St} = \frac{\kappa}{\pi} \tag{3.3}$$

. The key statement here is, that periodic vortex shedding can have both positive or negative effects depending on the technical/scientific field and on the frequencies at which shedding occurs. In both cases the shedding of vortices is associated with an increase in drag – detrimental in the case of helicopter aerodynamics, but obviously not for insect flight. Note that the Strouhal number range of natural fliers is within the range of optimum forcing frequencies observed here on low aspect ratio wings, while the DSV frequencies on helicopters are much smaller.

In the past several unconventional methods of generating high lift have been proposed. Most of these methods rely on trapped vortices, which are forced by either steady or periodic actuation. The low pressure core of these vortices generates additional lift, comparable to delta wing vortices. These applications of vortical flow are not limited to the low Reynolds number range.
Vakili [Vak90] reviewed several techniques of enhancing lift by utilizing vortices. He also discusses unconventional wing configurations featuring trapped vortices and active flow control. The author argues that the vorticity generated at the LE should not be shed into the wake but organized and directed into prescribed paths close to the body in order to become useful for lift generation. This organization and redirection can be accomplished by means of steady or unsteady suction and blowing or passive techniques and wing shaping.
Wu et al. [WVW91] discuss the generation of what they call *super lift* by utilizing vortical flows and unsteady excitation. Five physical principles for vortex control by unsteady excitation are examined. Stable as well as unstable vortices and their relation to lift increase are discussed as well as the stabilization of vortices by generating axial flow inside the vortex core. The wing configurations include two dimensional airfoils, swept wings, delta wings and unconventional configurations such as the Hurley flap wing. The authors believe that the utilization of vortex lift could bring about a breakthrough in lift generation and flight technology.
Broeren & Bragg [BB01] studied the unsteady stalling behavior of a number of low Reynolds number airfoils at $\mathrm{Re} = 300\,000$ with accompanying smoke visualization at $\mathrm{Re} = 75\,000$ and $100\,000$. Very low frequency lift fluctuations were measured with Strouhal numbers around $\mathrm{St}_h = 0.02$. The elimination of the lami-

nar separation bubble on the airfoils caused a distinct reduction in lift fluctuations. Several stalling characteristics are discussed and linked to unsteady lift generation.

3.4 The DBD Actuator as a Flow Control Device

The choice of flow control actuators for the wings that are considered here is quite limited due to geometrical restrictions. Dielectric barrier discharge DBD (plasma) actuators have recently become a popular device for active flow control because of their high flexibility in actuator placement, blowing direction and frequency spectrum. DBD actuators are simple to manufacture and several actuator locations and blowing characteristics can be studied on one and the same model without the need for structural changes when a different "slot"-location is to be investigated. The principles of DBD actuators are described by Enloe et al. [EMVF04], and Enloe et al. [EMFB05]. A theoretical study and simulation was done by Orlov et al. [OCP06], Orlov et al. [OAH+07], Likhanski et al. [LSO+07], and Opaits et al. [ONL+07]. The high flexibility of DBD actuators in the sense of blowing direction and characteristics is described by Santhanakrishnan et al. [SJS06]. Annular and linear plasma synthetic jet actuators are described and quantitative results of PIV measurements are presented. It was found that the generation of synthetic jets (in this case DBD actuators induce a flow perpendicular to the surface the actuator is applied to) enhances the penetration of the surrounding fluid. Porter et al. [PAC+08] investigated plasma induced jet vectoring and the generation of spatially distributed velocity variations. The study is aimed at the increase of aerodynamic performance of airfoils and the drag reduction on cylinders. A biologically-inspired use of DBD actuators was derived from the flippers of humpback whales, which feature so-called *tubercles* along the LE, which form a spatial waviness in span-wise direction (Fish & Lauder[FL06]). This effect of waviness can be generated by spatially distributed forcing with DBD actuators. Only a small modification in the covered electrode geometry is necessary to accomplish this.

Clearly, the flexibility of DBD actuators is demonstrated in these studies. Sev-

eral possible plasma actuator configurations and the respective induced jet directions are discussed in chapter 4.5, where the results of high speed Schlieren imaging are presented.
Flow control by DBD actuators is not only limited to conventional wings. Delta wing flow control was experimentally studied by Greenblatt et al. [GKNP08]. The LE vortices were found to be located closer to the wings surface and strengthened as control is applied at the optimum forcing frequency. Also the shear layer curvature increased, presumably due to increased entrainment of high momentum fluid from above the wing.
Due to the limited range of attainable velocity, plasma actuators are currently limited to low flight Reynolds number applications. Constant development of new dielectric material and high voltage sources can expand its applicability to higher free stream velocities.
The use of DBD actuators for hinge-less roll control was studied by Nelson et al. [NCH+07] on a swept wing UAV. The roll-control effect was found to be comparable to hinged control surfaces. This is backed up by the results obtained by Vorobiev et al. [VRJM08] on a AR = 4.5 wing. Plasma flow control can also be utilized to replace flaps. This was demonstrated by Corke et al. [CHP04].

3.5 DBD Actuator Flow Control on 2D Wings

Experimental results of DBD actuator flow control on three-dimensional wing configurations is scarce, but two dimensional wing configurations with DBD actuator flow control, mainly along the LE, were studied by a number of researchers (Corke et al. [CJPO02], Corke & Post [CP05], Post & Corke [PC03], Post & Corke [PC04a], Post & Corke [PC04b], Sosa et al. [SAMT07], Bachmann et al. [BUV+09], Mabe et al. [MCW+09]).
In summary the findings were that plasma flow control is effective only at post-stall angles of attack, actuation effect deteriorates with increasing free stream velocity, and that a pulsed actuation at certain frequencies is superior to steady blowing. Corke et al. [CPO07] discuss the use of plasma actuators as a flow control device in general. The parameters that govern the induced jet velocity are identified

and methods to optimize the actuator design are discussed. A numerical model for the generated body force is presented and simulation results for a plasma actuator at the LE of an airfoil are presented.

An experimental investigation of plasma flow control on flat plate wings was conducted by Greenblatt et al. [GGR+08] in the Reynolds number range from 3 000 to 20 000. Pulsed actuation was found to be superior to steady blowing and lift increases of up to $\Delta C_L = 0.4$ as well as enhanced endurance were observed. Increased levels of C_L were observed for reduced frequencies in the range $0.4 < F^+ < 0.6$. The positive control effect on an AR = 6 semi-span wing did not materially change compared to that of the two dimensional wing studied.

In a follow-on study Greenblatt et al. [GSS12] compare their experimental results of the flat plate wing to numerical (CFD) 2D laminar flow simulations. Their comparison was performed for a Reynolds number of Re = 3 000 and special emphasis was placed on the actuator calibration and the matching of a heuristic DBD plasma body-force model to the experimental data. Generally favorable agreement between experimental and numerical data was found, with the simulations accurately predicting the range of favorable forcing frequencies $0.2 \lessapprox F^+ \lessapprox 0.5$, corresponding to $0.07 \lessapprox F^+ \sin(\alpha) \lessapprox 0.175$. Furthermore, the simulations revealed a natural bluff-body shedding at $\mathrm{St} = f_{\mathrm{sh}}\, c \sin(\alpha) \,/\, U_\infty \approx 0.182$, which could not be observed in the experimental study. The authors conclude that the optimum forcing frequency for lift enhancement is in the range of the unforced bluff-body shedding frequency (a similar observation was made by Taira et al. [TRCW10], see above). The fluid mechanical lift enhancement mechanism was attributed to an optimal spacing of consecutive vortices above the wing and the vortices mutual interaction. At optimum forcing frequencies the time mean streamline deflection towards the wings upper surface reached a maximum. This illustrates the fact that circulation about the wing is increased by (optimum) actuation.

Investigator(s)	type	wing configurations	AR	Re	α	frequency	C_μ	actuation
Torres & Mueller [TM01]	exp.	flat plate (rect., ellipt., (inv.) Zimmerman)	0.5 – 2.0	7E3 – 10E3	$\leq 40°$	n.a.	n.a.	n.a.
Morse [Mor09]	exp.	flat plate, rect.	0.5	15E3 – 66E3	14° – 20°	n.a.	n.a.	n.a.
Brunton et al. [BRT+08]	num.	flat plate, rect.	2.0	300	0° – 30°, 28°	$0.032 \leq \mathrm{St} \leq 0.255$	n.a.	pitching / plunging
Taira & Colonius [TC09a]	num.	flat plate, rect.	1.0, 2.0, 4.0	300	10°, 20°, 30°	steady	0.51%, 1%	volume force
Taira & Colonius [TC09c]	num.	rect., delta, ellipt., semi-circ.	1.0, 1.5, 2.0, 3.0, 4.0	300, 500	0° – 60°	$\mathrm{St} = 0.12$	n.a.	n.a.
Taira et al. [TRCW10]	num.	rect.	2	300	30°	$(f/f_n)_{\mathrm{opt}} = 0.75$	0.5%	volume force (TE)
Goeksel et al. [GGR+06]	exp.	E338, cylinder, (2D)	2D	10E3 – 140E3	−10° – 40°	$F^+_{\mathrm{opt}} \approx 1.0$	$\leq$ 8.4%	DBD at $x/c = 1\%$
Greenblatt et al. [GKNP08]	exp.	semispan delta wing (60° sweep)	1.15	20E3 – 75E3	$\lessapprox 40°$	$F^+_{\mathrm{opt}} \approx 1.0$	$\leq$ 2.1%	DBD along LE
Greenblatt et al. [GGR+08]	exp.	flat plate, E338, (2D)	6, 2D	3 000 – 50E3	$\leq 30°$	$F^+_{\mathrm{opt}} \approx 1.2$ (E338), $F^+_{\mathrm{opt}} \approx 0.5$ (flat plate)	$\leq$ 1.2%	DBD at: $x/c = 1\%$ (E338), LE (flat plate)
Greenblatt et al. [GSS12]	exp. & num.	flat plate	3, 2D	3 000	20°, 24°	$F^+_{\mathrm{opt}} \approx 0.24$ ($\rightarrow F^* \approx 0.12$)	$\leq$ 0.74%	DBD along LE
Rizzetta & Visbal [RV12]	num.	flat plate	2.0	20 000	8°, 25°	$\omega_{\mathrm{a}} = 0.8$	n.a.	volume force (LE, WT; continuous, pulsed)

Tab. 3.1: Low aspect ratio wing aerodynamics and flow control studies. Including some relevant 2D wing investigations incorporating DBD actuator flow control.

4. DBD ACTUATORS FOR FLOW CONTROL APPLICATIONS

4.1 State of the Art of DBD Actuators

In the last 10 years dielectric barrier discharge (DBD) actuators for flow control applications have been intensively investigated in numerous experimental and numerical studies. Due to a plasma discharge with associated light emission that develops on the actuator they are commonly termed "plasma actuators".

In the chemical, medical and paper industry dielectric barrier discharges have been utilized for years for sterilization and surface treatment. In these fields DBDs are mainly used in a symmetric electrode configuration and the main interest is in the production of Ozone O_3. This is in contrast to flow control applications, where the main interest is in the production of thrust through an induced velocity in the vicinity of the exposed electrode. In these applications the generation of Ozone is an undesirable side effect.

A typical DBD for flow control purposes is depicted in Fig. 4.1. It consists of two electrodes in an asymmetric arrangement: a covered, grounded electrode and an exposed electrode which is connected to a high voltage generator. The electrodes consist of a conducting material, typically (tinned) copper. Located in-between the two electrodes is the dielectric material (i.e. the "dielectric barrier"). This material is non-conductive and typical materials are: glass, ceramics (Macor), Mylar, Teflon, or KAPTON® among other isolating materials.

By applying a high voltage to the electrodes a plasma discharge is generated downstream of the exposed electrode. Within the plasma discharge region a volume force is exerted upon the surrounding fluid. The principles of DBD actuators and the force coupling are described in more detail by ENLOE ET AL. [EMVF04] and ENLOE ET AL. [EMFB05] and in the review paper by CORKE ET AL. [CEW10]. A theoretical study and simulation of DBD actuators was conducted by ORLOV

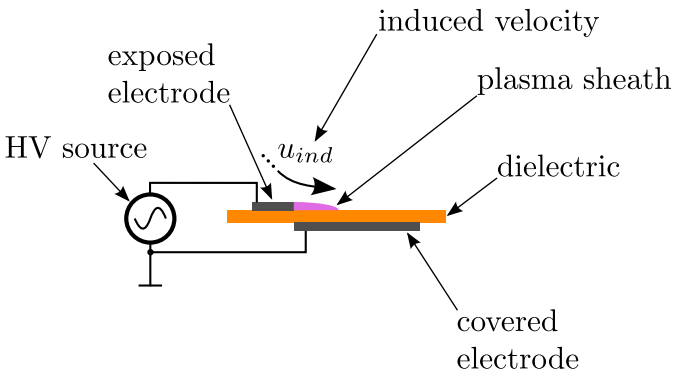

Fig. 4.1: Typical DBD actuator arrangement.

Fig. 4.2: The *Minipulse 1* HV generator with associated signal flow.

et al. [OCP06], Orlov et al. [OAH+07], Likhanskii et al. [LSMM07] and Opaits et al. [ONL+07]. The HV generator that was used in this study was a *Minipulse 1* by GBS Elektronik [GBS11]. A maximum peak-to-peak voltage of approximately $V_{\mathrm{p2p}} = 20\,\mathrm{kV}$ at ionization frequencies between $f_{\mathrm{ion}} = 3 - 20\,\mathrm{kHz}$ was possible with this system. A DC supply voltage of up to $V_{\mathrm{DC}} = 32\,\mathrm{V}$ and the desired ionization frequency in the form of a $\pm 5\,\mathrm{V}$ sinusoidal signal was supplied to the HV generator (figure 4.2). This signal was amplified with an amplification function that depends on the applied V_{DC} and f_{ion} to yield the peak-to-peak voltage V_{p2p} at f_{ion}. This dependency is illustrated in Fig. 4.5 and further discussed below. Depending on the desired flow control application DBD actuators can be operated in continuous mode or in burst mode (*bm*). In continuous mode an uninterrupted HV signal at f_{ion} is fed to the DBD actuator. A temporal constant volume force is thus created by the actuator. The effect is similar to other flow control methods that utilize continuous wall jets or moving wall surfaces. When the actuator was operated in burst mode the ionization voltage signal was periodically interrupted at the so called modulation frequency f_{mod} with a certain duty cycle of typically $dc = 20\%$. Within this study the modulation frequency was within

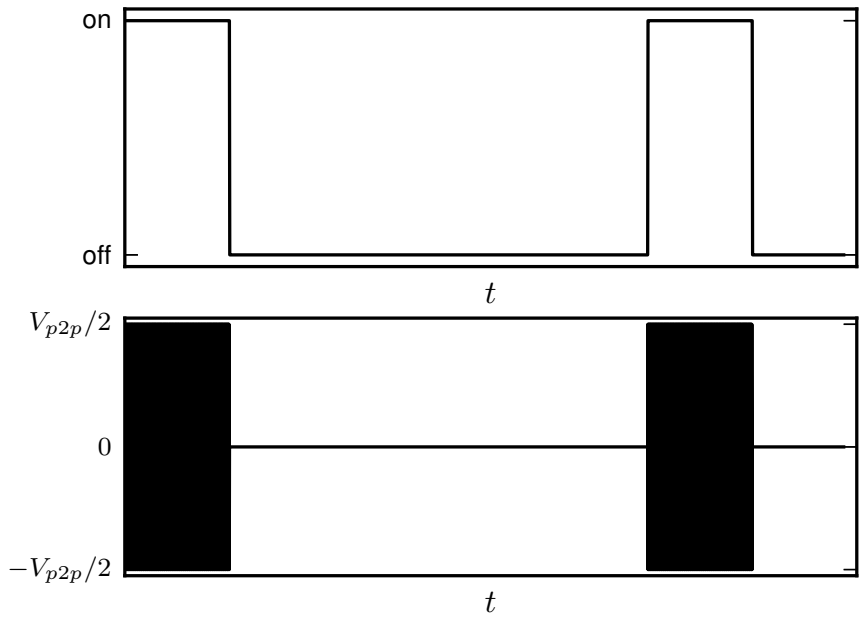

Fig. 4.3: DBD actuation signal with a duty cycle of $dc = 20\%$.

the range of $f_{\text{mod}} = 0 - 40\,\text{Hz}$. An example of the resulting signal is shown in Fig. 4.3. Shown in the top half is the modulation signal which defines when and for how long the actuator was turned on. For the fraction of time when the actuator is turned on it operates at the desired f_{ion} and V_{p2p} (bottom half of Fig. 4.3). Flow control using DBD actuators can be termed as "zero mass flux" (ZMF) actuation, because no mass is added or removed from the surrounding fluid. The momentum flux is finite though. In fact the Fourier decomposition of the temporal volume force (4.1) contains a constant term $0.2A$, indicative of a finite integral momentum input into the flow (A is the actuator amplitude, i.e. V_{p2p} or thrust F.

$$f(t) = 0.2A + \frac{2A}{\Pi} \sum_{n=1}^{\infty} \frac{\sin(0.2n\Pi)}{n} \cos\left(\frac{2n\Pi}{T} t - 0.2n\Pi\right) \tag{4.1}$$

In order to quantify actuator output Romann [Rom08] at TU Berlin conducted LDA measurements downstream of a DBD actuator. A superimposed LDA data set is shown in Fig. 4.4. The measurement point was located 2.5 mm downstream

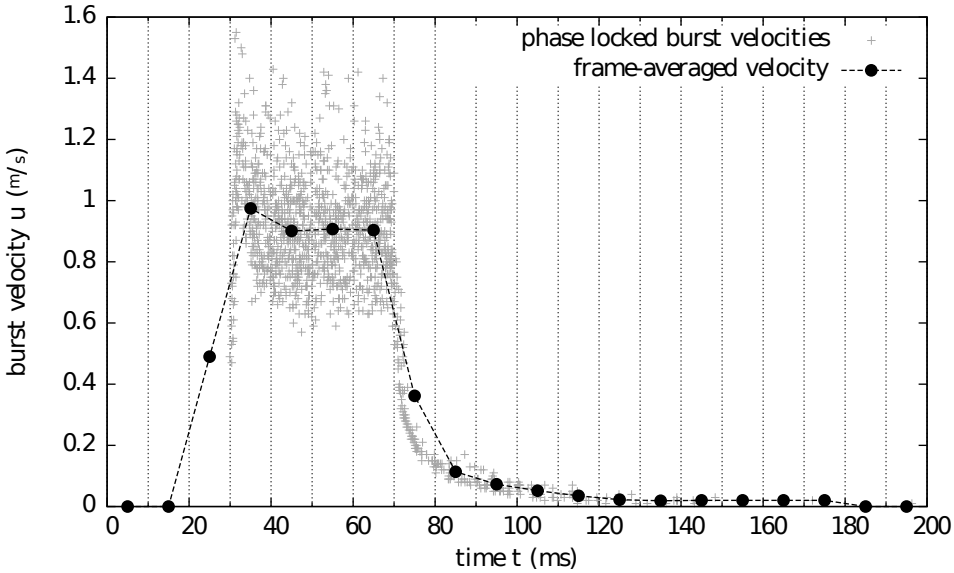

Fig. 4.4: Ensemble averaged LDA-signal of DBD actuator (from ROMANN [Rom08]). $f_{\mathrm{mod}} = 5\,\mathrm{Hz}$, $f_{\mathrm{ion}} = 4\,\mathrm{kHz}$, $dc = 20\%$

of the edge of the exposed electrode. The maximum burst velocity for this configuration was 1 m/s. It is interesting to note the step-like rise of the burst velocity within $\Delta t = 1\,\mathrm{ms}$ at $t = 30\,\mathrm{ms}$. At the end of the burst the velocity fell off exponentially to zero. For an optimized actuator configuration Romann measured a peak velocity of 2.5 m/s at a location 2.5 mm downstream of the exposed electrode edge and approximately 0.3 mm above the dielectric.

4.2 Estimating DBD Output

The aim of this part of the study was to characterize the utilized dielectric barrier discharge (DBD) actuators in terms of the induced thrust as a function of the applied high voltage V_{p2p}, the ionization frequency f_{ion} of the plasma discharge, and the actuator geometry.

High voltage (HV) generator, HV supply cables and the specific DBD actuator form a nonlinear system. The impedance of this system needed to be tuned in order to maximize the induced thrust. The induced thrust was measured using a laboratory scale (type: *Vibra AJ-220E*). In order to estimate the direction of the induced body force Schlieren images for selected actuator configurations were

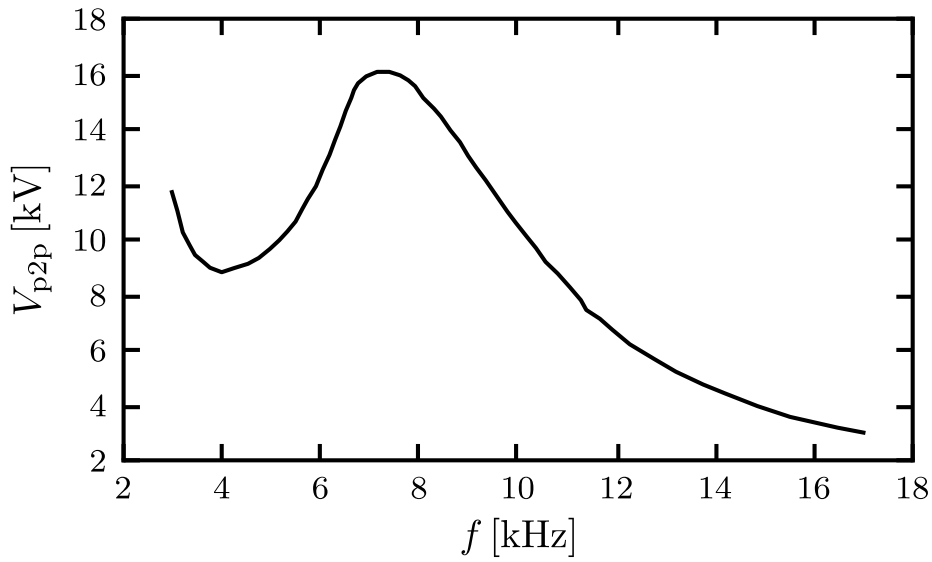

Fig. 4.5: Frequency response of the *Minipulse 1* HV generator at constant DC supply voltage.

taken with a high speed camera. The transfer characteristics of the HV generator for a specific DBD actuator were measured by applying a fixed dc supply voltage to the HV generator and then varying f_{ion} while at the same time measuring the induced thrust. Optimum f_{ion} depends on actuator length, dielectric material, electrode configuration and HV supply cables. Before an actuator was applied to one of the wings tested in this study, it was characterized by the technique described above. A typical result is shown in Fig. 4.5. The maximum amplitude in this case is generated at frequencies of about $f_{\mathrm{ion}} = 7\,\mathrm{kHz}$.

4.3 Experimental Setup for Thrust and Power Measurements on DBD Actuators

In order to quantify actuator output and compare different actuator configurations the induced thrust of the actuators was measured by means of a laboratory scale. In previous experiments by Utehs [Ute10] a traversing micro-Pitot-tube was used to measure the induced velocity of the actuators. Due to uncertainties about the influence of the Pitot-tube and the point-type measurement principle it was

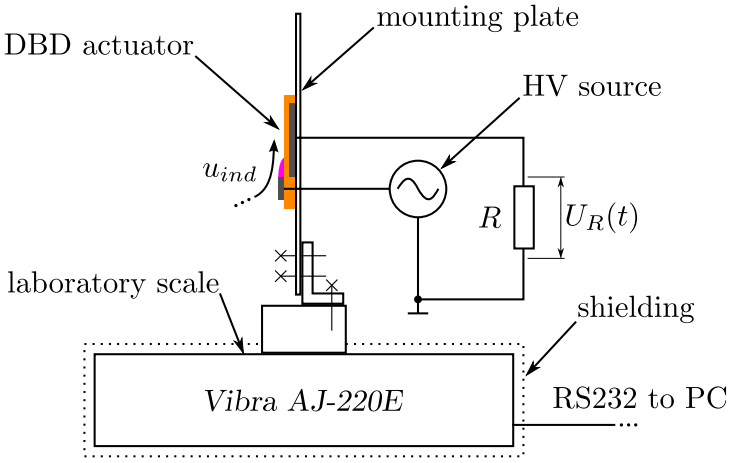

Fig. 4.6: Setup to measure induced force by DBD actuators. The high voltage cabling was laid in loops to avoid force coupling (wire ⌀0.1 mm).

decided to use an integral measuring technique. The laboratory scale was a *Vibra AJ-220E* ($d = 0.001\,\mathrm{g}$), which uses a tuning-fork measurement principle [Vib12]. Shown in Fig. 4.6 is the experimental setup for the thrust measurements. The DBDs were mounted on a mounting plate that was attached to the sensing element of the scale. In order to avoid a force coupling through the high-voltage power supply cabling an enameled copper wire with a diameter of ⌀0.1 mm was laid in loops from the HV generator to the DBD actuator. Care was taken to keep an as large as possible distance between the HV cable and the grounded cable or balance. This was done to avoid sparking between the cables or any grounded or shielded experimental equipment. Additionally a large distance between the wires needs to be kept because parallel, current-carrying wires exert a force upon each other which might affect the thrust measurements (this is actually how the unit *Ampere* is defined). The laboratory scale itself was shielded by a mesh of fine copper-wire to avoid cross-talk and fatal sparking. A *LabVIEW*-program was written to collect the balance readings via a RS-232 connection and to control the actuator operating point (Utehs [Ute10] and Lindner [Lin11]). The sinusoidal low-voltage input signal for the HV generator was generated by an *Agilent 33220A* function/waveform generator and the DC input voltage was provided by an *Agilent E3634A* programmable DC power supply. Power consumption of the actuator was measured by introducing a shunt resistor of $R = 1\,\Omega$ to the ground line of the

actuator. The voltage drop across the shunt $U_R(t)$ was measured, together with the high-voltage $U(t)$, by an *Agilent 5014A* oscilloscope. The electrical power P_{el} was then calculated according to (4.2). It is emphasized here that during the thrust- and power- measurements the actuators were operated in continuous mode. In the flow control study the actuators were operated in burst mode, i.e. with a duty cycle of typically $dc = 20\%$. Accordingly the electrical power needs to be multiplied by the duty cycle: $P_{\mathrm{el,bm}} = dc \cdot P_{el}$.

$$P_{\mathrm{el}} = \frac{1}{N \cdot T} \int_0^{N \cdot T} \frac{U(t) \cdot U_R(t)}{R} \, \mathrm{d}t \tag{4.2}$$

Electrical power P_{el} and $P_{\mathrm{el,bm}}$ and induced thrust F were normalized by the actuator length L.

4.4 Electrode Configurations

The induced thrust or velocity of a DBD is highly dependent on the configuration of the exposed electrode. In this regard the important variables are:

- electrodes overlap d ($d < 0$: overlap, $d > 0$: gap)
- geometry and surface quality of the electrodes edge (straight, serrated, wire...)
- electrode material

The geometry of the exposed electrode directly influences the strength of the electric field. For example if the electrode consists of a simple wire a smaller wire diameter would result in increased induced velocities. The physical mechanism is the increased strength of the electric field in the vicinity of a thin wire. Because the acceleration of ions is larger in stronger electric field a higher velocity/thrust is obtained. A comparable effect was observed when DBD actuators were wrapped around the leading edge of a flat plate wing. Results are shown in Fig. 4.11 and discussed at a later point.
Actuator output as a function of electrode overlap (or gap) was investigated by Lindner [Lin11]. For straight edged exposed electrodes Lindner found that a

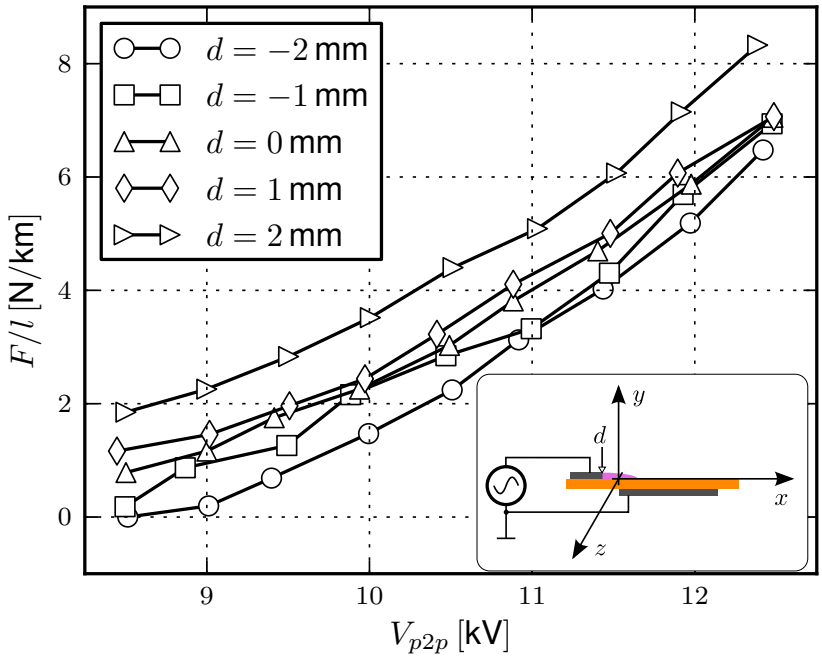

Fig. 4.7: Effect of electrode overlap on induced thrust for DBD actuators with straight-edged exposed electrodes. Inlay showing coordinate system centered above the upstream edge of the covered electrode. Negative overlap ($d < 0$) results in a gap in x-direction between the two electrodes. Length of the encapsulated electrode was $L = 10\,\mathrm{cm}$.

higher thrust was generated for overlapping electrodes (figure 4.7, $d > 0$). If the overlap was too large such that the upstream edge of the exposed electrode was located above the covered electrode a backward ionization was observed, i.e. a plasma discharge on the upstream edge was produced. This generated thrust in reversed direction and thus reduced the net-thrust. Backward ionization can be avoided by applying a layer of KAPTON® along the relevant edge of the exposed electrode. Actuators with negative overlap, i.e. a gap, tended to generate a filamentation of the plasma discharge and as a result the durability of the dielectric was reduced. The actuators that were used in the flow control study of this work had an overlap of $d \approx 1.5\,\mathrm{mm}$.

The fact that an increased electric field strength increases the induced thrust inspired the design of the actuators that are discussed in the following. Here the geometry of the exposed electrode was varied and its effect on induced thrust was measured. In most numerical and experimental studies a straight edged exposed electrode is used on DBDs. That means the downstream edge of the exposed electrode is a straight line. Under normal operating conditions a homogeneous plasma discharge (without signs of filamentation) is generated downstream of the exposed electrode – the actuator can be treated as two-dimensional. One way of generating a higher electric field strength is by using serrated exposed electrodes. On serrated electrodes the largest field strengths are generated in the vicinity of the apexes. Shown in Fig. 4.8 is the comparison of a straight edged actuator with two serrated actuators of different spike-density (number of spikes per length). The dielectric material for these actuators was FR4 with the electrode shapes etched into the two-sided copper layer.

The measurements were conducted for a range of peak-to-peak voltages V_{p2p} at a constant ionization frequency of $f_{\mathrm{ion}} = 8\,\mathrm{kHz}$. All the actuators downstream edges were aligned with the exposed electrode ($d = 0\,\mathrm{mm}$). Clearly the actuators with serrated electrodes generated a larger thrust than the reference design with the straight exposed electrode (figure 4.8). The actuator with the highest spike-density (5 spikes/cm) generated the largest thrust. At a typical operational peak-to-peak voltage of $V_{\mathrm{p2p}} = 10\,\mathrm{kV}$ the thrust is approximately three times larger than for the actuator with straight edged electrode. It is assumed that by further increasing the spike density even higher thrust could be generated. At some point a maximum must be reached, because an infinite number of spikes would represent a straight edged electrode and the plasma discharge would thus become homogeneous again. Looking at the power consumption of the three actuators (figure 4.9) the actuator with the highest spike density had the smallest power requirement per produced thrust. The 2.5 spikes/cm actuator consumes approximately the same power as the straight edged electrode actuator.

To shed light on the question why the serrated electrodes generated higher thrust and why a higher spike-density is beneficial, the plasma discharge was looked at in more detail. Shown in Fig. 4.10 are photographs of the plasma discharge that were taken with a macro lens. Marked by a dashed line is the $x = 0\,\mathrm{mm}$ position

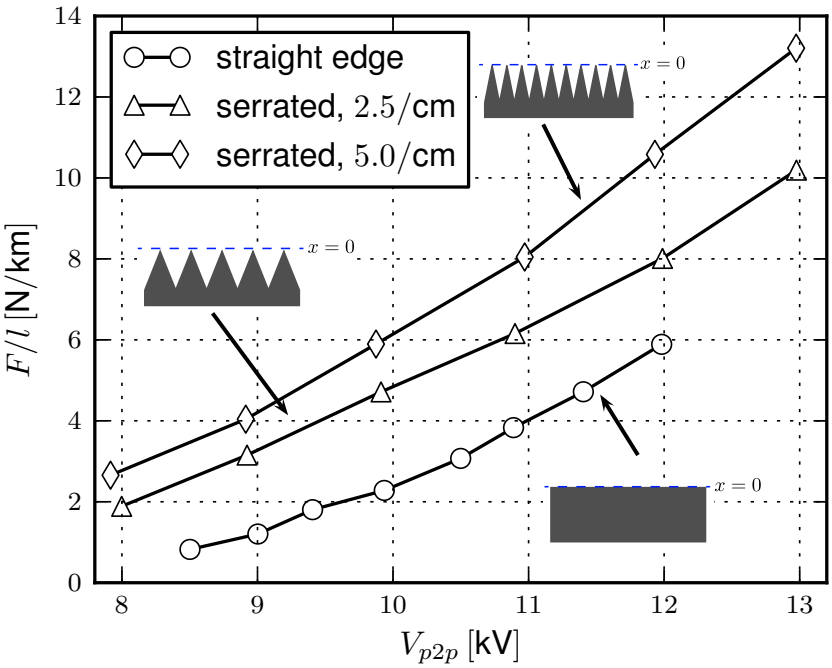

Fig. 4.8: Comparison of straight and serrated electrodes. The serrated electrodes were utilized in the roll control study (see chapter 7.7). Electrode overlap $d = 0\,\mathrm{mm}$, also see Fig. 4.10 for details on the plasma discharge and Fig. 4.7 for electrode arrangement.

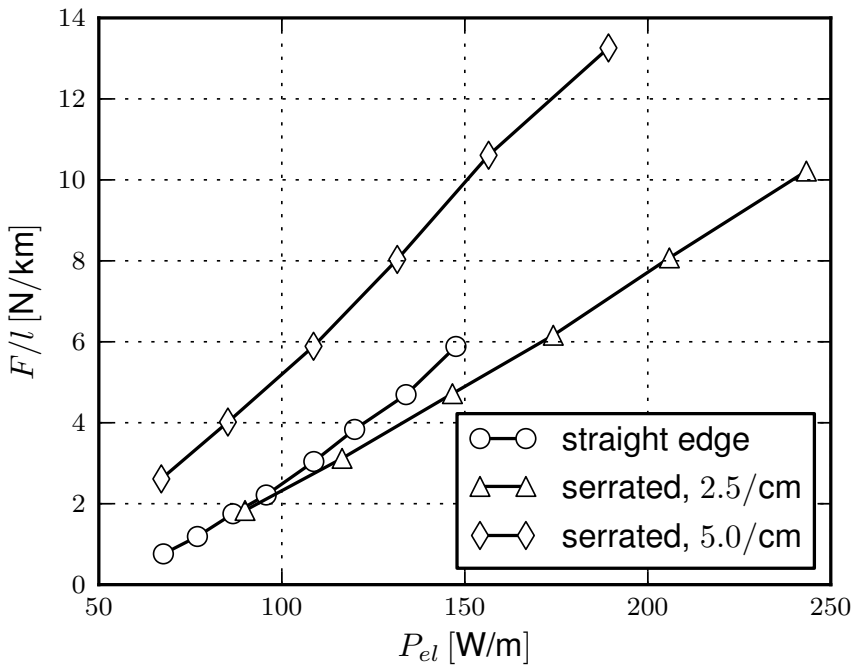

Fig. 4.9: Power consumption of two serrated actuators with different spike density and a straight exposed electrode actuator. Dielectric material is FR4 with etched electrodes.

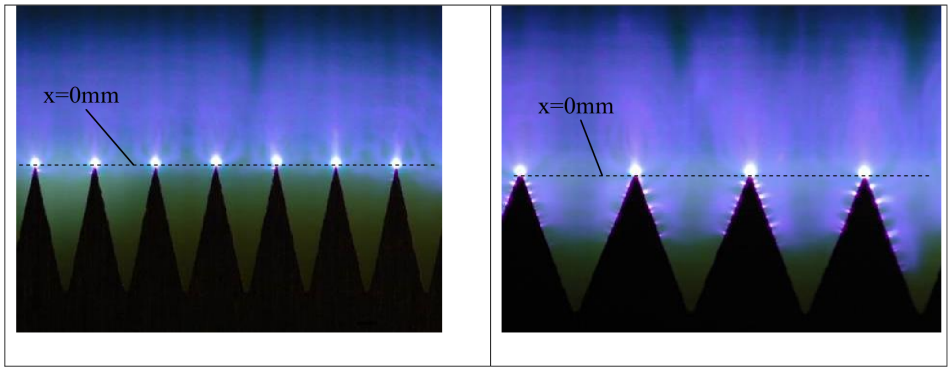

Fig. 4.10: Plasma discharge filamentation on two serrated electrodes. Actuators operated at the same V_{p2p} and f_{ion} = 8kHz. Left: 5.0 spikes/mm, right: 2.5 spikes/mm. Note plasma discharge for negative values of x (beneath dashed line) in right image.

of the upstream position of the covered electrode. The plasma discharge of the 5.0 spikes/mm actuator (left in Fig. 4.10) is concentrated around the apexes and in the region of positive x-values. At the right hand side of Fig. 4.10 the plasma discharge of the coarsely serrated actuator is also spread along the edges of the spikes (negative x-values). This induces volume forces that are inclined to the x-axis direction and therefore do not contribute to the thrust.

It is emphasized that serrated electrodes do not generate a homogeneous volume force – the volume force varies in span-wise direction according to the spike-spacing. In a flow control application the actuator would therefore generate stream-wise vortices with a span-wise spacing commensurate with the spacing of the spikes. How the specific flow control goals are affected by this still needs to be clarified. A span-wise varying volume force was beneficially implemented in at least one study (Porter et al. [PAC+08]) for the drag reduction of cylinders in cross-flow.

The serrated-electrode actuator seems to be superior to the straight-electrode actuator. This electrode configuration was only tested at an advanced stage of this thesis and therefore the majority of experiments were conducted using the straight-edge actuator. Serrated electrodes were only used in the roll-control study which is discussed in chapter 7.7. Both actuator configurations are assumed to produce similar effects and therefore the actual actuator type is of minor importance.

The de facto standard DBD actuator used in most experimental studies including the current one featured a straight exposed electrode edge and used KAPTON® tape as a dielectric material. This actuator type was studied in detail through force and power measurements. Typically the actuator is applied to a flat surface like a wing. Within the current study of flow control on flat plate wings the actuators were usually mounted to the edges of the wings, i.e. to the edges of a flat plate. As already mentioned above the geometric configuration of the exposed electrode affects the thrust that is generated by the actuator. Therefore an actuator that is applied to an edge is expected to behave differently as an actuator that is applied to a flat surface. This inspired the comparison between the two actuators shown in Fig. 4.11. At a typical operating peak-to-peak voltage of $V_{\mathrm{p2p}} = 8\,\mathrm{kV}$ the edge actuator generated 2.5 times the thrust of a flat actuator operated under the same conditions. Although both exposed electrodes had the same dimensions the electrode in the case of the edge actuator is virtually smaller – the covered electrode only "sees" the edge of the exposed electrode at the upper corner of the plate. It is assumed that the exposed electrode of a "standard" flat DBD actuator is comparable to a thick wire while the exposed electrode of the edge actuator can be compared to an actuator with a thin wire. The thinner the wire, the higher the electric field strength. Note that the edge actuator consumes approximately half the power when compared to a flat actuator operated at the same thrust level. The power consumption of the edge actuator is $P_{\mathrm{el}} = 45\,\mathrm{W/m}$ when operated at $V_{\mathrm{p2p}} = 8\,\mathrm{kV}$. Considering the typical duty cycle of $dc = 20\%$ the resulting power consumption in burst mode operation is $P_{\mathrm{el,bm}} = 9\,\mathrm{W/m}$. What needs to be pointed out here is the fact that a duty cycle of $dc = 20\%$ is a rather conservative value and could be further reduced without any detrimental effect on control authority. This is discussed in more detail in the flow control section.

When comparing the power consumption of the straight actuators in figures 4.9 and 4.9 it is noted that at the same induced thrust the actuator in figure 4.9 consumes more power. This is due to the different dielectric (FR4 and KAPTON®, respectively). In this case different dielectric materials were used because it was more convenient to etch the different serrated electrodes, while the edged actuator could only be built using dielectric and conducting tapes. Therefore the compari-

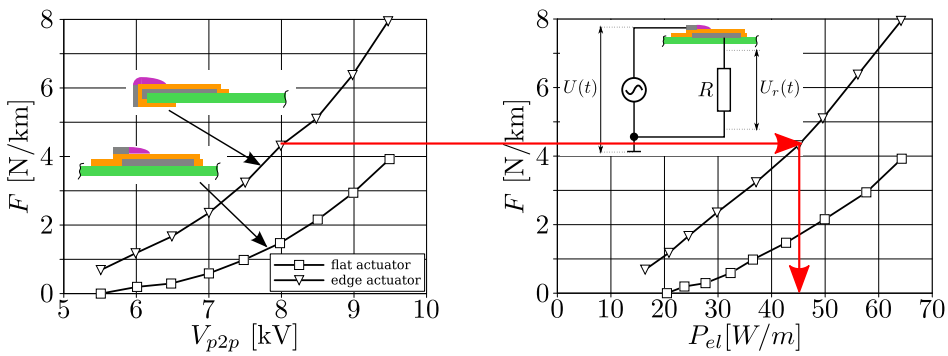

Fig. 4.11: Comparison of flat and edged actuator configurations at $f_{\text{ion}} = 4.75\,\text{kHz}$, schematic for power measurement. Edged actuator generates twice the thrust of a flat actuator – at the same power consumption. Dielectric material is KAPTON®.

son of the different electrode shapes is only relative and depend on the respective dielectric material.

Shown in Fig. 4.12 is another comparison of a flat and an edged actuator. This time the actuators were operated at an ionization frequency of $f_{\text{ion}} = 8.00\,\text{kHz}$. The measurements on the half span wings were mainly conducted at $f_{\text{ion}} = 8.00\,\text{kHz}$ and $V_{\text{p2p}} = 10\,\text{kV}$ while for the full span wings (3D) $f_{\text{ion}} = 4.75\,\text{kHz}$ and $V_{\text{p2p}} = 8\,\text{kV}$ was used to operate the DBD. The choice of different operating parameters was due to the increased length of the actuators on the full span wings. This resulted in a different electrical load and therefore the HV generators had to be operated at a different operating point in order to generate a higher peak-to-peak voltage.

Though the matter of momentum coefficient C_μ will be discussed in more detail in the flow control section some typical numbers for the relevant flow control cases are given in table 4.1 already at this point.

One possibility of increasing the actuator output is by operating it at a higher ionization frequency f_{ion}. Shown in Fig. 4.13 is the dependency of the induced thrust on f_{ion}. Higher ionization frequencies lead to a higher induced thrust. At $V_{\text{p2p}} = 8\,\text{kV}$ the thrust is increased by a factor of two when the ionization frequency is increased from 6 kHz to 10 kHz.

It is important to note that the HV generator in use (the *Minipulse 1*) does not output pure frequencies for all desired ionization frequencies. For a certain

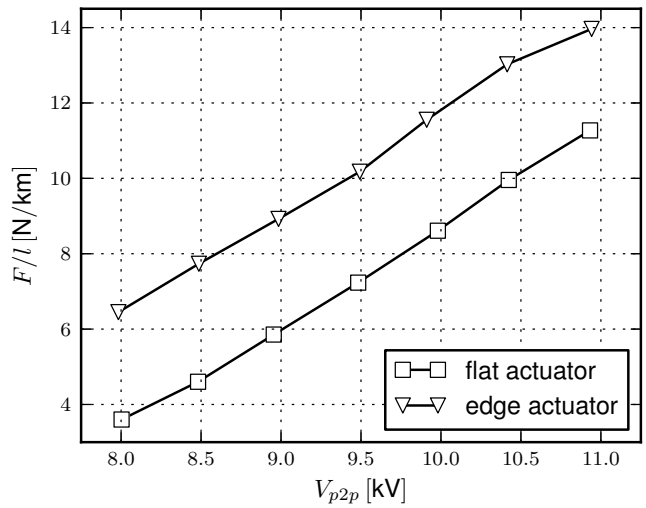

Fig. 4.12: Comparison of flat and edged actuator configurations at $f_{\text{ion}} = 8.00\,\text{kHz}$.

Tab. 4.1: Summary of flow control parameters encountered throughout the study. Electrical power given for $dc = 100\%$. SC: semi circular wing

f_{ion} [kHz]	V_{p2p} [kV]	F [N/km]	act. pos.	wing	c [m]	U_∞ [m/s]	C_μ [%]	dc [%]	P_{el} [W/m]
8.00	10	11.8	LE TE	2.5D, rect.	0.15	2.0	0.65	20	160
8.00	10	11.8	LE TE	2.5D, rect.	0.15	2.0	3.25	100	160
4.75	8	4.3	LE TE	3D, rect.	0.3	2.0	0.12	20	45
4.75	8	4.3	LE TE	3D, rect.	0.3	2.0	0.59	100	45
4.75	8	4.3	LE TE	3D, rect.	0.3	4.0	0.15	100	45
4.75	8	4.3	TE	3D SC	0.3	2.0	0.69	100	45
4.75	8	4.3	TE	3D SC	0.3	4.0	0.18	100	45
4.75	8	4.3	LE	3D SC	0.3	2.0	0.24	20	45

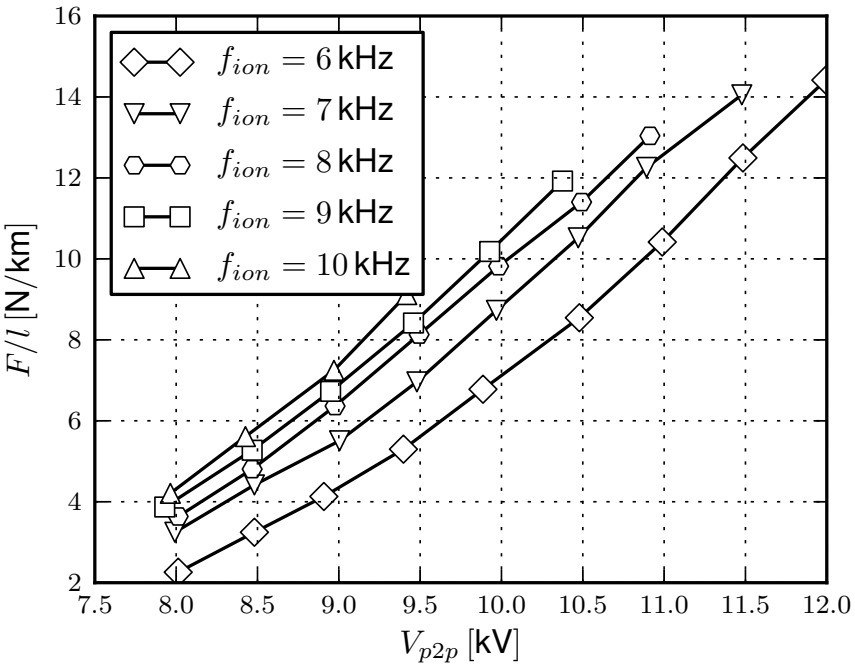

Fig. 4.13: Effect of ionization frequency f_{ion} on induced thrust.

electrical load (actuator and supply cabling) the HV generator reaches its maximum amplitude at a certain frequency, the resonance frequency of the system. At this frequency the output HV waveform is an almost pure, i.e. single-frequency, sinusoidal signal. This has to be taken into account when looking at Fig. 4.13, but the general trend of increasing thrust with higher ionization frequencies is still valid. Responsible for the decreasing maximum peak-to-peak voltage is the HV generator characteristic, i.e. at higher frequencies the peak-to-peak voltage cannot be further increased above a certain limit – this is a limitation of the *Minipulse 1* HV generator.

The dielectric material of DBDs is susceptible to erosion Roth & Dai [RD06]. Shown in Fig. 4.14 is a DBD featuring a serrated exposed electrode. In this case the dielectric material was FR4, a fiber-reinforced plastic covered with a thin layer of copper ($\approx 35\,\mu$m thick) on both sides. This material is commonly used in the production of electronic breadboards. After several hours of operation the resin downstream of the exposed electrode eroded, exposing the glass-fibre mesh. In

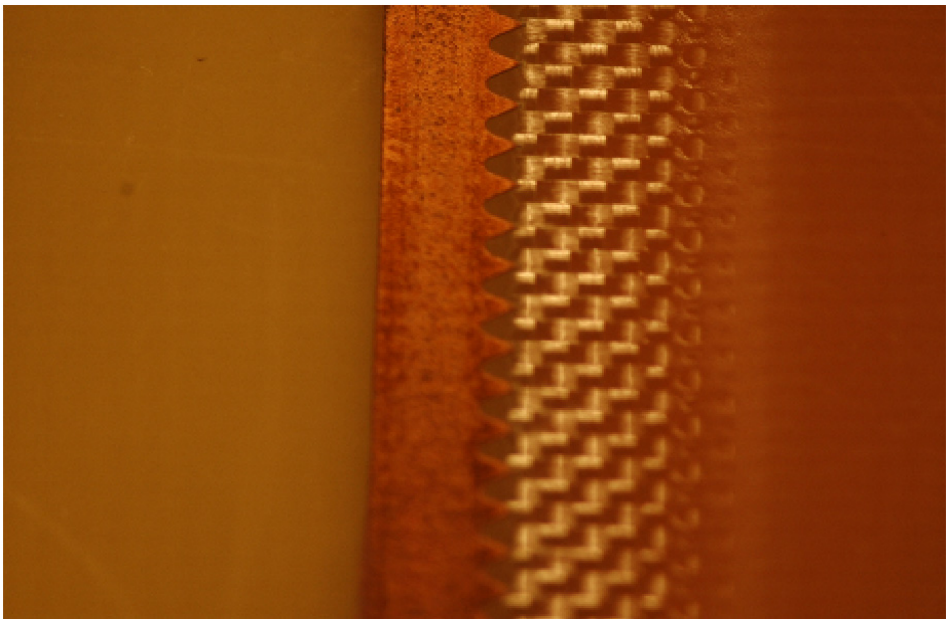

Fig. 4.14: Eroded dielectric material (FR4) downstream of the serrated electrode showing exposed glass fibres (from UTEHS [Ute10]). The actuator was operated for several hours.

the early stages of the erosion process mainly the region in the vicinity of the apexes are affected. In these regions the electric field is strongest, resulting in an increased thermal load for the dielectric material. It is assumed that the erosion is due to high-speed ions impacting into the dielectric. This heats up the material and abrasively degenerates the dielectric. At some point during operation the dielectric would burn through.

Another degenerating effect for the dielectric is the radiation of ultraviolet (UV) light in the plasma discharge region. KAPTON® embrittles after prolonged exposure to UV light. A high UV radiation is assumed to occur in the apex region of serrated electrodes, which speeds up the degeneration of the dielectric.

4.5 Qualitative Characterization of Actuator Output Through Schlieren Imaging

DBD actuators constructed from conductive and dielectric tapes are highly flexible in terms of placement and induced jet direction. By appropriate electrode

arrangement surface normal jets can be generated without the need for slits or grooves in the model under investigation.
Comparable configurations were investigated by Santhanakrishnan et al. [SJS06] and it was concluded that surface-normal plasma induced jets enhance the penetration of the flow field which resulted in enhanced control authority.
A selection of the configurations investigated are shown in Fig. 4.15, which shows electrode configurations and the resulting jet direction as obtained from the Schlieren imaging videos. The color plot depicts the standard deviation of 3000 frames of the high speed (1kHz) Schlieren imaging. In this case a large standard deviation represents regions of large density fluctuations. These were caused by the periodic generation of vortices through the pulsed DBD actuator. For the test cases in figures 4.15a and 4.15b the dielectric (blue) was glass, which at the same time formed the wall to which the actuators were mounted. The electrode beneath the dielectric was grounded while the electrode(s) above the dielectric were connected to the HV generator. Actuators used for flow control on the flat plate wings were derived according to Fig. 4.16.
The induced jet direction in Fig. 4.15a was perpendicular to and away from the wall. The actuator in Fig. 4.15b induced symmetrical blowing tangential to the wall. This resulted in a momentum flux towards the wall from above the actuator. Depicted in Fig. 4.15c is an actuator mounted on the leading edge of one of the wings investigated. It induces a jet tangential to the wings upper surface and represents the de facto standard DBD actuator that was used in this study. A sequence of stills from the high speed Schlieren imaging of this actuator is shown in Fig. 4.17 and discussed in more detail later.

It is interesting that a small modification in the electrode arrangement induced a jet at an angle of $\approx 45°$ to the wings upper surface (figure 4.15d). It was found that the lift increase (ΔC_L) obtainable with this configuration was $\approx 30\%$ less than what was obtained with the reference actuator at otherwise similar operating conditions.
The configuration depicted in Fig. 4.15a yielded $\approx 50\%$ less ΔC_L compared to the reference configuration, while the actuator derived from the one in Fig. 4.15b increased ΔC_L by 4% compared to the reference configuration. The peak to peak voltage was kept constant at 10kV for this comparative study.

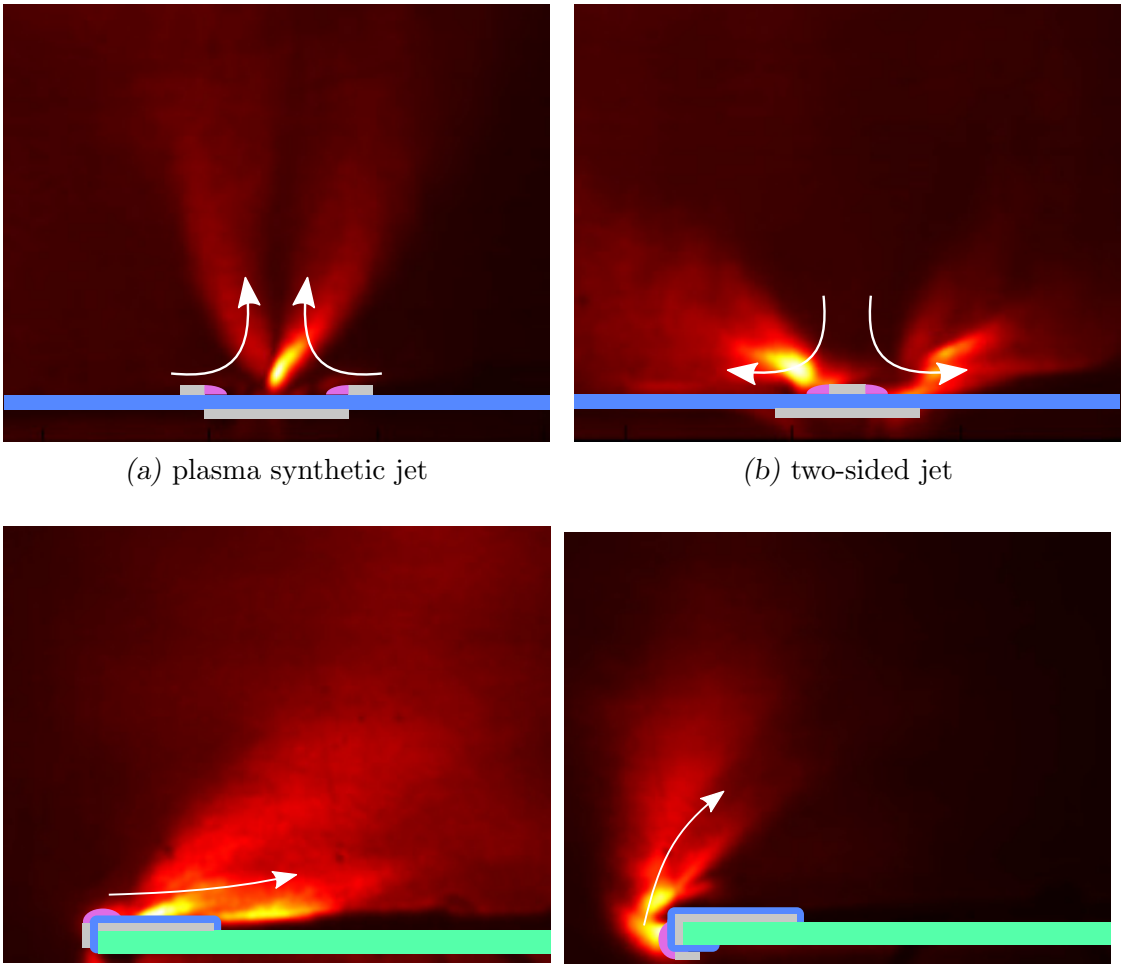

(a) plasma synthetic jet

(b) two-sided jet

(c) tangential wall jet

(d) inclined jet ($\approx 45°$)

Fig. 4.15: Basic actuator configurations investigated with Schlieren imaging. Standard deviation of 3s high-speed (1kHz) video images. Pulsed operation with a modulation frequency of $f_{mod} = 5$Hz at $V_{\mathrm{p2p}} = 10$kV, quiescent air. Colors: blue - dielectric; green - wing/plate; pink - plasma discharge; grey - electrodes.

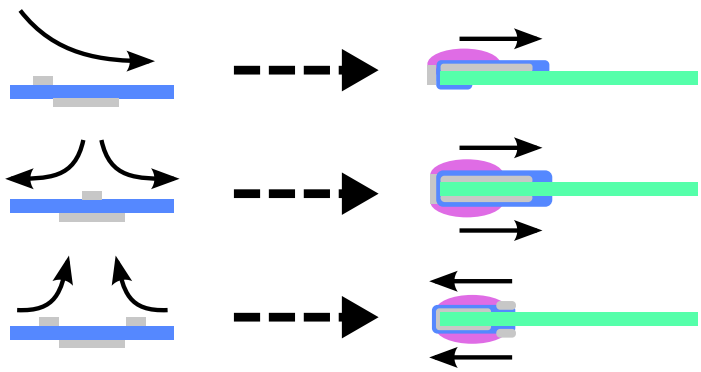

Fig. 4.16: Actuators derived from basic configurations and wrapped around wing leading edges. Tangential wall jet, two-sided tangential wall jet, and two-sided counter-flow jet.

The actuator configuration that was mainly used within the flow control part of this study is shown in Fig. 4.15c and was discussed above in the context of the thrust measurements.

A sequence of stills from the high speed Schlieren imaging is shown in Fig. 4.17. Note that the actuator is oriented upside-down in the image sequence. The actuator was operated in pulsed mode at $f_{\mathrm{mod}} = 5\,\mathrm{Hz}$ and $dc = 87.5\%$. At the beginning of the sequence ($t = 0\,\mathrm{ms}$) the actuator is fired, traces of the last cycle are still visible in the form of a jet that emerges from the trailing edge. A vortex is formed that grows in size and is convected downstream due to the momentum input of the tangential wall jet ($t = 22-65\,\mathrm{ms}$). The vortex has convected down to the trailing edge of the plate at $t = 77\,\mathrm{ms}$ and is barely discernible. At $t = 89\,\mathrm{ms}$ the actuator is still operational and a planar jet detaches from the trailing edge. The tangential wall jet stays attached to the plate during the whole cycle due to the Coanda-effect. It is interesting to observe the development of the detaching jet of the previous cycle, especially at $t = 0 \cdots 41\,\mathrm{ms}$. Within this time-frame the jet is affected by some kind of instability that seems to resemble a Kelvin-Helmholts-type instability. An interaction between the remains of the previous jet and the newly formed vortex takes place at $t = 65\,\mathrm{ms}$. At this point the previous jet is highly bent upwards at the trailing edge.

While taking the high speed Schlieren images on pulsed actuators it was noted

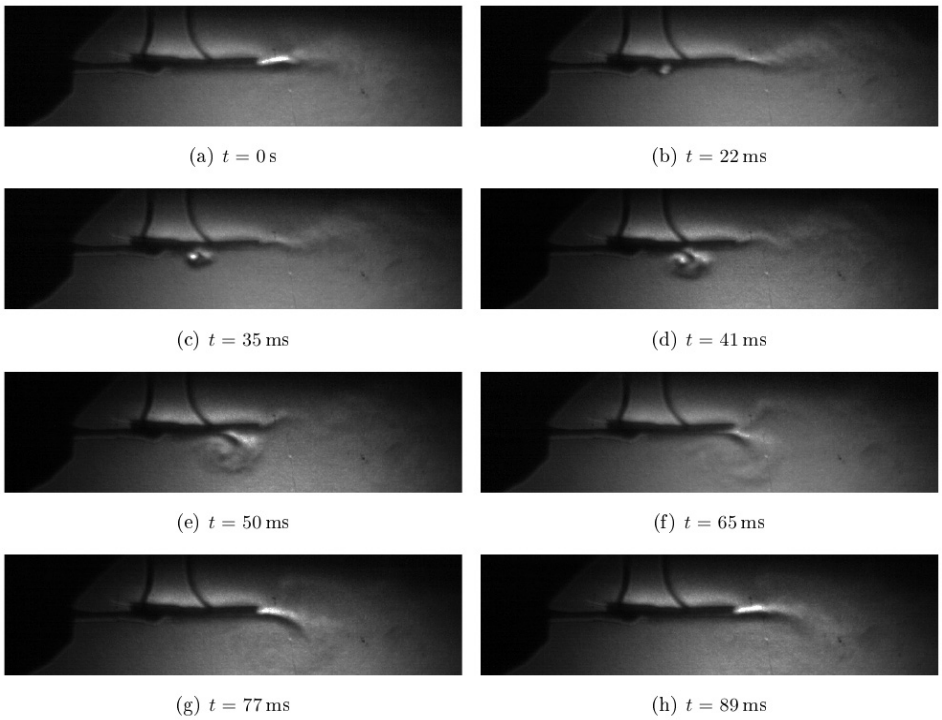

Fig. 4.17: Stills from high speed Schlieren imaging of a DBD in pulsed operation. The actuator with its mounting plate is placed upside-down and operated at $f_{\mathrm{mod}} = 5\,\mathrm{Hz}$, $dc = 87.5\%$, $f_{\mathrm{ion}} = 8\,\mathrm{kHz}$, and $V_{\mathrm{p2p}} = 10\,\mathrm{kV}$.

that, in-between the active cycles, heat accumulated in the vicinity of the electrodes. This heat was then convected by the next cycles jet. The effect of heat release is usually neglected in CFD simulations of plasma flow control, but it could become an important factor at very low Reynolds numbers. However, its role in plasma actuator flow control has not been investigated in the framework of this study.

5. SEMI-SPAN (2.5D) WINGS – THE RISK REDUCTION PHASE

Before applying the actuators to three dimensional flat plate wings they were tested on semi-span wings, i.e. 2.5D wings. Within this risk reduction phase the wings were mounted flush to the wall of a small wind tunnel. This study helped getting familiar with the equipment and gave valuable information on the governing parameter ranges. The results were found to compare favorable to the findings of the flow control study on the three dimensional wings which will be discussed later.

5.1 Experimental Setup for Measurements on 2.5D Wings

The experimental study on the 2.5D wings was conducted in the TU Berlin low speed, closed loop wind tunnel (MoWiKa) with a test section of 0.28 m × 0.4 m. The free stream turbulence level of this wind tunnel was $Tu = 0.15\%$ and the maximum obtainable inflow velocity was $U_\infty = 25\,\mathrm{m/s}$ (Urzynicok [Urz03]). The half span wings were mounted to the tunnels upper wall at a distance of 0.35 hydrodynamic diameters downstream of the nozzle exit (figure 5.2). A gap of approximately 0.5 mm was kept between wing root and wind tunnel wall.
In order to estimate the integral effect of flow control on the wings a custom-made two component force balance was constructed from two strain gauge based load cells. These were salvaged from laboratory scales and had a range of approximately 500 g. They were arranged relative to each other at a 90° angle to allow measuring the normal (F_N) and tangential (F_T) forces of the wing under investigation. Conversion coefficients and linear response were determined through a calibration with precision calibration weights in the range ±500 g. The lift (F_L)

and drag (F_D) forces are then calculated according to (5.1):

$$\begin{aligned} F_L &= F_N \cdot \cos(\alpha) - F_T \cdot \sin(\alpha) \\ F_D &= F_N \cdot \sin(\alpha) + F_T \cdot \cos(\alpha) \end{aligned} \tag{5.1}$$

When flat plate wings are considered (infinite as well as finite wings) the tangential force component is usually neglected. This is a valid simplification because for flat plate wings the tangential force is caused by skin friction only. Classical airfoil sections are characterized by a camber-line and a thickness distribution, which results in a pressure distribution in chord-wise direction. If the pressure was fully recovered at the trailing edge there would not be a drag component due to the pressure distribution. Through losses of kinetic energy within the boundary layers the pressure does not fully recover, which results in a net pressure drag. By modification of the pressure distribution through an appropriate flow control method the pressure drag component can be reduced. Flat plate wings lack camber and therefore modifying the pressure distribution would not alter the pressure drag component at all. Neglecting both the effects of blunt leading and trailing edges, and skin friction the relation between lift and drag, i.e. the aerodynamic efficiency, is fixed by a geometrical relation as will be shown below. Without the aforementioned simplifications the only modifier to improve the aerodynamic efficiency is the skin friction drag.
According to Schlichting [SG06] the friction drag can be estimated for a flat plate with a laminar (5.2) and a turbulent (5.3) boundary layer as follows.

$$C_{D,\,\mathrm{lam}} = \frac{1.328}{\sqrt{\mathrm{Re}}} \tag{5.2}$$

$$C_{D,\,\mathrm{turb}} = 2\left[\frac{\kappa}{\ln(\mathrm{Re})}\,G(\ln(\mathrm{Re}))\right]^2 \tag{5.3}$$

with the von Kármán-constant $\kappa = 0.41$ and $G(\ln(\mathrm{Re})) \approx 1.5$ for the Reynolds number range $10^5 \leq \mathrm{Re} \leq 10^6$. For a flat plate at $\mathrm{Re} = 100\,000$ with two sided boundary layer development the friction drag coefficient is $C_{D,\,\mathrm{lam}} = 0.008$ for laminar flow and $C_{D,\,\mathrm{turb}} = 0.011$ in the turbulent flow case. These numbers are two orders of magnitude smaller than the normal force coefficient C_N of the inclined

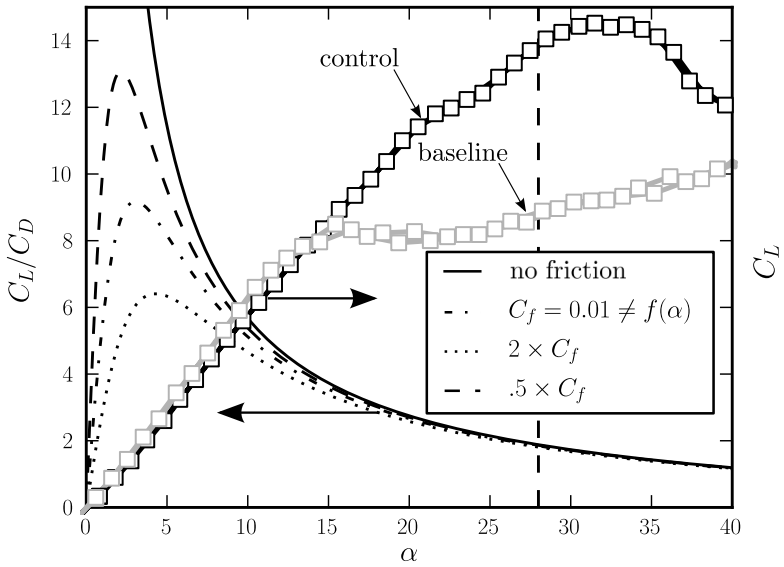

Fig. 5.1: Aerodynamic efficiency of flat plate wings for varying skin friction coefficients. Typical lift curves for baseline and control case shown for reference.

flat plate – friction drag (tangential force) was therefore neglected in the further analysis.

The above equations are therefore simplified and written in dimensionless form as (5.4):

$$\begin{aligned} C_L &= C_N \cdot \cos(\alpha) \\ C_D &= C_N \cdot \sin(\alpha) \end{aligned} \tag{5.4}$$

A trivial but important observation concerns the aerodynamic efficiency C_L/C_D which under the aforementioned assumptions is independent of the aerodynamic coefficients C_L and C_D. It is simply a function of angle of attack α (5.5):

$$C_L/C_D = 1/\tan(\alpha) \tag{5.5}$$

This discussion is concluded by noting that the aerodynamic efficiency of flat plate wings can not be materially improved by the active flow control method that was used in this study. An increase in lift always results in an increase in drag such

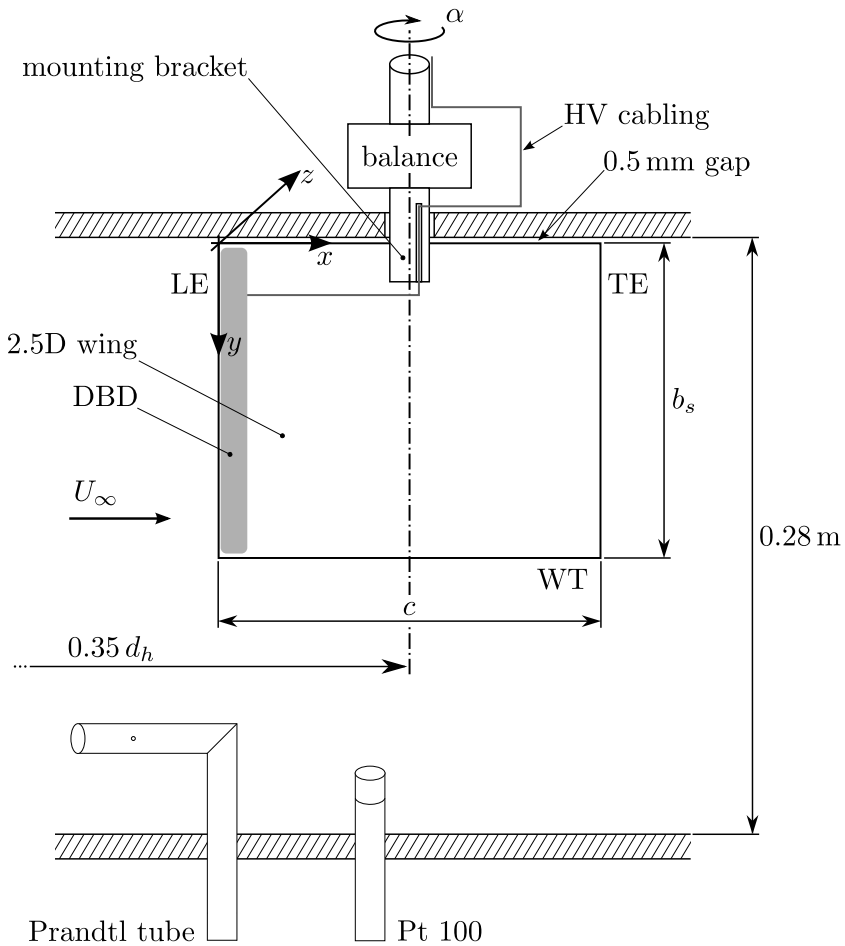

Fig. 5.2: Experimental setup for force measurements on 2.5D wings in closed loop wind tunnel. Schematic view, not to scale. LE: leading edge, TE: trailing edge, WT: wing tip.

that (5.5) is satisfied, no matter what planform shape is used. For this reason this study was focused on lift increase only. In chapter 11 the implications on the selection of the optimum forcing frequency will be discussed.

The wings were mounted at the $x/c = 0.5$ position to an isolating Teflon mounting bracket that was led through the upper wind tunnel wall and had a circumferential gap of approximately 1 mm. In order to reduce the cross-talk through electromagnetic interference to a minimum the high voltage cabling was led around the sensitive part of the balance by a support arm. It was then guided

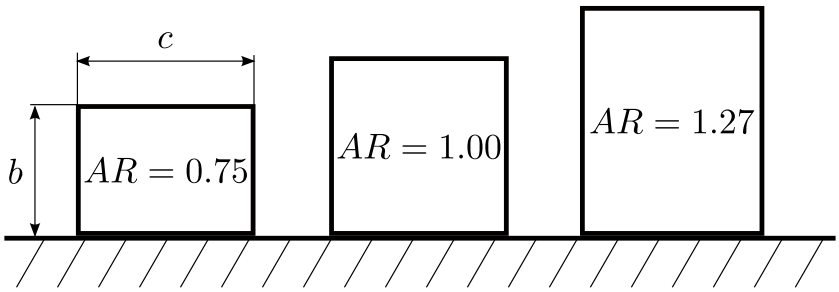

Fig. 5.3: Scale view of the three rectangular semi-span wings that were investigated. $\mathrm{AR}_s = 0.75$, 1.00, and 1.27. Thickness $t = 2\,\mathrm{mm}$, blunt edges.

into the wind tunnel through grooves that were milled into the mounting bracket (see Fig. 5.2) and then led along the wings pressure side to the DBD actuators. Only one (leading edge) DBD is depicted in Fig. 5.2, but during the experimental study DBDs were also attached to the leading edge (LE), trailing edge (TE), and wing tip (WT), respectively. These were then operated individually and in combination and the resulting effects will be discussed in the following sections.
Unless otherwise noted the wings were constructed from FR4 of thickness $t = 2\,\mathrm{mm}$. With a standard chord length of $c = 0.15\,\mathrm{m}$ the resulting thickness to chord ratio of the wings was $t/c = 1.3\%$. The semi-span length ranged from $b_s = 0.112\,\mathrm{m}$ to $0.191\,\mathrm{m}$ corresponding to semi-span aspect ratios of $\mathrm{AR}_s = 0.75$ to 1.27 (figure 5.3), where AR_s is defined according to (5.6).

$$AR_s = \frac{b}{c} = \frac{b^2}{A} \tag{5.6}$$

All edges of the wings were left blunt. The wing coordinate system is centered at the intersection of leading edge and wing root (see Fig. 5.2). Coordinates are given as fractions of chord length x/c and semi-span y/b_s, respectively.
The free stream velocity U_∞ was measured by a Pitot-static tube in connection with a differential pressure transducer (MKS Baratron with $\pm 100\,\mathrm{Pa}$ range). The velocity was adjusted with the wing at $\alpha = 0°$. The free stream temperature was measured by a 4-wire Pt100 temperature probe.
The data presented has not been corrected for wind tunnel blockage effects.

5.2 Baseline Semi-span Wing Characteristics

Initially the semi-span wings were investigated without flow control. This was done to gain an understanding of the specific wings characteristics and to compare the results to data published in the literature. A direct comparison of lift curves can not be performed, though, because of a lack of published lift curves for low aspect ratio *semispan* wings. The situation is quite different for 3D (fullspan) low aspect ratio wings, which were studied in detail by Mueller et al.[MTS07]. Their data can be directly compared to the measurements on 3D wings conducted in this study and the result is favorable. This will be discussed in further detail in section 7.1 on page 58.

Chord-length-based Reynolds numbers for the semispan wings were in the range $10\,000 < \mathrm{Re} < 50\,0000$, with the majority of experiments conducted at $\mathrm{Re} = 20\,000$. Within this range the experimental results were found to be independent of Reynolds number, i.e. the deviations in α_{stall}, $C_{L,\max}$, and $C_{L\alpha}$ were less than 1%.

The baseline lift curves together with the aerodynamic efficiency are shown in figure 5.4. The lift slope $C_{L\alpha}$ of all the wings is smaller than the maximum of $2\,\pi$ that is predicted by inviscid theory for infinite flat plate wings. Typical for wings of differing aspect ratios the lift curve slope increases with aspect ratio. Note that the lift slope of the smallest aspect ratio wing ($\mathrm{AR}_s = 0.75$) is non-linear just before α_{stall}. This quadratic lift term is attributed to tip vortex effects (see Hoerner [HB85]) and was also observed by Pelletier & Mueller [PM00] for a range of low aspect ratio wings.

The highest aspect ratio wing $\mathrm{AR}_s = 1.27$ has a linear lift curve prior to stall, the largest lift slope $C_{L\alpha}$, and obtains the highest $C_{L,\max}$ of the three aspect ratios. For this wing the lift is produced mainly by circulation and the tip vortex effect is small compared to the wings with lower aspect ratio. Note the smoothing of stall and the increased α_{stall} with decreasing aspect ratio, again this is caused by the influence of the wing tip vortex.

Apart from the rectangular planform shapes several other planforms were investigated in this study. These include the semi circular, elliptical, and Zimmerman [Zim32] wings. The inverse Zimmerman wing is obtained by mirroring the Zim-

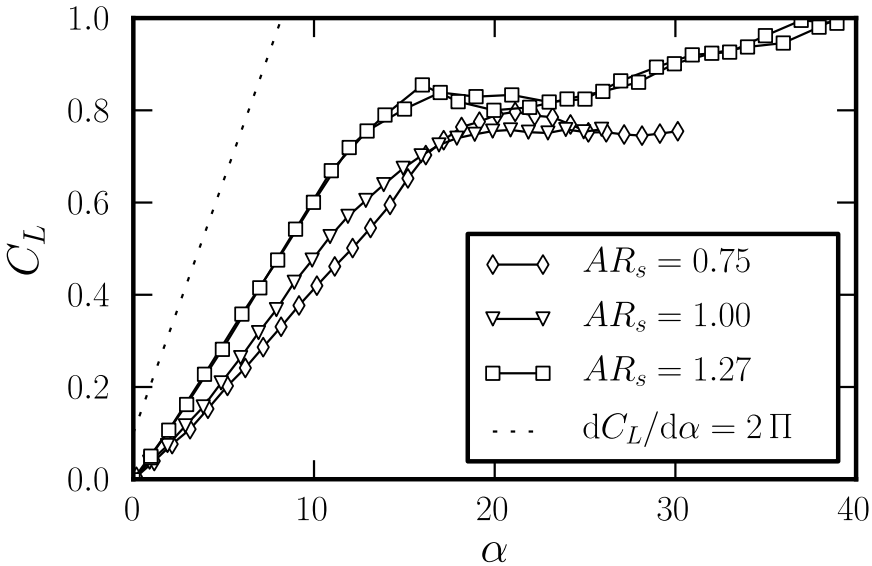

Fig. 5.4: Baseline lift curves and aerodynamic efficiency of wings at $Re = 20\,000$. Dotted line depicts the inviscid theory lift slope of $2\,\pi$.

merman wing at its 25% chord line.

The aforementioned planform shapes are under consideration for the use on MAVs (see [MKIS07]). On the non-rectangular planform wings two different aspect ratios were studied, $\mathrm{AR}_s = 1.00$ and 1.27. Note that a semi circular wings geometry does not allow for aspect ratio variations – the aspect ratio is always $\mathrm{AR} = 8/\pi$ and $\mathrm{AR}_s = 4/\pi$ for full span and semi-span wings, respectively. The semi circular planform is of interest because of the continuous transition of the leading edge into the wing tip. This results in a continuous and static LE/WT vortex bearing similarities to a delta wing vortex system. DBD actuators are unique in the sense that they allow a continuous forcing along the LE/WT of the semi circular wing. This would not have been possible with traditional flow control actuators.

Consider Fig. 5.6 for a comparison of the baseline lift curves of these non-rectangular planform wings. All the wings have similar aerodynamic characteristics with small differences in $C_{L\alpha}$ and a $C_{L,\max}$ between 0.75 and 0.85. The steepest lift curve is observed for the elliptical planform wing with $\mathrm{AR}_s = 1.27$.

It is interesting to note that hysteresis effects were not observed on any of the wings under investigation, neither with nor without flow control.

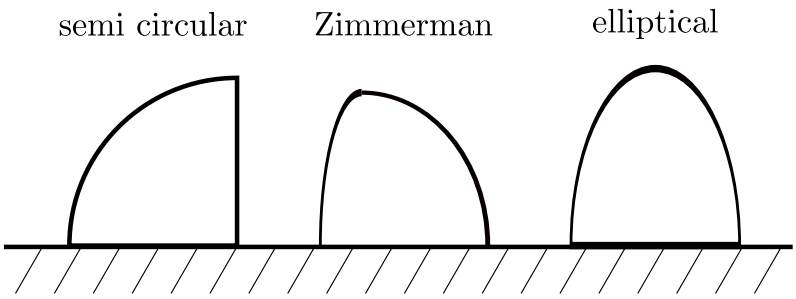

Fig. 5.5: Investigated non-rectangular planform shapes. Swapping the leading and trailing edges of the planform in the center results in the inverse-Zimmerman wing.

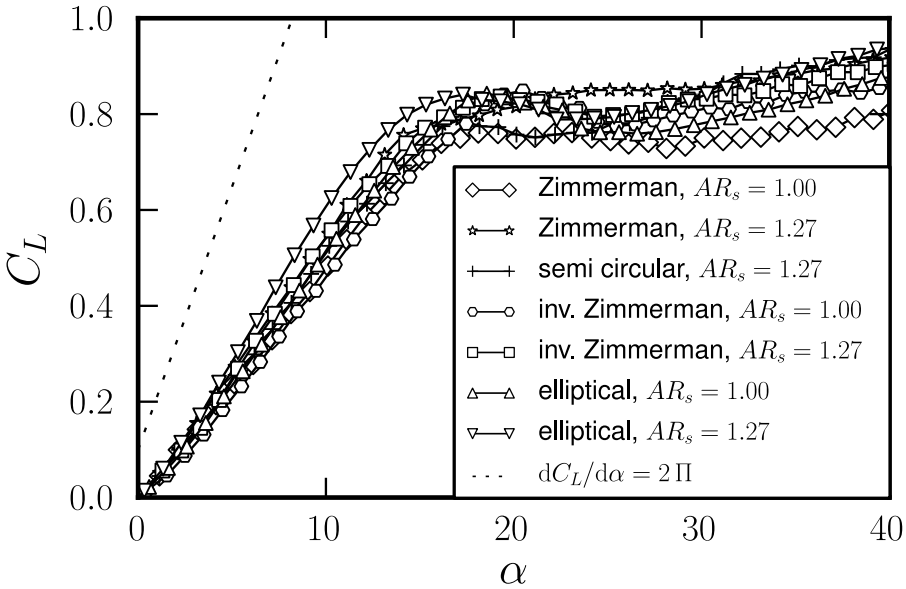

Fig. 5.6: Non-rectangular planform shapes. Baseline lift curves at Re = 20 000. Dotted line depicts the inviscid theory lift slope of $2\,\pi$.

6. FLOW CONTROL ON 2.5D WINGS

6.1 Experimental Procedure

In this section the findings of the flow control study on semi-span wings will be discussed. The DBD actuators were applied to the leading edge, trailing edge, and wing tip, respectively. They were operated individually and, in some cases, in combination. The latter was done in an attempt to further increase the lift gain. A number of different electrode configurations and their effect on the flow control goal was investigated. The parameters governing the actuators induced force and thus jet velocity were discussed in section 4.4 on page 23 et seqq.. A major finding of this actuator calibration study was that the induced force F of a given DBD actuator is a function of the applied peak-to-peak voltage V_{p2p}. The results were found to be reproducible for different batches of actuators. The deviations in force for a given V_{p2p} were less than 5%. Therefore experiments on different wing planforms and with varying actuation locations could be conducted with reproducible flow control parameters by simply monitoring V_{p2p} with an oscilloscope.

6.2 Definition of the Momentum Coefficient

In flow control studies it is common practice to define a momentum coefficient C_μ of actuation. This allows the comparison of different studies or different kinds of actuators by estimating the ratio of momentum that is introduced by the actuator and the momentum of the flow about the model under investigation itself. The general definition of C_μ is (6.1):

$$C_\mu = \frac{J_{\text{jet}}}{1/2\, A_{\text{ref}}\, \rho_\infty\, U_\infty^2} \tag{6.1}$$

with the jet momentum J_{jet} and the reference area $A_{\text{ref}} = b \cdot c$. The momentum coefficient was estimated by an actuator calibration according to the procedure described in chapter 4.3. Rewriting (6.1) to conform to the parameters used in the calibration study yields (6.2):

$$C_\mu = \frac{dc\, F\, b_{act}}{1/2\, b_s\, c\, \rho_\infty\, U_\infty^2} \tag{6.2}$$

with the duty cycle dc, the induced thrust F per length (at $dc = 100\%$), and the actuator length b_{act}. For a given operating point (f_{ion}, V_{p2p}, U_∞, ...) the momentum coefficient of a LE or TE actuator is independent of the wing span, because in most cases $b_{\text{act}} = b_s$.
The actual momentum coefficient will be mentioned for each specific configuration, but as an example for the typical magnitude of C_μ throughout this study the edged actuator according to Fig. 4.11 is considered at a free stream velocity of $U_\infty = 2\,\text{m/s}$ and a duty cycle of $dc = 20\%$ at $V_{p2p} = 8\,\text{kV}$. According to (6.2) this results in a typical momentum coefficient of $C_\mu = 0.24\%$.

6.3 Variation of Actuation Frequency

To determine the actuation frequency that results in the largest lift increase $(\Delta C_L)_{\text{max}}$ a frequency scan was performed for each new actuator location. At a post-stall angle of attack the modulation frequency f_{mod} was varied while keeping V_{p2p} and dc (and therefore C_μ) constant. The reduced forcing frequency F^+ where the lift increase ΔC_L reaches a maximum was termed the *optimum reduced forcing frequency* F^+_{opt} or F^*_{opt}, depending on the length scale that was used in normalizing the frequency.
Similar to the definition of the Strouhal number $\text{St} = f \cdot L/U_\infty$ the reduced (or dimensionless) forcing frequency is defined as (6.3):

$$F^+ = \frac{f_{\text{mod}} \cdot c}{U_\infty} \tag{6.3}$$

Within this study low frequency actuation at $F^+ = \mathcal{O}(1)$ was applied. The lift increase is therefore strongly dependent on the actuation frequency. Higher actuation

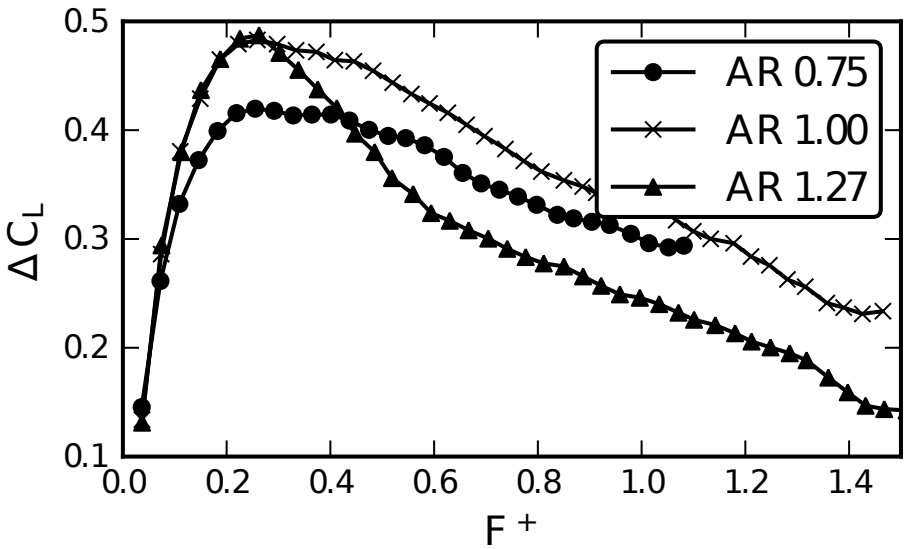

Fig. 6.1: Frequency scan data for LE actuation on rectangular planform wings with varying aspect ratio. Re = 20 000, $\alpha = 32°$, $V_{p2p} = 10\,\mathrm{kV}$, $dc = 20\%$, and $C_\mu = 0.5\%$.

frequencies of $F^+ = \mathcal{O}(10)$ reportedly result in a lift increase that is independent of frequency (see DeSalvo et al. [DWG11]). Actuation at $F^+ = \mathcal{O}(10)$ was tested on a rectangular planform wing by Holst [Hol09] and resulted in a ΔC_L that was an order of magnitude smaller than what was obtained at $F^+ = \mathcal{O}(1)$. Consider Fig. 6.1 for the frequency dependency of lift increase for varying aspect ratio wings at a post-stall angle of attack of $\alpha = 32°$. A leading edge DBD actuator was applied to the wings and the momentum coefficient was kept constant at $C_\mu = 0.5\%$. At $\alpha = 32°$ a ΔC_L of 0.48 was obtained for the $\mathrm{AR}_s = 1.00$ and 1.27 wings and 0.42 for the $\mathrm{AR}_s = 0.75$ wing. All wings reached $(\Delta C_L)_{\max}$ at the same reduced frequency of $F^+_{\mathrm{opt}} = 0.24$. With increasing AR_s the bandwidth of beneficial forcing frequencies became smaller. With increasing aspect ratio the flow field resembles more and more the flow about a two dimensional section. The three dimensionalities introduced by the tip vortex become less important. Leading edge actuation triggers the formation of span-wise structures which are convected downstream (see chapter 10.5). For an infinite wing these structures would have a common convection velocity which is equivalent to a narrow-band

vortex passage frequency. When the flow field is distorted by tip vortex effects this passing frequency can no longer be expected to be constant along span. The idea of a span-wise variation of convection velocity results in a variation of optimum forcing frequency along span, resulting in a broader range of optimum forcing frequencies.

As already mentioned the frequency scans above were performed at a post-stall angle of attack of $\alpha = 32°$. F^+_{opt} generally varies with angle of attack (Nagib et al. [NKRD06], Wygnanski [Wyg04]) due to the dependency of the size of coherent structures on the generating geometry. This variation with incidence was investigated by performing frequency scans at several angles of attack (see Fig. 6.2). Shown in the top part of Fig. 6.2 are three frequency scans that were performed at $\alpha = 26°$, $29°$, and $32°$, respectively. Of note is the variation of F^+_{opt} with angle of attack (see table 6.1). As α is increased F^+_{opt} decreases. The shedding frequency of bluff bodies is known to scale with the transverse height of the body (Hucho [Huc02], Williamson [Wil96]). For stalled airfoil flows the natural shedding frequency is also found to scale with the transverse height (see Leder [Led92], p. 10). At $\alpha \leq \alpha_{\text{stall}}$ two shear layers can be observed, one emanating from the leading edge and the other from the trailing edge. The transverse distance of these two shear layers is proportional to $c \cdot \sin(\alpha)$. It is therefore the representative length scale for normalizing the forcing frequency in flows with $F^+ = \mathcal{O}(1)$. The resulting dimensionless frequency was termed F^*. It is defined according to (6.4) and is also listed in table 6.1.

$$F^* = \frac{f \cdot c \cdot \sin(\alpha)}{U_\infty} = F^+ \cdot \sin(\alpha) \tag{6.4}$$

In the lower half of Fig. 6.2 the frequency scan data for the three angles of attack was scaled with F^*. Note that $(\Delta C_L)_{\text{max}}$ is now obtained at $F^*_{\text{opt}} = 0.12$ for all three angles of attack. Furthermore for the frequency range $F^* \leq F^*_{\text{opt}}$ self similarity is observed. The deviation of the $\alpha = 32°$ case near $F^* = 0.1$ is due to the wing operating in stalled condition already (i.e. α_{stall} is reached in the control case). A reduction of ΔC_L was observed for increasing α at $F^* > F^*_{\text{opt}}$ (figure 6.2). A possible explanation is the increased distance of the shedding span-wise vortices

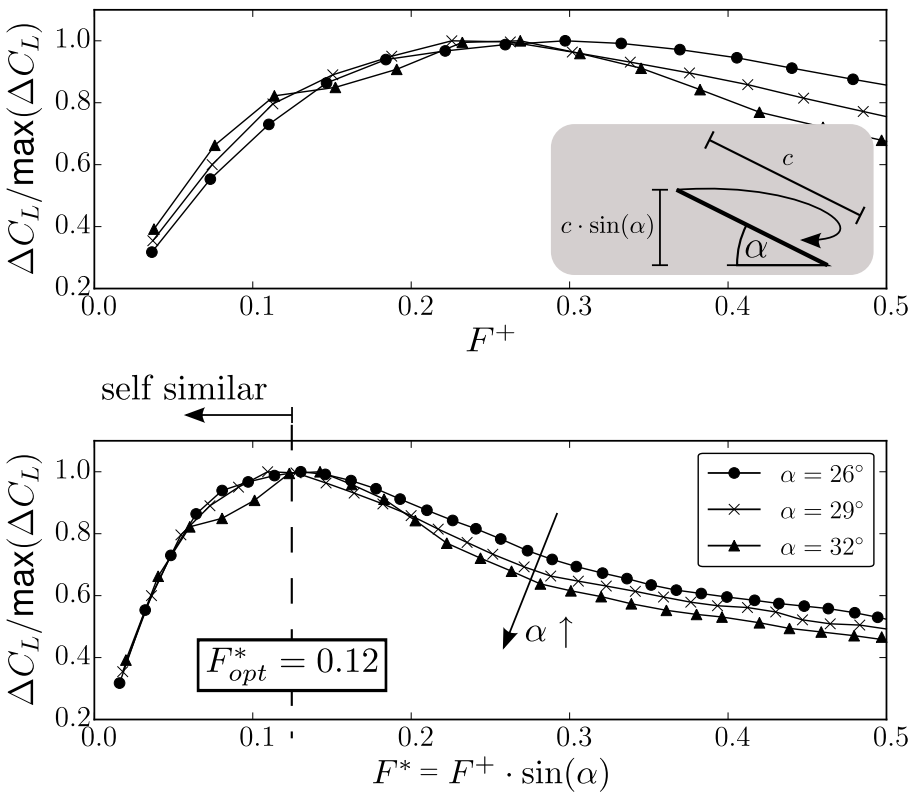

Fig. 6.2: Dependency of F^+_{opt} on angle of attack (top) and effect of using transverse height $c \cdot \sin(\alpha)$ for the frequency scaling. $\text{AR}_s = 1.27$ rectangular planform wing at $\text{Re} = 20\,000$. geometric relations depicted in inset figure.

α	F^+_{opt}	F^*_{opt}
26°	0.27	0.12
29°	0.25	0.12
32°	0.23	0.12

Tab. 6.1: Optimum reduced forcing frequencies for several angles of attack. Data from Fig. 6.2.

from the wings upper surface at higher angles of attack.

This frequency scaling was applied to the experimental results of SCHÜLE ET AL. [SGP08], who applied DBD flow control to two dimensional wings equipped with Gurney flaps for Re $\leq$ 10 000. The Gurney flaps were unusually large with heights of up to $h_G = 20\%\, c$. Re-scaling SCHÜLES frequency scan data as described above under the consideration of the Gurney flap height resulted in a universal optimum reduced frequency of $F^*_{\text{opt}} = 0.12$ (see VEY ET AL. [VGNP10]).

The topic of frequency scaling will be re-addressed in chapter 11, where a local reference velocity will be used in the non-dimensionalization of the forcing frequency.

6.4 Variation of Duty Cycle

Flow control by periodic excitation is known to be more effective and efficient than continuous blowing (refer to GREENBLATT & WYGNANSKI [GW00] for a review). This is illustrated by the duty cycle scan shown in Fig. 6.3. The baseline case is represented by $dc = 0\%$ and $dc = 100\%$ is the analogous to continuous blowing. In-between these extremes is the range of periodic excitation at varying duty cycle. As the duty cycle approaches the steady blowing limit ($dc = 100\%$) the lift goes down. The largest values of C_L were obtained at duty cycles around $dc = 20\%$. Though even at lower duty cycles effective control would be possible $dc = 20\%$ was chosen for this study as a conservative value.
Note that power consumption scales directly with duty cycle. Going down to $dc = 5\%$ would mean a reduction in power by a factor of four. At the same time the momentum coefficient would be reduced by a factor of four without a significant detrimental effect to the flow control effectiveness.

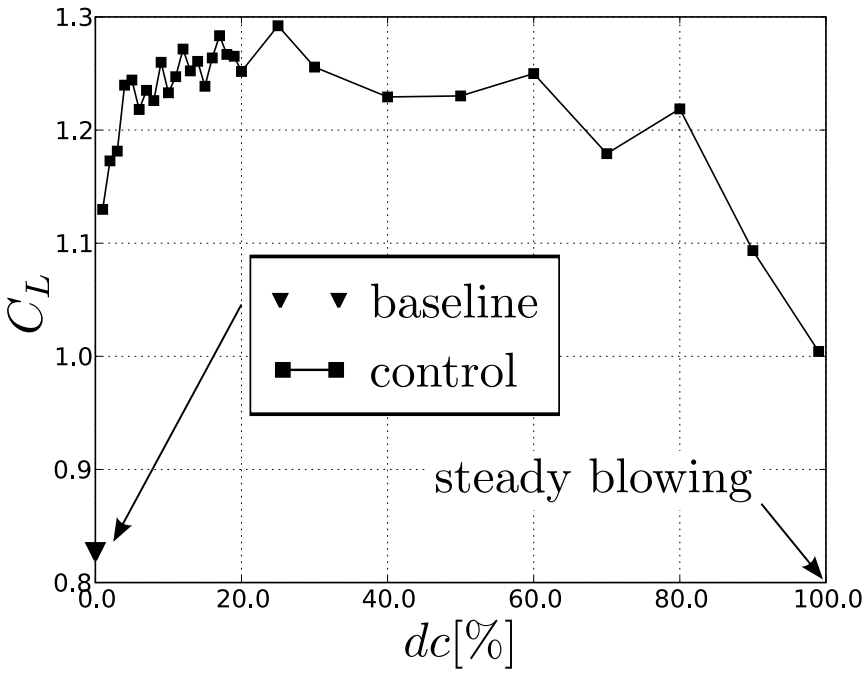

Fig. 6.3: Duty cycle scan on flat plate wing at F^*_{opt}.

6.5 Results of the Flow Control Study on 2.5D Wings

6.5.1 Leading Edge Actuation on Rectangular Plan-forms

The most effective location for flow control on the flat plate wings was found to be directly at the leading edge. This is shown in Fig. 6.4 for the three rectangular planform wings at Re = 20 000. The DBD actuator was of the edged type and is shown in the inset of the figure. This actuator configuration generated a tangential wall jet along the wings suction side. The momentum coefficient was $C_\mu = 0.5\%$ for all three wings. The according baseline lift curves are shown for reference in a shaded color. Control was applied at $F^* = F^*_{\text{opt}} \neq f(\alpha)$. At pre-stall angles of attack the lift curves were not materially altered through actuation. The main effect of actuation was an increase in both α_{stall} and $C_{L,\,\max}$ through a continuation of the lift curves.

The maximum lift increase of $\Delta C_L = 0.6$ was obtained with the $\text{AR}_s = 1.27$ wing. This was accompanied by a shift of α_{stall} from 16° to 32°. Typical for wings with differing aspect ratios the largest $C_{L,\,\max}$ is found on the highest aspect ratio wing while the largest α_{stall} is reached by the lowest aspect ratio wing.

6.5.2 Comparison of Leading Edge and Wing Tip Actuation Locations

The importance of the wing tip vortices for the flow about a low aspect ratio wing and the additional quadratic lift term that arises through the tip vortices has already been mentioned above. Therefore it seemed reasonable to apply actuators also to the wing tip region. The experiments were conducted on the $\text{AR}_\text{s} = 0.75$ wing at Re = 20 000. Different actuator configurations were tested according to Fig. 4.16 (also see Holst [Hol09]). Of the tested actuators the largest lift increase was obtained with an edged actuator that was blowing tangentially along the wings pressure side (see inset in Fig. 6.5). The results are shown in Fig. 6.5 where the WT actuator is compared to a LE actuator of the same configuration (i.e. edged actuator on pressure side).

For both control locations the actuators were operated at the same peak to peak voltage of $V_{p2p} = 10\,\text{kV}$. This resulted in a slightly higher momentum coefficient for the wing tip actuator. These were $C_\mu = 0.5\%$ and 0.67% for LE and WT actuation,

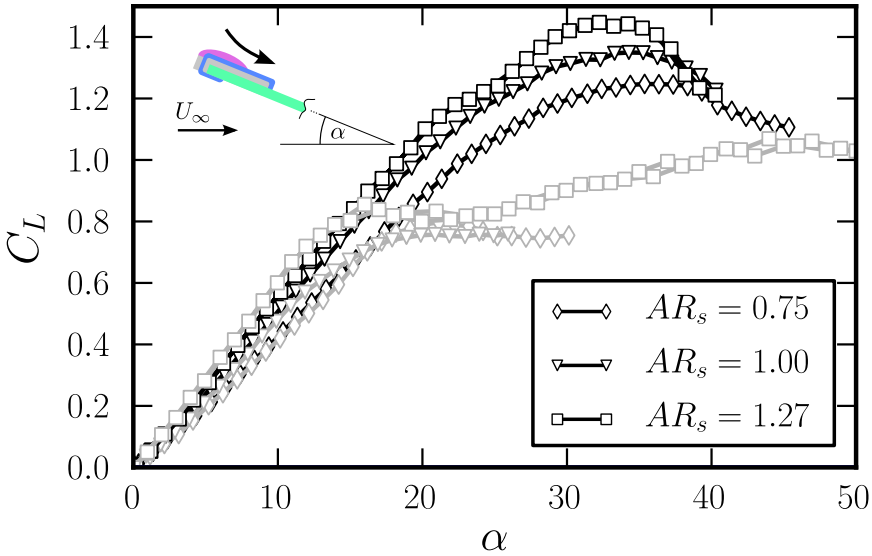

Fig. 6.4: Comparison of LE control effect on the three rectangular planform shapes at Re = 20 000. Baseline lift curves shown shaded for reference. Actuator configuration shown in inset Fig. at upper left. $C_\mu = 0.5\%$, $F^* = F^*_{\text{opt}} = 0.12$.

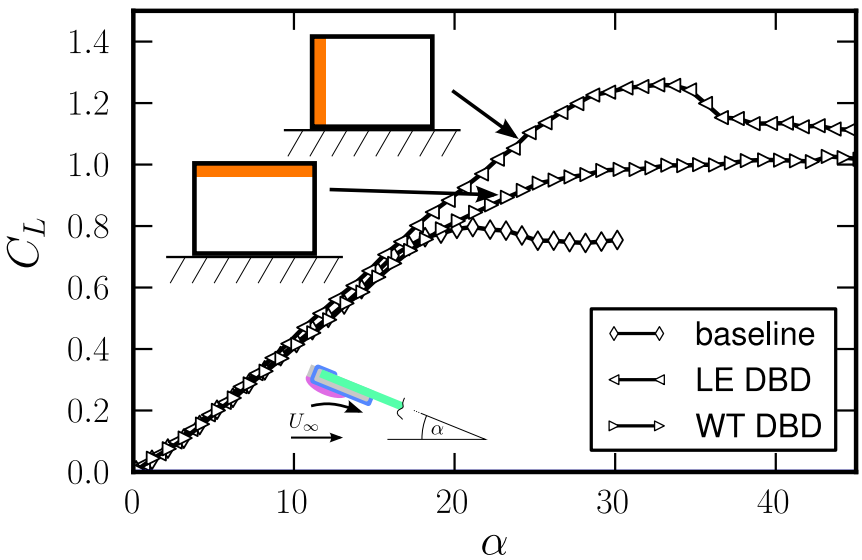

Fig. 6.5: Different control locations (LE & WT actuator) compared to baseline case of $\text{AR}_\text{s} = 0.75$ wing at Re = 20 000. Actuator (shown in inset) operating in pulsed mode on wings pressure side.

respectively. In spite of the higher momentum coefficient the lift increase due to WT actuation ($\Delta C_{L,max} = 0.2$) was found to be smaller than what was obtained by LE actuation ($\Delta C_{L,\max} = 0.5$). Note the change in stall characteristics. WT actuation resulted in a more gentle stall behavior than stall with LE actuation.
No significant difference in maximum lift or stall angle of attack was observed when comparing the lift curves for LE actuation with the actuator placed on the pressure side (figure 6.5) and on the suction side (figure 6.4).

7. FLOW CONTROL ON 3D WINGS

Following the detailed experimental study on the semi-span wings some selected cases were studied on three dimensional wings. The study on the 3D wings was focused mainly on obtaining frequency scan data, investigating phase shifted operation of two actuators (at LE & TE), roll control authority tests, flow control on yawed wings, and continuous TE actuation. Additionally a detailed stereo PIV study was conducted in order to investigate the flow field dynamics (discussed in chapter 10.5). The measurement of lift curves was confined to the baseline cases in order to deduce the angle of attack for the frequency scans from α_{stall}. The experimental setup is depicted in Fig. 7.1. The wings were fixed to a mounting arm and installed vertically in the 1.4 m $\times$ 2 m test section of the TU Berlin large wind tunnel (GroWiKa). A force sensor was integrated into the mounting arm, measuring the normal force on the wing. It was of the same type as in the two component balance that was used for the experiments on the half span wings. The angle of attack was set using the turn table of the main six-component wind tunnel balance. Two wing sizes were studied: small and large wings which had a chord length of $c = 0.15$ m and $c = 0.3$ m, respectively. Aspect ratios were AR = 1.00, 2.00, and 2.66. In addition to the rectangular planforms a semi-circular planform (AR = 2.55) was investigated.

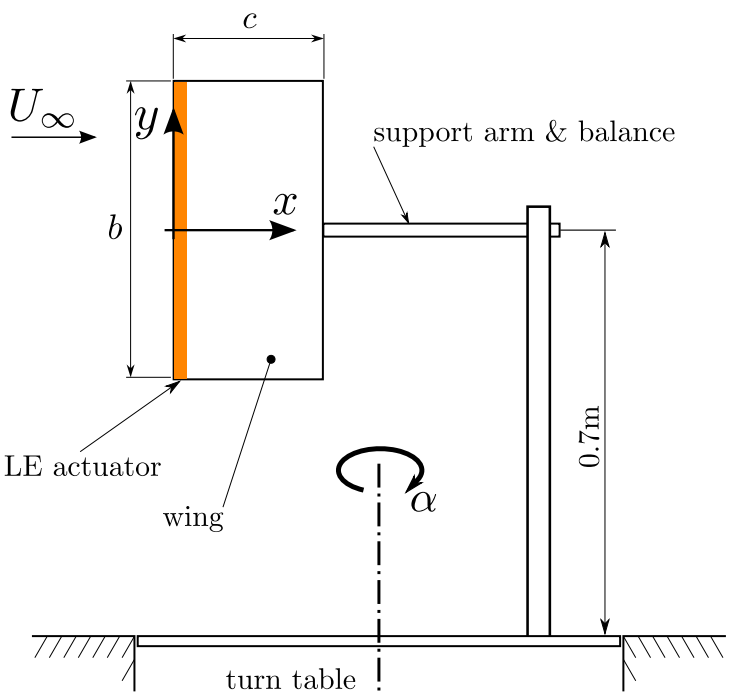

Fig. 7.1: Experimental setup for measurements on 3D wings in 1.4 m × 2.0 m test section.

7.1 Validation of Baseline Lift Curves

In order to validate the measurements on the 3D wings the polars were compared to previously published polars. Extensive polar data for low aspect ratio, rectangular planform wings was published by Mueller et al. [MTS07]. The authors studied 3D wings with $0.5 < \mathrm{AR} < 2.0$ mainly at a Reynolds number of $\mathrm{Re} = 100\,000$. For a direct comparison only the data of the $\mathrm{AR} = 1.0$ and 2.0 wings are suited. Mueller et al. did not perform measurements on an $\mathrm{AR} = 2.66$ wing.

Before the data is compared some differences in the measurement procedures are highlighted below. Mueller et al. used a platform balance to measure lift and drag and a sting balance to measure the wings pitching moment. All of their aerodynamic forces were corrected for solid blockage, wake blockage, and streamline curvature. The maximum blockage correction factors occurred for the $\mathrm{AR} = 2.0$ wing at stall angles of attack. The difference between corrected and uncorrected aerodynamic coefficients was in the range of 10%. Their wind tunnel had a 2 ft × 2 ft section (0.61 m × 0.61 m). Although the authors do not give

the dimensions of their wings explicitly it is deduced from the pictures in their report that the wings span approximately one third of the wind tunnel, resulting in a wing span of approximately $b = 0.2\,\mathrm{m}$ (also depending on AR). The wings featured elliptical leading and trailing edges, while in this study the wings had blunt leading and trailing edges.

The 3D wing measurements presented within this thesis were conducted in a 1.4 m × 2.0 m wind tunnel and the smaller scale AR = 2.0 model spanned only one fifth of the wind tunnel, resulting in considerably smaller blockage. Because this study was not focused on evaluating the absolute aerodynamic performance of low aspect ratio wings and because blockage effects were considered small no blockage correction was performed and the force measurements are given as uncorrected values. Furthermore only the wings normal force was measured in the 3D wing study. The measurement of the tangential force was omitted because its addition to the lift force is negligible for the purpose of this study. Thus the given C_L values were solely calculated from the normal force component.

First the lift curves for the AR = 1.0 wing are compared in Fig. 7.2a. The pre-stall lift curves compare favorable. Although the data of Mueller et al. reveals slightly higher lift coefficients for $15° < \alpha < 32°$ and also a different lift drop-off characteristic at post-stall angles of attack. The lift drop-off observed in this study is shifted by approximately 5° towards higher angles of attack. A definitive reason for these differences could not be determined. Possible sources could be the different LE/TE shape (elliptical vs. blunt), the different turbulence levels (Mueller et al.: Tu = 0.05%, TU Berlin large wind tunnel: Tu $\leq$ 0.5%, or the different Reynolds number.

Shown in Fig. 7.2b is a comparison of several AR = 2.0 wings. Differences between the two scales of wings ($c = 0.15\,\mathrm{m}$ and $0.3\,\mathrm{m}$) were found to be negligible. Note, though, that the blockage differs by a factor of four between the two scales. Thus the effect of blockage does not materially affect the quality of the measurements here. Also shown in Fig. 7.2b is the lift curve as given by Mueller et al. [MTS07]. The data compares favorable with deviations being $< 3\%$ for $\alpha \lessapprox \alpha_{\mathrm{stall}}$. Somewhat larger deviations can be observed in the post-stall angle of attack range.

In conclusion the baseline lift curves compare favorable to data published in the literature. The fact that two different scales of wings resulted in similar lift

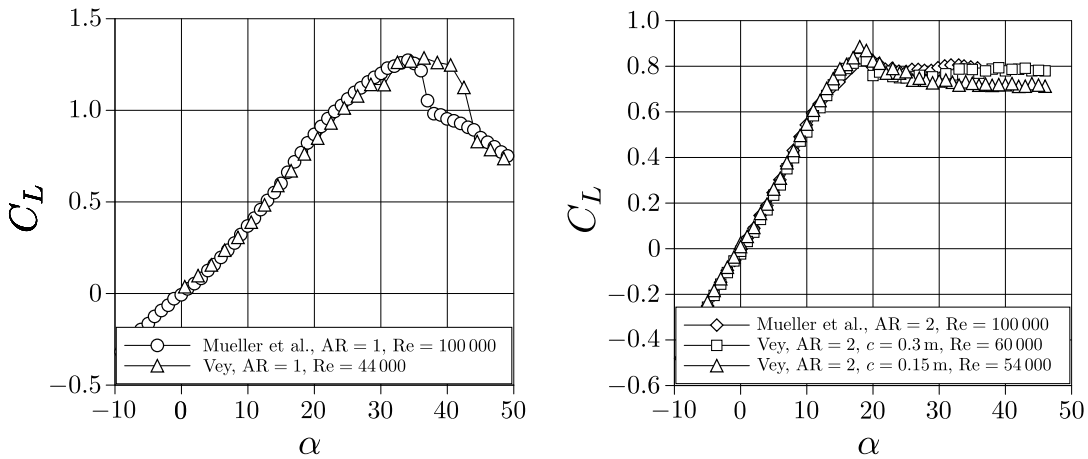

(a) AR = 1.0 rectangular planform wings. *(b)* AR = 2.0 rectangular planform wings.

Fig. 7.2: Comparison of polars of AR = 1.0 and 2.0 wings with polar data published by Mueller et al. [MTS07].

curves supports the decision to neglect wind tunnel corrections. Although only two geometrical configurations could be compared the positive results support the good overall data quality, also for other wing configurations.

7.2 Variation of Actuation Frequency on 3D Wings

The semi-circular planform wing stalled at $\alpha_{\text{stall}} = 13°$ in the baseline case. For the frequency scan shown in Fig. 7.3 the wing was set at a post-stall angle of attack of $\alpha = 20°$. The wing had a chord length at the center-line of $c = 0.3\,\text{m}$ which resulted in a Reynolds number of Re = 35 000. Optimum forcing frequencies were in the range $0.24 \leq F^+ \leq 0.4$. For this wing configuration it was not possible to define a reduced frequency like F^* purely based on the wings geometry. The chord-length varies along the span from 0.3 m at the center-line down to zero at the wing tip. Therefore a representative chord length would either be the mean aerodynamic chord (MAC) according to (7.1) Abbott & von Doenhoff [AD59]

$$MAC = \frac{2}{S} \int_0^{\frac{b}{2}} c(y)^2 \, \mathrm{d}y \tag{7.1}$$

which resulted in a dimensionless frequency of 0.086 or the standard mean chord (SMC) according to (7.2)

$$SMC = \frac{S}{b} \tag{7.2}$$

with a resulting dimensionless frequency of 0.082. It is assumed that neither of the two scalings captures the fluid mechanical mechanism.

The flow field about a semi-circular wing is inherently different from the flow field of a rectangular planform wing of moderate aspect ratio (say AR $>$ 1). The swept-back LE of the semi-circular wing provides a mechanism for vorticity transport similar to delta wings. The vorticity transport along the axis of leading edge vortices and possible means of its control are discussed by Ng [Ng89]. The two leading edge vortices are expected to be stable, which is in contrast to the span-wise vortices which exist on rectangular planform wings. In this case the vorticity transport is established through the (periodic) convection of span-wise vortical structures emanating from the leading edge. The stable vortex system of a semi-circular wing induces a down-wash in the center-line region of the wing through which the size of the separated region is somewhat reduced compared to the case of a rectangular planform, where the width of the wake is proportional to the transverse height of the wing (i.e. $c\,\sin(\alpha)$). In summary the dominant fluid mechanical feature of a rectangular planform shape directly scales with the geometry of the wing, while for a semi-circular wing this is not the case.

The frequency scan data of LE actuation on an AR = 2.66 wing shown in Fig. 7.4 supports the scaling that was introduced with equation (6.4), i.e. the maximum increase in normal force occurs at $F^* = 0.12$. An interesting effect occurs at higher angles of attack approaching (control) stall at $\alpha = 32°$, where a secondary peak develops around $F^* = 0.22$. This is presumably a harmonic of the primary peak though it is not an exact multiple.

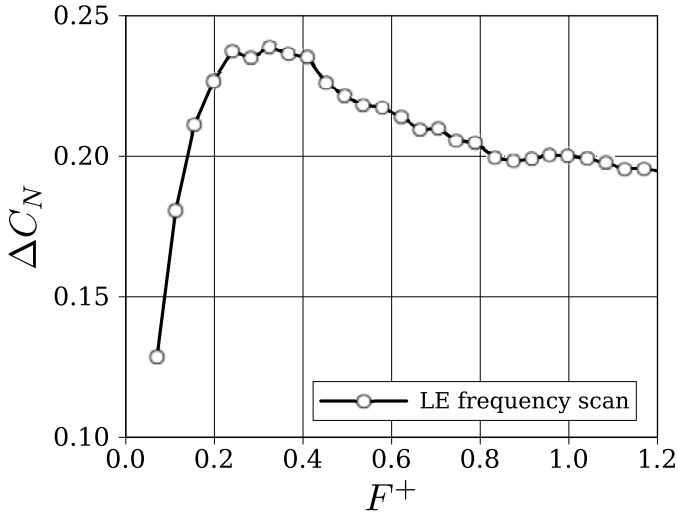

Fig. 7.3: Frequency scan for LE actuation on semi-circular wing. $\alpha = 20°$, Re = 35 000.

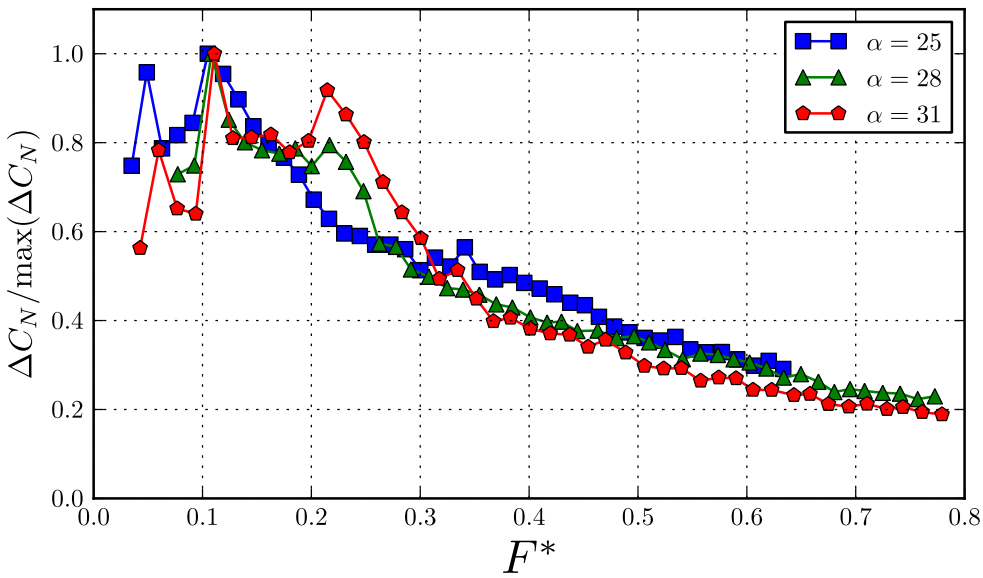

Fig. 7.4: Frequency scan data for three angles of attack. AR = 2.66 rectangular planform, $c = 0.3\,\mathrm{m}$, Re = 35 000, $C_\mu = 0.12$, $\alpha_{\mathrm{stall}} = 16°$.

7.3 Leading Edge and Trailing Edge Actuation on 3D Wings

In this section a new actuation location in the trailing edge region is introduced. Furthermore dual-location actuation is investigated on a rectangular planform wing of AR = 2.66.

Periodic trailing edge actuation on a 2D wing at Re = 300 was investigated numerically by Joe et al. [JCM09]. The authors concentrated their investigation on the optimization of the forcing signal and concluded that a periodic, pulsatile waveform generated the largest lift increase at the lowest momentum coefficient. At $C_\mu = 0.5\%$ the authors obtained a mean lift coefficient of $C_L = 2.5$ with the optimized pulsatile waveform. This study inspired the experimental testing of pulsed actuation in the upstream direction along the wings pressure side. The results of the frequency scan for individually operated LE and TE actuators are shown on the left of Fig. 7.5. With LE actuation alone a maximum increase in normal force of $\Delta C_N = 0.78$ was obtained at $F^+ = 0.23$ which corresponds to $F^* = 0.11$. Note, though, that the resolution of the frequency scan around the optimum reduced forcing frequency is rather coarse. For the phase shift actuation $F^* = 0.12$ was chosen as the modulation frequency of both actuators. Unlike on the semi-span wings ($\mathrm{AR}_s = 1.27$, see Fig. 6.1) a secondary peak was observed in the frequency scan data of both control locations. This peak is more pronounced for the trailing edge actuation location and seems to be a harmonic of the primary peak. In the case of TE actuation $\Delta C_N = 0.38$ was reached at $F^+ = 0.32$ corresponding to $F^* = 0.15$.

Shown on the right hand side of Fig. 7.5 are the results of a phase shift scan performed with both actuators operating at the same modulation frequency of $F^* = 0.12$ ($F^+ = 0.25$). The dashed red line marks the increase in normal force that was realized by LE control alone at the same reduced frequency. The phase shift study aimed at increasing ΔC_N beyond the values obtained by individual control (i.e. beyond $\Delta C_N = 0.68$). The combined actuation resulted in a marginal additional increase in the range $30° \leq \Delta\Phi \leq 210°$ with a maximum of 0.04 for phase shift angles around $\Delta\Phi = 90°$. At twice the energy expenditure and only a marginal beneficial effect phase shift actuation does not seem to be a promising approach to efficient flow control at low aspect ratios. Matters may be different

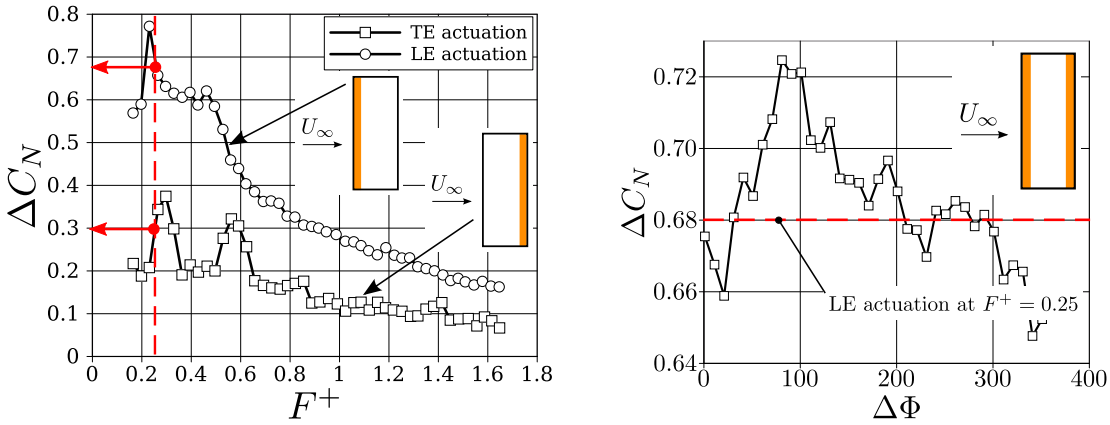

Fig. 7.5: AR = 2.66 wing at Re = 35 000, $\alpha = 28°$. Left: Effect of individually operated LE suction side or TE pressure side actuator. Dimensionless frequency for phase shift scan and respective C_N marked in red. Right: Phase shifted actuation between LE and TE actuator at $F+ = 0.25$ i.e. $F^* = 0.12$. $C_\mu = 0.12$ for each actuator.

for 2D wings or higher aspect ratios.

7.3.1 Lift Increase at Pre-Stall Angles of Attack

With the actuation schemes discussed so far the lift curves at (baseline) pre-stall angles of attack were not materially changed through actuation. Even with actuation the wings still showed the characteristics of a symmetrical section, i.e. $C_{L,0} = 0$.

In order to generate a lifting component the flow around a body needs to be deflected. This deflection of the flow is caused by the circulation around the body or wing. The Kutta condition, which fixes the rear stagnation point at the trailing edge, is satisfied by the appropriate amount of circulation. Manipulating the rear stagnation point results in a modification of lift (i.e. circulation) for a given angle of attack. This can be achieved for example by attaching a Gurney flap to the trailing edge of the wing or by circulation control (CC). The term *circulation control* summarizes flow control schemes that generate lift coefficients above those predicted by inviscid theory Wygnanski [Wyg04]. In this sense CC was applied to a semicircular, three dimensional, flat plate wing by attaching a continuous ($dc = 100\%$) upstream blowing DBD actuator to the wings pressure side at the

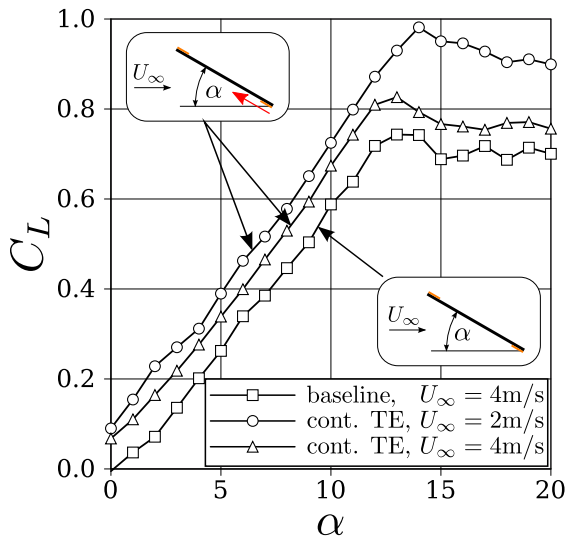

Fig. 7.6: Continuous trailing edge upstream blowing along wings pressure side. Semi-circular wing planform.

C_μ	U_∞	$C_{L,\max}$	ΔC_L	α_{stall}
n.a.	4 m/s	0.75	n.a.	13°
0.69%	2 m/s	0.99	0.24	14°
0.18%	4 m/s	0.81	0.06	13°

Tab. 7.1: Main parameters and results for trailing edge upstream actuation on a semi circular three dimensional wing.

trailing edge. The chord length at the center line was $c = 0.3$ m and the thickness to chord ratio was $t/c = 2\%$.

Consider Fig. 7.6 for the effect of CC on the lift curve. Control was applied at two different free stream velocities $U_\infty = 2$ m/s and 4 m/s corresponding to momentum coefficients of $C_\mu = 0.69\%$ and 0.18%, respectively. Table 7.1 summarizes the results and main parameters. The overall effect of TE upstream blowing is comparable to that of a plain flap in the sense that the lift curve is shifted towards larger values of C_L for increasing C_μ Hoerner [HB85], Anderson [And05].

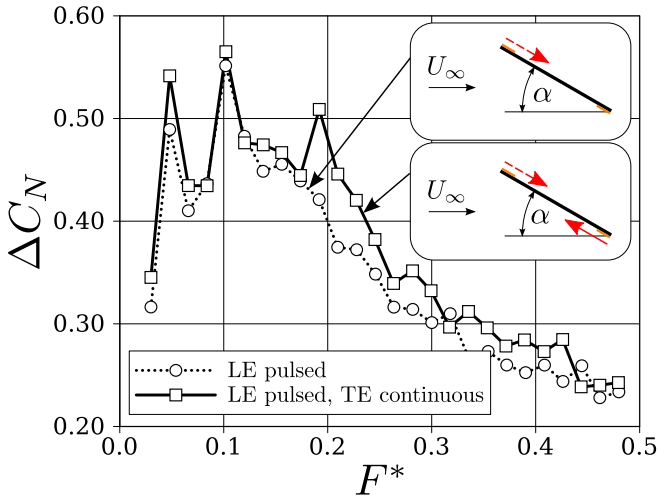

Fig. 7.7: Comparison of LE frequency scans in combination with continuous trailing edge upstream blowing. AR = 2.56, $\alpha = 25°$, Re = 35 000

7.4 Pulsed Leading Edge Actuation Combined with Continuous Trailing Edge Actuation

The final flow control scheme investigated on the 3D wings was the combination of pulsed LE actuation with continuous TE actuation. It was expected that a frequency scan performed on a wing with a continuously operating TE actuator would result in a different optimum forcing frequency. This assumption was deduced from the fact that continuous TE actuation resulted in a significant control effect even at pre-stall angles of attack (see above). The experimental results show that F^*_{opt} was not changed when continuous TE actuation was applied in addition to pulsed LE actuation (figure 7.7). At $F^* \geq 0.18$ a beneficial effect in the sense of a small increase in ΔC_N was observed. This was accompanied by the development of a tertiary peak around $F^* = 0.2$.

7.5 Actuation on Wing Tips

Applying control to the wing tips of the rectangular planform shapes did not have any effect for ARs = 2.00 and 2.56 rectangular planform wings. Only for the AR = 1.00 wing a ΔC_N of 0.1 was achieved Vey et al. [VGP11]. This wing

stalled at $\alpha_{\text{stall}} = 42°$ and the frequency scan was conducted at $\alpha = 47.5°$. The practical value of flow control on these extremely low aspect ratio wings is therefore questionable. At $\alpha > 45°$ the main effect is no longer primarily a *lift*, but rather a *drag* increase.

7.6 Effect of Yaw on Control Authority

The flight envelope of MAVs is characterized by prolonged periods of flight through highly turbulent environments with varying inflow vectors. This results in varying inflow velocity U_∞, angle of attack α, and yaw angle β. From a flight-control point of view an important parameter for control-ability is the wings sensitivity to these varying inflow conditions. When active flow control is considered as a means of roll control and gust alleviation the sensitivity of the control effect to distorted inflow conditions should be as small as possible.
Varying inflow velocity, angle of attack and yaw angle basically have the same effect on the flow control system – the optimum forcing frequency varies.
In an experimental study two flat plate wings with leading edge DBD actuators, a rectangular wing and a semi-circular wing with AR = 2.66, were investigated in the wind tunnel. The yaw angle β was varied between $0° \leq \beta \leq 30°$ while the angle of attack was kept constant at $\alpha = 28°$. The yawed wings and geometric arrangement is shown in Fig. 7.8. Also shown here is a qualitative explanation of how a yawed inflow affects the flow control effect. A simple empirical model to explain the reduced lift increments is developed within the next section.

For each yaw angle a frequency scan was performed. With increasing yaw angle the optimum reduced frequency increases (figure 7.9).

Note that the reduced frequency is scaled by chord length c. A representative length in order to obtain $F^*_{opt}(\alpha, \beta, U_\infty, c) = const$ was not found and calculating a representative inflow velocity by taking $U_\infty \cdot \cos(\beta)$ would increase the divergence of F^+_{opt} with β.
By inspection of Fig. 7.8 for the rectangular planform it is noted that with increasing yaw angle:

- The gray area on the wing that is no longer affected by the span-wise vortices increases.
- The red area where the span-wise vortices no longer directly affect the flow field above the wing increases – structured, lift enhancing vorticity is "spoiled".

These effects might explain the high sensitivity of lift increase on the rectangular

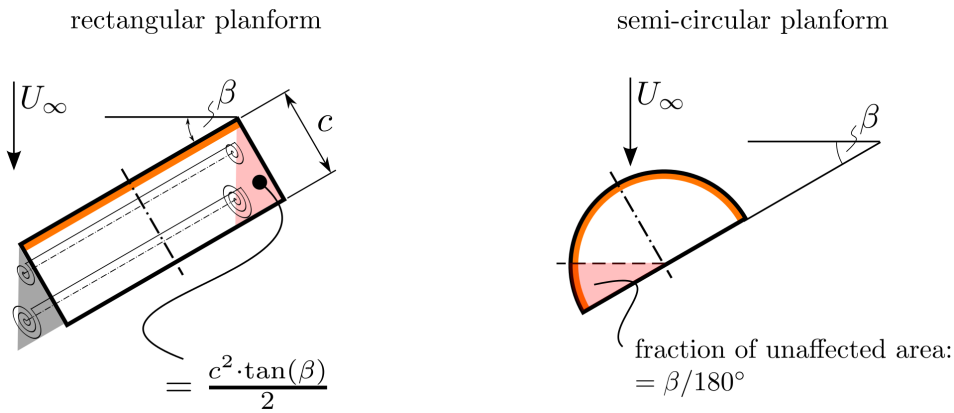

Fig. 7.8: Sketch of yawed wings. Span-wise vortices generated by actuation shown for rectangular planform. Shaded red areas not affected by vortices (segment of circle for semi-circular wing). Structured vorticity spoiled in grey area.

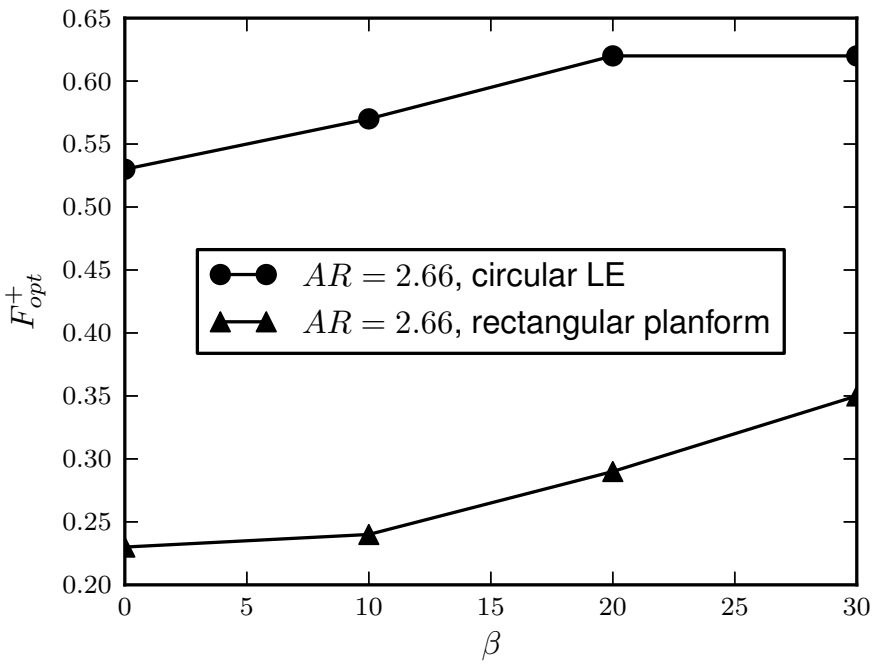

Fig. 7.9: Dependency of optimum forcing frequency F^+_{opt} on yaw angle β for semi-circular wing and rectangular wing planform.

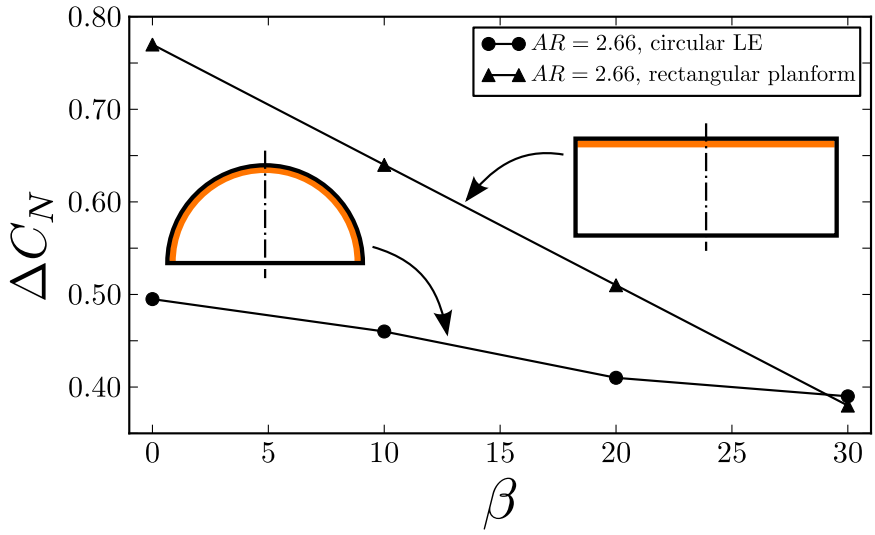

Fig. 7.10: Effect of yaw on control efficiency on two different wing planforms with leading edge DBD actuator. Angle of attack kept constant at $\alpha = 28°$, $Re = 35\,000$.

wing to yawed conditions (figure 7.10). The semi-circular planform shape is less sensitive to yaw, i.e. it has a smaller $\mathrm{d}C_N/\mathrm{d}\beta$. Note that an $AR = 1$ wing at $\beta = 45°$ would transform to a rhombus-wing, bearing some similarities to delta wing configurations.

In the next section the yaw effect will be quantified by a semi-empirical model.

7.6.1 Modeling the Effect of Yaw on Flow Control Efficiency

In this section a semi-empirical model, that describes the effect of yaw and how it affects flow control efficiency, will be discussed. The model is inspired by the work of Greenblatt & Washburn [GW08] and requires an estimation of the phase velocity U_Φ of the vortical structure that is generated by the LE actuator. The phase velocity at optimum forcing conditions was measured on a two dimensional flat plate wing with actuation along the leading edge and normal inflow (refer to chapter 8). It varies linearly between $U_\Phi/U_\infty = 0.58$ at the LE and 0.36 at the TE (figure 8.7, below). This data will be used in the following discussion because of a lack of appropriate data for the three dimensional wing.

At yawed inflow conditions one can define a tangential and a normal inflow velocity component according to equations (7.3) and (7.4):

$$U_{\infty,t} = U_\infty \sin(\beta) \tag{7.3}$$

$$U_{\infty,n} = U_\infty \cos(\beta) \tag{7.4}$$

For the following discussion it is assumed that:

- In yawed condition the vortical structures generated at the LE are convected tangentially with a velocity equal to $U_{\infty,t}$.
- The vortices are convected in the normal direction by $U_{\Phi,n}/U_{\infty,n} = \text{const} \neq f(\beta)$
- Vortex convection at the optimum forcing frequency is comparable to the two dimensional case.
- Only the perturbations that cover the full range from LE to TE are considered to have a positive effect on the lift.

Referring to Fig. 7.11 for the geometrical arrangement, and applying the above assumptions the trajectory angle ϵ can be calculated according to equation (7.5).

$$\epsilon = \arctan\left(\frac{U_{\Phi,n}}{U_{\infty,n}} \frac{1}{\tan(\beta)}\right) \tag{7.5}$$

The resulting trajectories for the three yaw angles are indicated in Fig. 7.11, and a summary of the percentages of unaffected areas are listed in table 7.2, together with the loss in ΔC_L, and changes in F^+_{opt}. The shaded red area in Fig. 7.11 represents the region which is not affected by the actuation effect at a yaw angle of $\beta = 30°$. Within this region the actuation does not have a positive effect on lift. Note that with increasing yaw angle this area increases in size (see table 7.2).

Note that the loss in ΔC_L is proportional to the size of the unaffected area of the wing. The small discrepancies are assumed to be due to three dimensional flow effects.

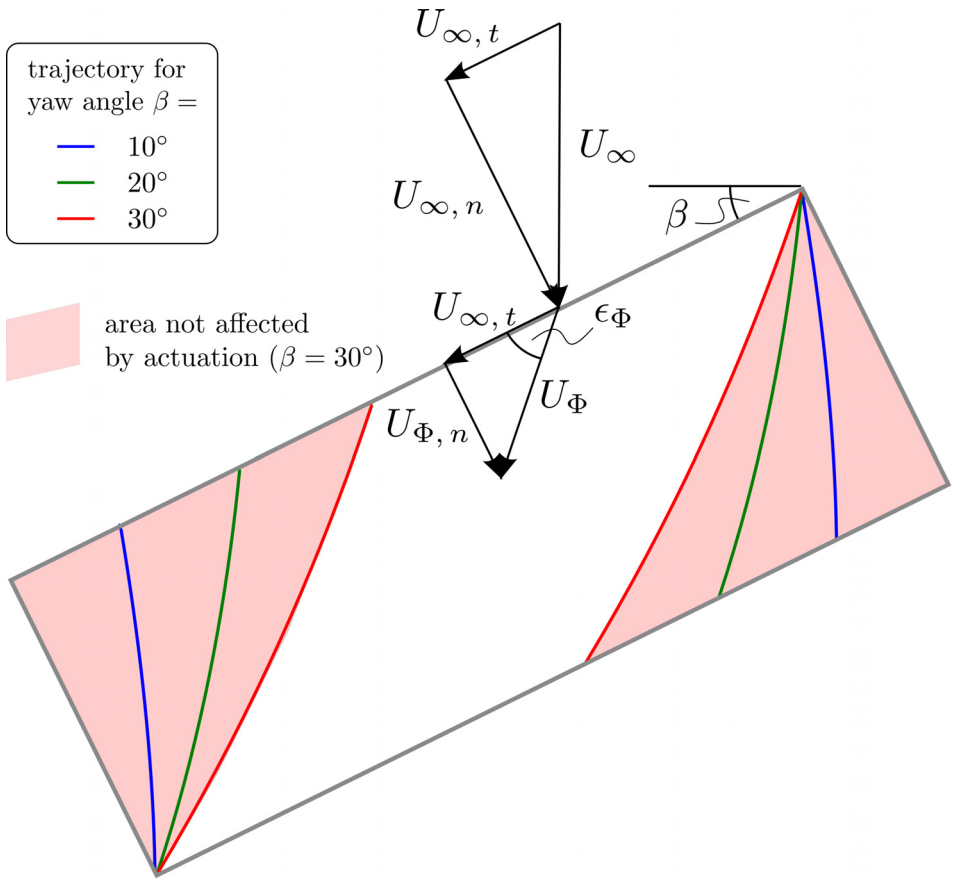

Fig. 7.11: Prediction of distortion trajectories based on a semi-empirical model. Geometrical relations of velocity vectors illustrated. Red area indicates the area that is not affected by LE control for $\beta = 30°$.

yaw angle β	unaffected area	loss in ΔC_L	F^+_{opt}
10°	14%	17%	0.23
20°	29%	34%	0.28
30°	46%	51%	0.35

Tab. 7.2: Effect of various yaw angles of rectangular planform wing on: area unaffected by LE control, loss in ΔC_L, and change in optimum forcing frequency.

This simple empirical model captures the effect of yaw to a reasonable degree and explains why flow control is less effective in these cases.

Applying this model to the semi-circular planform wing is somewhat more complicated. The flow field around this planform shape is inherently three dimensional and relations to an infinite wing can not be easily drawn in this case. A simpler approach was taken here in order to explain the behaviour of the semi-circular wing under yawed conditions. The area which is not affected by actuation is estimated as indicated by the shaded red region in Fig. 7.8, right. The fraction of unaffected area is simply calculated according to equation (7.6):

$$A_{\text{unaff.}} = \beta/180° \tag{7.6}$$

A look at table 7.3 reveals that the comparison of unaffected area $A_{\text{unaff.}}$ and loss in ΔC_L is not as promising as in the case of the rectangular planform shape. Nonetheless, the tendency is captured and it can be shown that the semi-circular planform shape is less sensitive to yaw effects.

yaw angle β	unaffected area	loss in ΔC_L	F^+_{opt}
10°	5.6%	7.1%	0.57
20°	11.1%	17.4%	0.62
30°	16.7%	21.2%	0.62

Tab. 7.3: Effect of various yaw angles of semi-circular planform wing on: area unaffected by LE control, loss in ΔC_L, and change in optimum forcing frequency.

7.7 Roll Control by DBD actuators

One of the prospected applications for DBD actuators, and AFC in general, is the replacement of hinged control surfaces on airborne vehicles. Given a sufficient control authority the actuators could replace classical ailerons or flaps. The resulting implementation would be lightweight, less complex, and without any moving parts.

The roll control authority of DBD actuators was investigated experimentally with LE and TE actuators on an AR 2 flat-plate wing at $U_\infty = 2.0\,\mathrm{m/s}$. With a chord-length of $c = 0.3\,\mathrm{m}$ the resulting Reynolds number was $\mathrm{Re} = 35\,000$. The wing was mounted on a support arm equipped with an active low friction bearing allowing the wing to roll freely. A picture of the wing mounted on the support arm is shown in Fig. 7.12. A video of the wing was taken with a camera mounted downstream of the wing inside the wind tunnel. The wings attitude was quantitatively measured by processing the video frames with a Python script. The resulting data is shown in Fig. 7.13 and will be discussed below. The roll control effect was realized

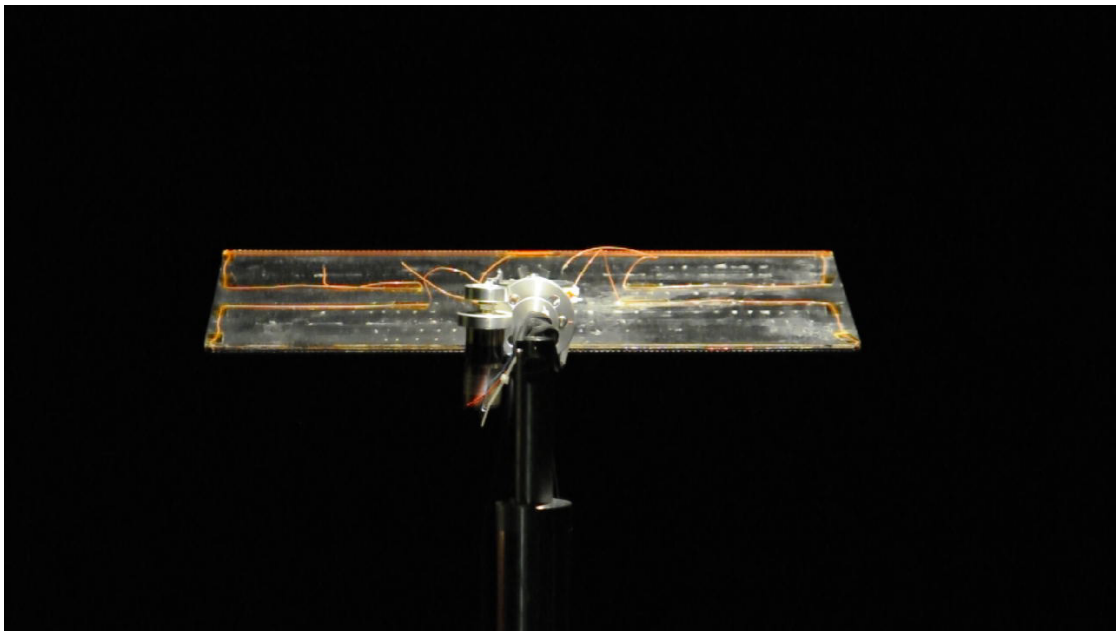

Fig. 7.12: AR 2 wing mounted inside 1.4 m × 2 m wind tunnel test section on support arm. View from downstream.

by applying individual DBD actuators to the left and the right wing-half, respec-

tively. The peak-to-peak voltage of each actuator was controlled by a PWM-based step-down converter. This enabled the control of the DC-supply voltage of the HV-generators through a square wave signal from a function generator. The actuators featured a zig-zag exposed electrode which increases the induced velocity (see chapter 4.3 for details).

At the start of each measurement sequence the actuators were operated at the same peak-to-peak voltage. Therefore the wing was initially at, or swinging around, the $\Phi = 0°$ roll angle (figure 7.13). Especially when the wing was set to a post-stall angle of attack ($\alpha = 28°$) periodic, large amplitude rolling motion of up to $\pm 8°$ was observed. This motion occurred at an approximate frequency of $f_{roll} \approx 0.17$Hz. A possible explanation is asymmetric flow separation from the wings left and right sides as observed by Taira & Colonius[TC09c], though no periodicity was found in their study. Additionally, for pulsed LE actuation, separation is triggered along the full length of the LE. This should eliminate any asymmetries in the flow separation process. Another possible explanation are low frequency distortions in the wind tunnel inflow.

Previous experiments revealed that pulsed LE forcing has the largest control effect in terms of lift increase. Looking at the results for LE control in Fig. 7.13 (red line) the following observations can be made:

- Initially the actuators operate at 50% power at a reduced frequency of $F^* = 0.12$. The wing performs a periodic low frequency rolling motion about $\Phi = 0°$.

- At $t = 57$s the right actuator is set to 100% while the left actuator is set to 0%. The wing performs a negative roll and oscillates about $\overline{\Phi} = -10°$ with exponentially decaying amplitude.

- At $t = 86$s the left actuator is set to 100% while the right actuator is set to 0%. The wing performs a positive roll and oscillates about $\overline{\Phi} = 15°$ with exponentially decaying amplitude.

- The transition time from $\overline{\Phi} = -10°$ to $\overline{\Phi} = 15°$ is $\Delta t = 2$s. The resulting roll-rate is therefore a mere $\Delta\Phi/\Delta t = 12.5°/$s – acrobatic airplanes have roll rates of $\approx 300°/$s

The disadvantage of roll control by pulsed LE actuation is (apart from the large oscillations) that a control effect can only be observed for post-stall angles of attack. In certain situations this might be sufficient, but generally a pre-stall control authority is anticipated and necessary. As discussed in chapter 7.3.1 the only actuator configuration that generated a pre-stall control effect was the TE actuator blowing in the upstream direction along the wings pressure side.
Roll control with TE actuators was tested at two angles of attack corresponding to a pre-stall ($\alpha = 10°$ and a post-stall ($\alpha = 28°$) case. In both cases the roll control effect was negligible (green and blue lines in Fig. 7.13). At post-stall angle of attack the low-frequency rolling motion is somewhat damped compared to the pulsed LE control case (compare green with red line). The amplitude is significantly reduced for the pre-stall angle of attack case (blue line).

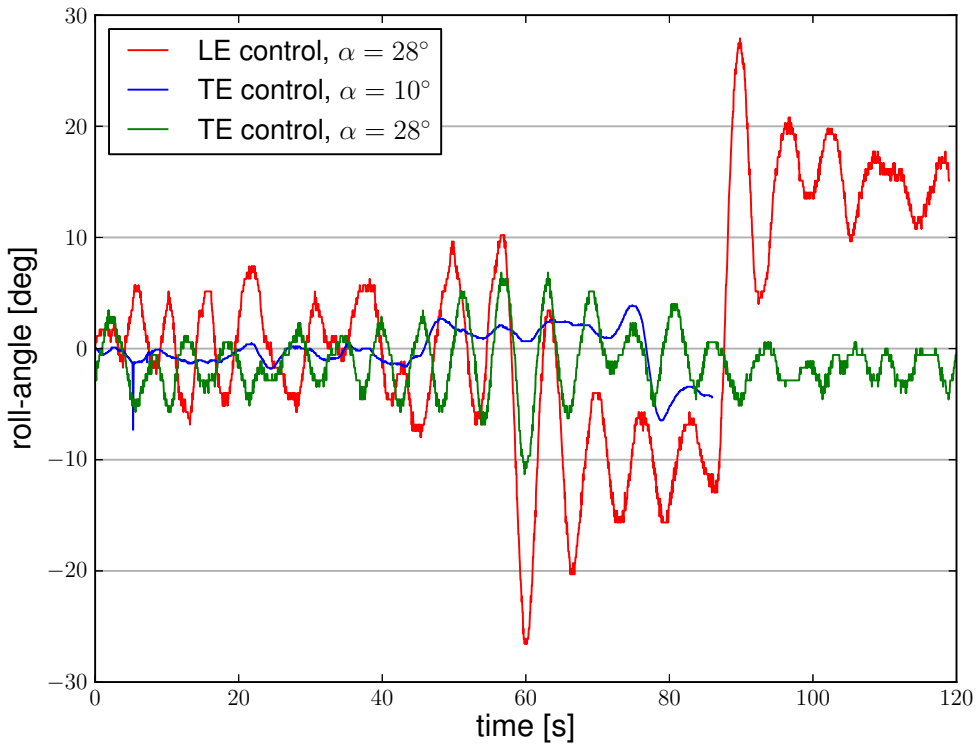

Fig. 7.13: Roll control by means of continuously upstream-blowing TE actuators or pulsed LE actuators operating at $F^*_{opt} = 0.12$. The finer angular resolution of the blue line is due to a different camera setup.

8. TIME RESOLVED PRESSURE MEASUREMENTS ON A TWO-DIMENSIONAL FLAT PLATE WING

8.1 Reasoning for 2D Wing Investigations

In order to investigate the vortex dynamics under the influence of LE control an experimental study was conducted on a 2-dimensional flat plate wing. This investigation was inspired by the numerical simulations conducted by Taira et al. [TRCW10], who studied flow control on low aspect ratio wings ($AR = 2$). They observed an optimum forcing frequency F^*_{opt} that was slightly lower than the natural shedding frequency of the wing, i.e. $F^*_{\text{opt}}/F^*_{\text{nat}} \approx 0.75$. At frequencies close to F^*_{opt} the standard deviation (std) of lift had a minimum. The authors reported a distinct natural shedding frequency of $F^*_{\text{nat}} = 0.12$. The 2.5D and 3D wings previously discussed in this study did not reveal a characteristic natural shedding frequency. It is assumed that the lower aspect ratio of the wings under investigation prevented a coherent natural shedding of vortices due to increased tip vortex effects. It was therefore decided to study natural vortex shedding and its relation to F^*_{opt} on a 2D wing configuration. Two-dimensional wings at post-stall angles of attack typically have distinct characteristic frequencies in the range $F^*_{\text{nat}} = 0.16...0.20$ (Taira & Colonius [TC09c]).

8.2 Experimental Setup for Time Resolved Pressure Measurements on 2D Wing with LE DBD

The experimental investigation was conducted in a blow-down type wind tunnel with a 0.28 m $\times$ 0.4 m test section of 1 m length. An end-diffusor consisting of a radial diffuser was attached to the downstream end of the test section in order to suppress tunnel oscillations. The flat plate wing with $t/c = 0.02$ was mounted from

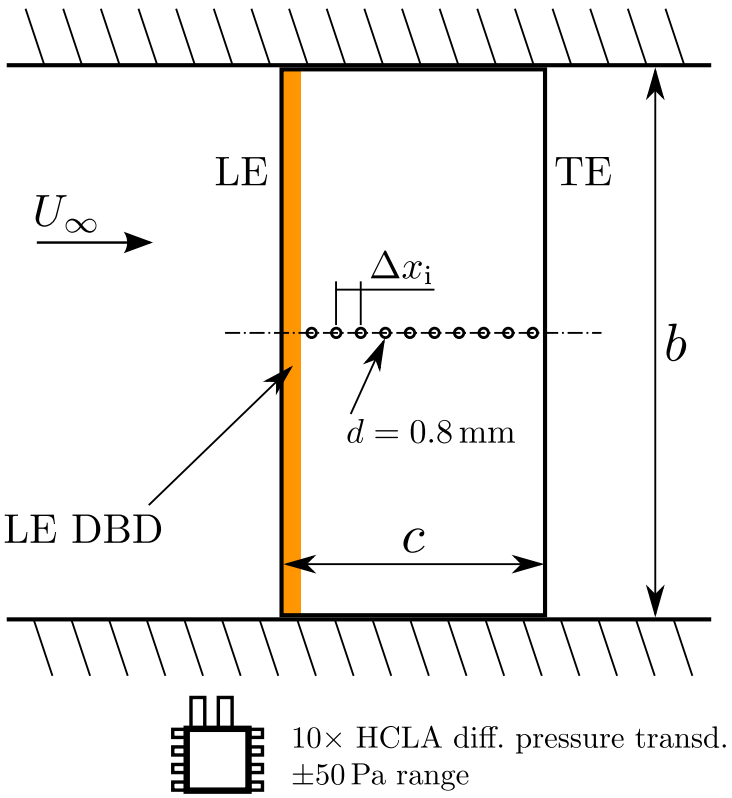

Fig. 8.1: Experimental setup for the measurement of time resolved surface pressures on a 2D flat plate wing with leading edge DBD at $\alpha = 28°$.

wall-to-wall and had a span of $b = 0.28\,\mathrm{m}$ and a chord length of $c = 0.1475\,\mathrm{m}$ (figure 8.1). The DBD actuator was located at the leading edge, blowing downstream along the wings upper surface. It was operated in burst mode with a duty cycle of $dc = 20\%$ at $V_{p2p} = 8\,\mathrm{kV}$ and $f_\mathrm{ion} = 8\,\mathrm{kHz}$. The active part of the actuator ended approximately 5 mm before the respective wall.

Ten pressure ports ($d_{pp} = 0.8\,\mathrm{mm}$) were incorporated into the suction side of the wing in a chord-wise row at mid-span. They were arranged between $x/c = 0.09$ and $x/c = 0.92$. The distances between two consecutive ports varied between $\Delta x = 6\,\mathrm{mm}...33\,\mathrm{mm}$. Ten amplified differential pressure transducers (*Sensortechnics* HCLA, ±50 Pa range) were connected to the pressure ports through 30 cm long flexible tubing with an inner diameter of $d_i = 1.2\,\mathrm{mm}$. The reference pressure was taken from the static pressure port of a Pitot-static probe.

It should be noted that the pressure measurement system was not calibrated for

amplitude respectively frequency attenuation through the connecting tubing. This was not deemed necessary for the expected frequency range of interest ($\mathcal{O}(1\,\mathrm{Hz})$ to $\mathcal{O}(10\,\mathrm{Hz})$).
Of higher importance is the fact that the blockage that was generated by the wing at $\alpha = 28°$ was quite considerable (solid blockage: 17%). The free-stream velocity was set with the wing at $\alpha = 28°$ to $U_\infty = 2\,\mathrm{m/s}$. Considering solid and wake blockage corrections this would result in an approximate free-stream velocity of $U_\infty = 3.3\mathrm{m/s}$ and accordingly shifted dimensionless frequencies. Nonetheless the correction was not performed for the data presented below, mainly because the interest is in the frequency *ratio* of optimum forcing and natural shedding – and not in the frequencies as such. Also for gaining a qualitative understanding for the forcing frequency dependent changes in mean value μ and standard deviation σ of the pressure signals the uncorrected velocity suffices.

For each forcing frequency the ten pressure ports, the Pitot-static probe signal and the forcing waveform were sampled at 5 kHz for 5 s. The respective forcing frequency was known for each case. In the unforced (e.g. baseline) case the natural shedding frequency was determined through a FFT. Mean phase velocity $\overline{u}_\Phi$ and growth of vortex intensity were determined through cross correlation of consecutive pressure port signals and the determination of the standard deviation, respectively. This defines the vortex dynamics, which were studied and compared for varying forcing frequencies $F^*_{\mathrm{sub}} < F^*_{\mathrm{opt}} < F^*_{\mathrm{sup}}$. On a global scale the optimum forcing frequency was determined by calculating the minimum overall mean pressure values. Additionally the overall (correlated) standard deviation σ_{corr} was calculated to define the *ride quality* of a vehicle operating with AFC devices. Its distribution was then compared to the numerical results obtained by Taira et al. [TRCW10].
Throughout the discussion the term F^* indicates a forced case while $\mathrm{St_D}$ indicates an unforced (i.e. baseline) case.

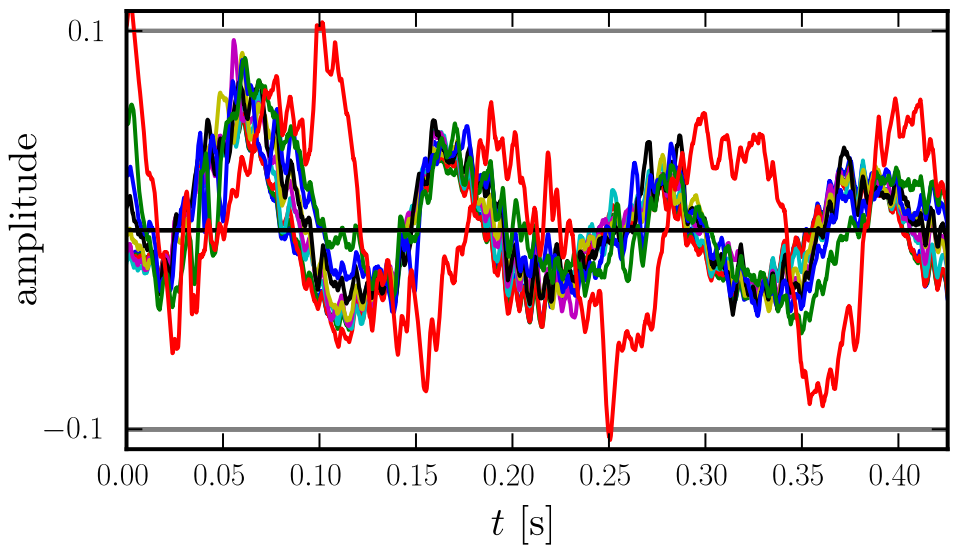

Fig. 8.2: Overlaid baseline pressure signals of the ten pressure ports. Note that the first mode is in phase.

8.3 The Unforced Case (Natural Shedding)

As mentioned above the natural shedding frequency $\mathrm{St_D}$ in the unforced case was determined by performing a FFT on the time series. For each of the ten pressure ports the frequency spectrum was similar and a distinct first mode at $f = 9.4\,\mathrm{Hz}$ ($\mathrm{St_D} = 0.325$, uncorrected) was identified. A representative frequency-spectrum of the unforced case is shown in Fig. 8.4 (top) for the pressure port closest to the leading edge. Note that the spectral peak at 33.4 Hz and its harmonic at 66.8 Hz are not harmonics of the first mode. The higher frequency peak at 171.0 Hz was interpreted as the Kelvin-Helmholtz shear layer shedding frequency. It can also be observed overlaid over the large scale sinusoidal signal in the temporal sequence shown in Fig. 8.5 (top) and in Fig. 8.2.

The temporal sequence of the ten pressure signals overlaid in Fig. 8.2 revealed that the initial sinusoidal vortex footprint (first mode) is neither amplified nor damped with downstream distance. Its standard deviation remains constant at $\sigma \approx 0.026$. The red line originates from the pressure port closest to the trailing edge and shows a somewhat different behavior, possibly caused by the pressure signature of a shedding trailing edge structure. It is remarkable that there is no temporal delay between the pressure signals in the unforced case. This can be observed

by inspection of Fig. 8.2 and was confirmed by cross-correlations performed on the signals (not shown here) and can be interpreted as an instantaneous, global separation phenomenon. Moreover it underlines the fact that separation does not occur in an organized manner of large coherent span-wise vortices that grow in size and are convected downstream. It is shown below that through actuation the shedding characteristics of the first mode were altered and occurred in a more organized manner, which resulted in a lift increase. The first mode could also be a trace of a von Kármán type wake instability, which affects the pressure field above the wing. This view is supported by the spatial distribution of coherent kinetic energy $\tilde{k}$ in a chord-wise measurement plane of the flow field around a low aspect ratio wing (see chapter 10.5 and Vey et al. [VNPG12]). In the baseline (uncontrolled) case increased values of $\tilde{k}$ were concentrated in a region downstream of the wings trailing edge in the vicinity of a detached stagnation point. It was concluded that this represents the interaction of LE and TE shear layers and the formation of large scale structures in the wings wake. The pressure signatures of these structures could be responsible for the shedding characteristics observed above. In the control case $\tilde{k}$ was concentrated immediately above the wing, which supports the observations discussed below for pressure signatures of the forced cases.

8.4 Global Effects of Actuation

To globally quantify the effect of actuation the mean pressure values μ of all pressure ports were integrated. Additionally a mean standard deviation σ was calculated by averaging over all the ports standard deviations. A large mean standard deviation thus corresponds to high overall amplitude fluctuations in the pressure signals, suggesting strong vortical structures (or a decrease in the distance of the vortices to the detecting pressure port, see for example Darabi & Wygnanski [DW04]).

The frequency scan procedure was similar to the approach described in the section on the force measurements on flow control on the 2.5D and 3D wings. Refer to section 6.3 for details.

The mean pressures variation over forcing frequency is depicted in Fig. 8.3

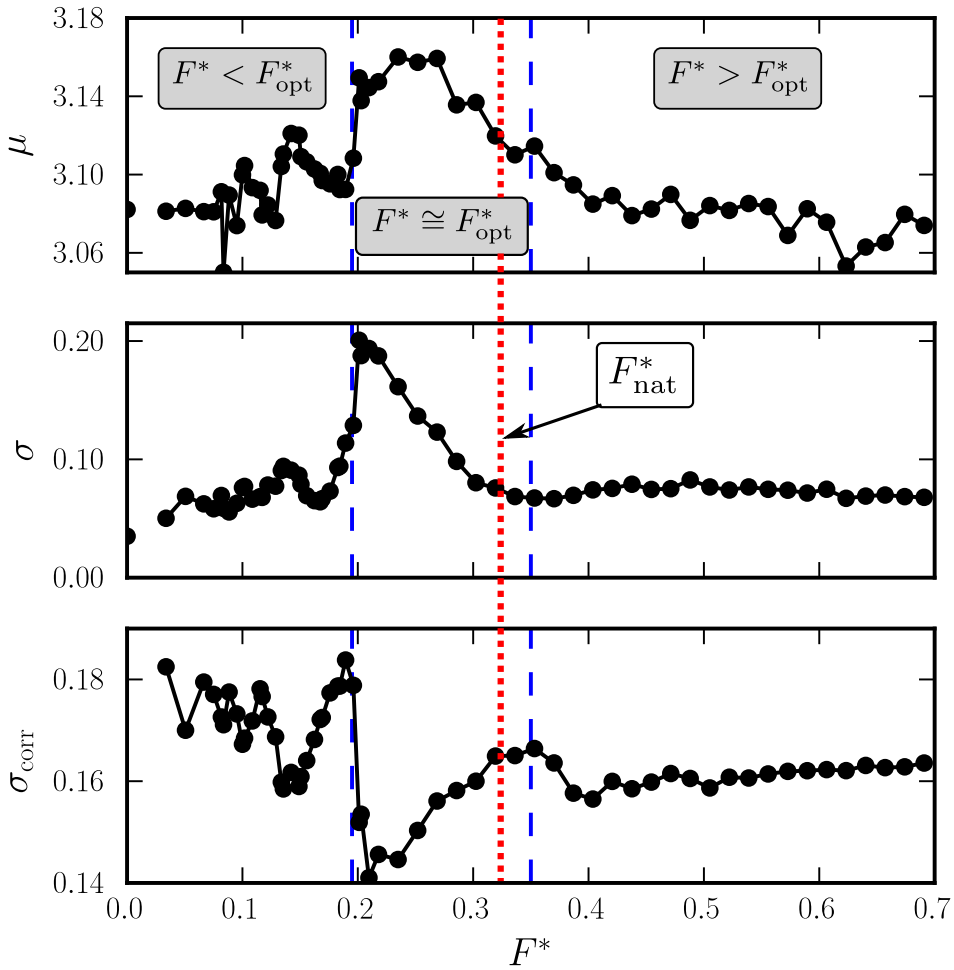

Fig. 8.3: The effect of forcing at the leading edge of a 2D wing as seen in the mean surface pressures μ and the corresponding mean standard deviation σ and correlated standard deviation σ_{corr}. Natural shedding frequency at $F^*_{nat} = 0.325$.

(top). A region of increased mean values is observed between approximately $0.19 < F^* < 0.35$. The unforced case corresponding to $\mathrm{St_D} = 0.325$ is marked by the isolated black disk symbol at $F^* = 0$. The forcing frequency F^* that matches the natural shedding frequency $\mathrm{St_D}$ was termed F^*_{nat} and is marked by the dotted red line in Fig. 8.3. It is interesting to note that F^*_{nat} lies within the range of optimum forcing frequencies as defined above. In both cases the flow should be dominated by the same principal frequency, yet a higher lift coefficient is obtained in the forced case.

Some light is shed into this situation by inspection of the Fourier spectrum shown in Fig. 8.4 for the unforced case (top) and the F^*_{nat} case (middle). Generally the energy content is higher in the forced case for the spectral range shown here. The forced case spectrum is dominated by the peak at the forcing frequency and the corresponding harmonics. The spectral peak at 33.4 Hz and its harmonic at 66.8 Hz is suppressed, but the shear layer shedding frequency is retained though at a slightly lower frequency of 170.0 Hz. This reduction is most likely due to the effect of forcing on the time-mean flow field (i.e. changes in mean velocity and pressure gradient).

When the flow is forced at the optimum forcing frequency $F^*_{\mathrm{opt}} = 0.209$ the spectrum does not materially change compared to the F^*_{nat} case. Energy content is shifted towards the lower end of the spectrum and the shear layer shedding frequency is further reduced to 169.6 Hz. This results in a further increase in lift compared to the F^*_{nat} case. How exactly F^*_{opt} was determined here will be discussed below.

Coming back to the pressure signal time series shown in Fig. 8.5 an increase in signal amplitude can be observed from the top (unforced) via the middle (F^*_{nat}) to the bottom (F^*_{opt}) of the Fig. (note the varying axis scaling). In all three series the shear layer shedding frequency discussed above can be observed. In the forced cases (middle & bottom) traces of the actuation deform the signal from its otherwise sinusoidal shape.

The variation of the pressure signal standard deviation with chord-wise location was further investigated and is shown in Fig. 8.6. Several data series of varying forcing frequencies were grouped according to the three frequency regimes as marked in Fig. 8.3. The specific characteristics of each group are:

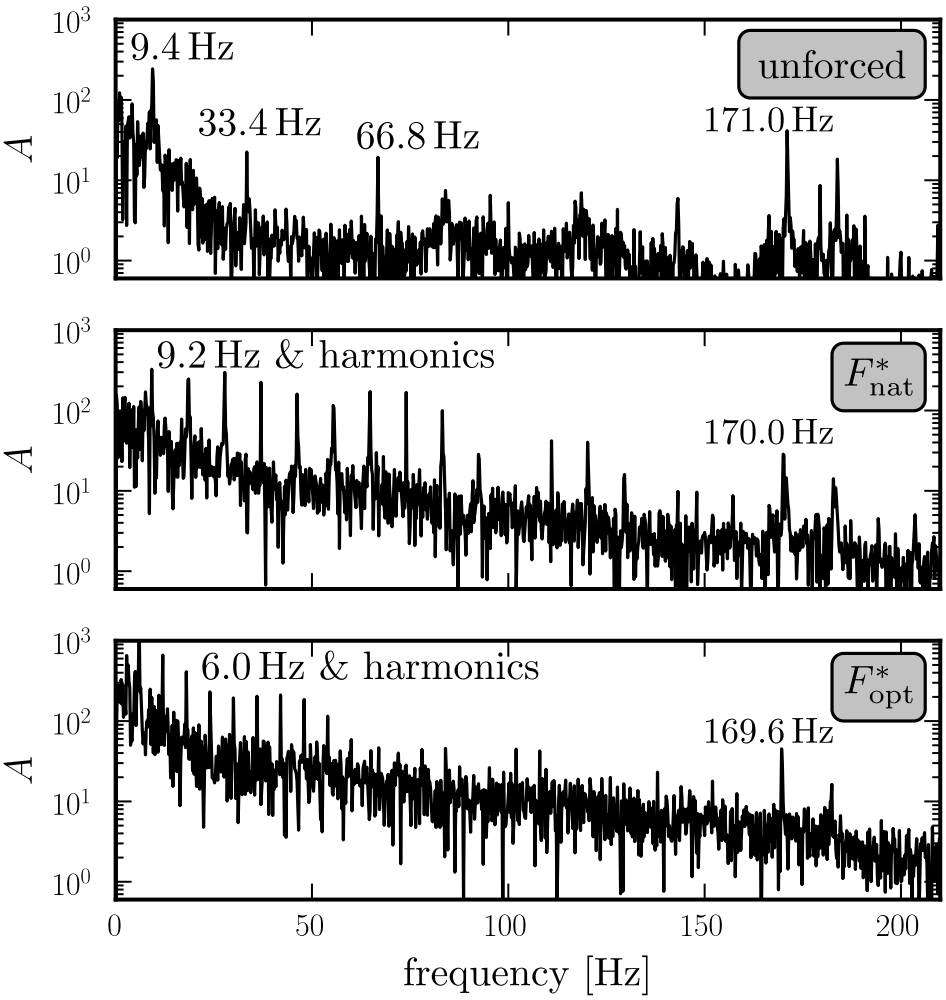

Fig. 8.4: FFT of three time series representing, from top to bottom: the unforced (baseline), F^*_{nat}, and F^*_{opt} cases.

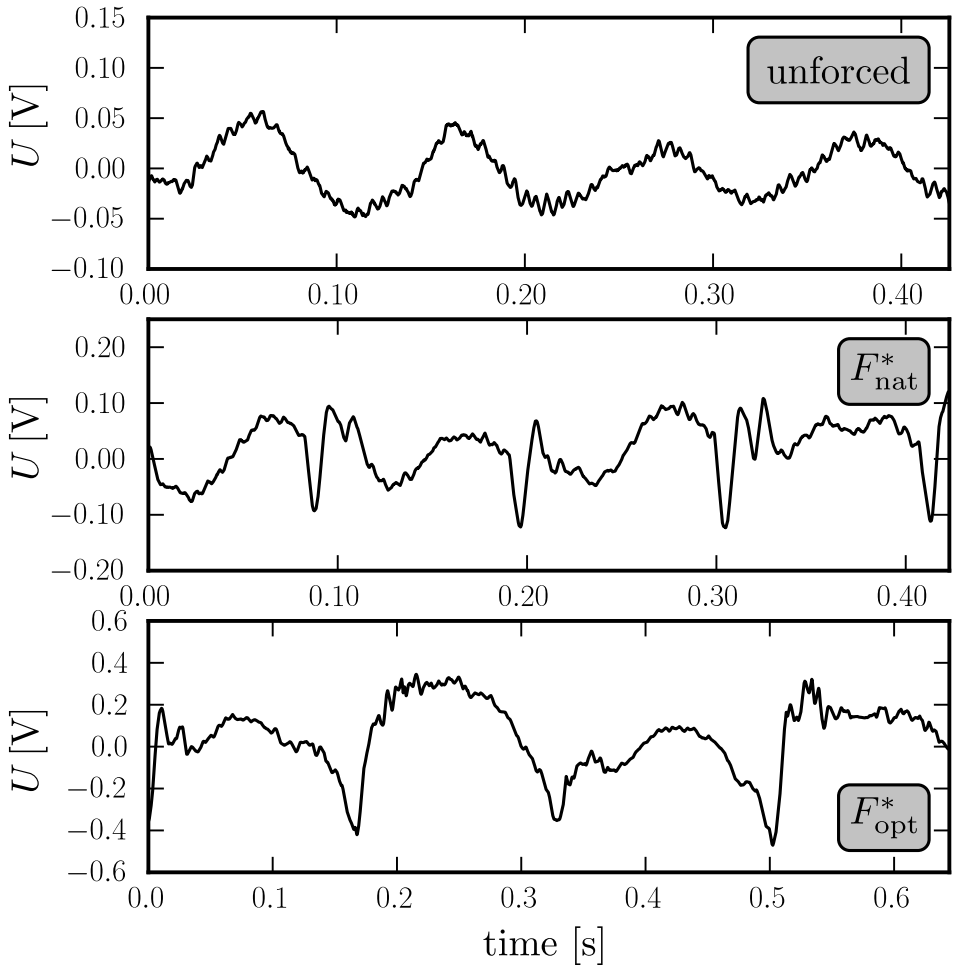

Fig. 8.5: Surface pressure time series at pressure-port closest to the leading edge. Same cases as in Fig. 8.4. Note change in axis scaling.

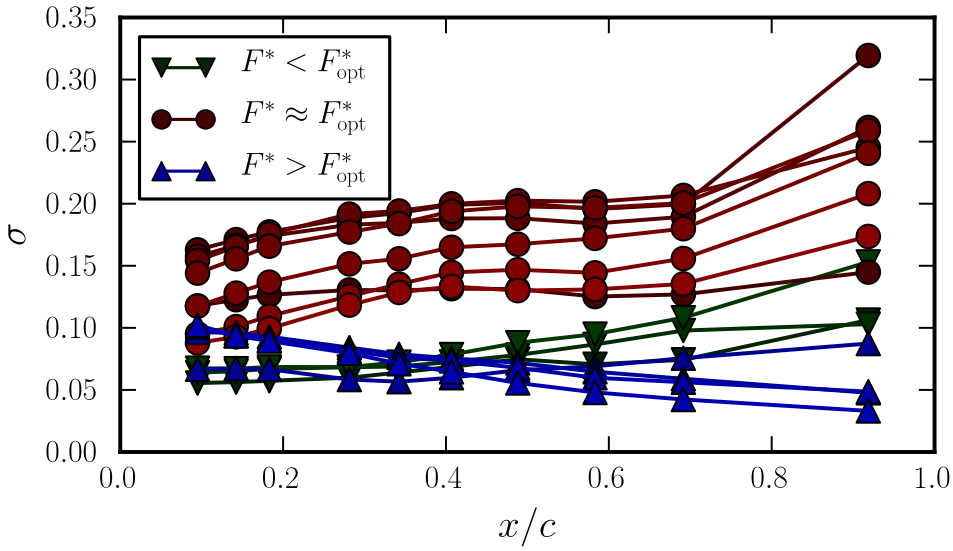

Fig. 8.6: Vortex footprint strength determined by surface pressure measurements over chord-wise location. Note characteristic vortex development for the three frequency regimes corresponding to Fig. 8.3

$\mathbf{F}^* < \mathbf{F}^*_{\text{opt}}$*:* increasing pressure fluctuations with chord-wise distance

$\mathbf{F}^* \cong \mathbf{F}^*_{\text{opt}}$*:* highest overall pressure fluctuations, increasing with chord-wise distance

$\mathbf{F}^* > \mathbf{F}^*_{\text{opt}}$*:* pressure fluctuations decreasing with chord-wise distance

The mean phase velocities $\overline{U}_\Phi$ (=convection velocity) for the last two groups were calculated by means of a cross-correlation between consecutive pressure port signals (figure 8.7). The location where $\overline{U}_\Phi$ is measured was assumed to be centered between the corresponding pressure ports, i.e. $x_i + 1/2\,\Delta x_i$. As mentioned above $\overline{U}_\Phi$ for the unforced case is zero, suggesting an instantaneous and global separation phenomenon. A nonzero phase velocity is indicative for the shedding of span-wise vortices. These vortices are convected downstream and grow or diminish in strength as shown above in Fig. 8.6. When forced at F^*_{opt} the phase velocity was essentially constant over x/c at $\overline{U}_\Phi \approx 1.7\,\text{m/s}$ with a marginal reduction towards the trailing edge region. In contrast $\overline{U}_\Phi$ for higher forcing frequencies increases by a factor of two with downstream distance.

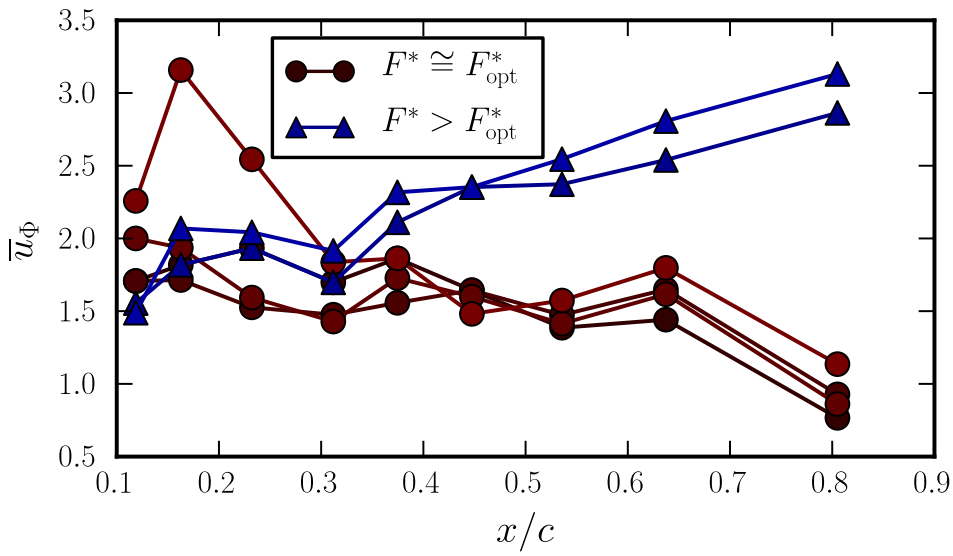

Fig. 8.7: Mean phase velocity $\overline{u}_\Phi$ of passing vortices.

One of the conclusions from the above discussion is that around F^*_{opt} lift reaches a maximum, while the mean standard deviation of the pressure signals also reaches a maximum, which is concentrated at $F^* = 0.208$. Large periodic pressure fluctuations would result in a large force variation, which is detrimental for the ride quality. A different conclusion can be drawn when first averaging the pressure fluctuations at each time step and then taking the standard deviation, which was termed the correlated standard deviations σ_{corr}. Its distribution is plotted in Fig. 8.3 at the bottom. Notably σ_{corr} has a clearly defined minimum at F^*_{opt}, which is interesting because the overall fluctuations σ reach a maximum. A similar behavior was also observed in the numerical simulations by Taira et al. [TRCW10], who found that the overall lift fluctuations on a low aspect ratio wing with flow control reached a minimum at F^*_{opt}. Though the authors did not give an explanation why a minimum was reached.

8.5 Vortex Phase Lag at Optimum Forcing Frequencies

Some light is shed into this question by considering the temporal arrangement of the vortices given by the phase lag according to (8.1).

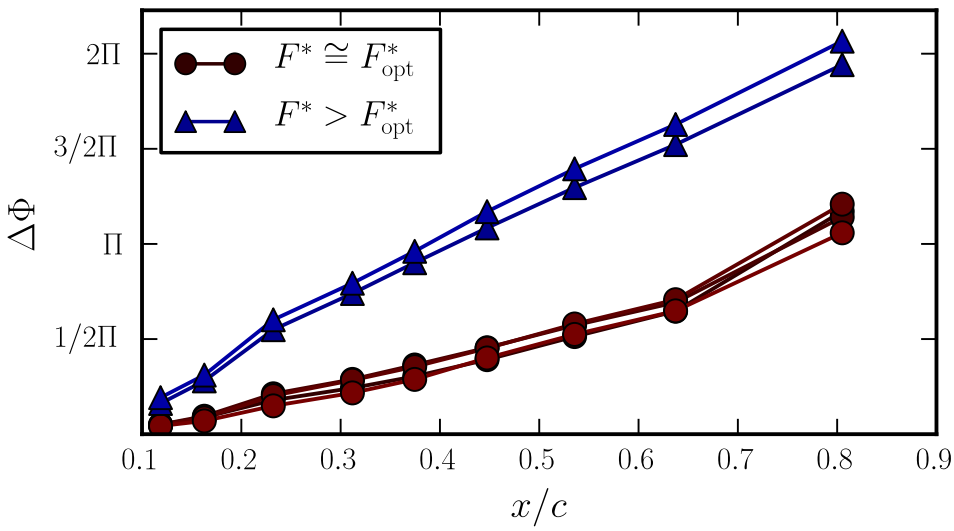

Fig. 8.8: Phase delay $\Delta\Phi$ of vortices for varying actuation frequencies. Note that for near-optimum frequencies ($F^* = 0.203...0.235$) the phase lag between LE and TE is approximately π.

$$\Delta\Phi = \frac{\Delta t}{T}\, 2\pi \tag{8.1}$$

With the total time lag Δt and the forcing period T. Where T is given by (8.2) in terms of the governing forcing parameters.

$$T = \frac{1}{f} = \frac{c\,\sin(\alpha)}{F^*\,U_\infty} \tag{8.2}$$

And Δt is given by (8.3).

$$\Delta t = \text{cumsum}\left(\frac{\Delta x_i}{\overline{U_\Phi}}\right) \tag{8.3}$$

The results shown in Fig. 8.8 reveal significant differences in the phase delay at F^*_{opt} as compared with non-optimum forcing conditions. The phase delay between the two outermost chord-wise measurement positions is approximately half a phase, e.g. $\Delta\Phi = \pi$, at F^*_{opt}, suggesting that the periodic pressure fluctuations on the wing neutralize, at least to some extend. With this in mind the minimum in the correlated standard deviation at F^*_{opt}, that was mentioned above in conjunction with Fig. 8.3 can be explained.

9. THE LEADING EDGE SHEAR LAYER AT HIGH ANGLES OF ATTACK

Based on intuition the optimum actuation frequency was initially expected to be in the range of the Kelvin-Helmholtz instability frequency of the shear layer emanating from the wings leading edge. This was further backed by the fact that forcing the flow directly at the leading edge (from where the shear layer originates) resulted in the largest levels of lift increase. This suggests that the leading edge shear layer is somehow involved in the fluid mechanical process which ultimately results in an lift increase.
It was therefore decided to study this shear layer in some more detail by evaluating the available PIV datasets of the baseline and the control case. The approach that was taken here was to determine the shear layer thickness, spreading, and characteristic velocity in order to estimate it characteristic frequency, which is then compared to the optimum actuation frequency. Furthermore the changes of the shear layer parameters with regard to the forcing are discussed.

Following common practice a hyperbolic tangent velocity profile was fitted to the measured velocity distributions (equation (9.1), with the fitting parameters P_0 and P_1).

$$U_{fit}(y) = \tanh\left(\frac{y - P_0}{P_1}\right) \tag{9.1}$$

The quality of the fitting can be judged by referring to figures 9.1 and 9.2 which show the measured profiles (dashed red lines) and the fitted profiles (solid black lines). Note that the extreme velocities ($U_{\min}$ and $U_{\max}$) are defined by the velocity overshoots. A qualitative comparison of the shear layer development under the influence of actuation reveals a generally thicker shear layer in the control case. Furthermore with actuation it is deflected more towards the wings upper surface.

This will be discussed in more detail in chapter 10.3.

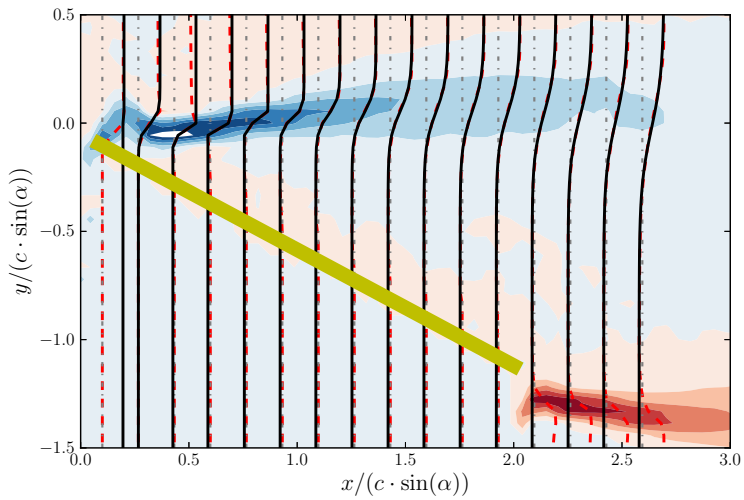

Fig. 9.1: Shear layer above wing for the baseline case. Velocity profile fit (solid black line) compared to measurement (dashed red line). Contours showing qualitative vorticity distribution.

A quantitative comparison of the shear layer development is shown in Fig. 9.3 where the local momentum thickness Θ is plotted according to equation (9.2). Note that Θ was non-dimensionalized here with $c\ \sin(\alpha)$.

$$\Theta = \int_{-\infty}^{\infty} \frac{U(y) - U_{min}}{U_{max} - U_{min}} \cdot \left(1 - \frac{U(y) - U_{min}}{U_{max} - U_{min}}\right) \mathrm{d}y) \tag{9.2}$$

An approximately linear growth of the unforced mixing layer was observed. The forced mixing layer is thicker and initially features an increased growth rate. At approximately $x/(c \cdot \sin(\alpha)) = 1.2$ the growth rate is reduced to a value less than that of the baseline case and further growth is non-linear.

Following the lines of Fiedler & Fernholz [FF90] the shear layer data is now generalized using the Abramovich-Sabin rule by introducing the velocity

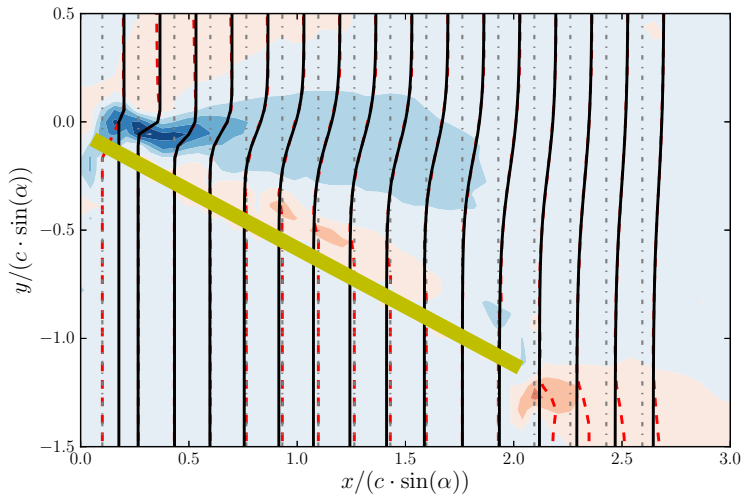

Fig. 9.2: Shear layer above wing with LE control at $F^* = 0.12$. Velocity profile fit (solid black line) compared to measurement (dashed red line). Contours showing qualitative vorticity distribution.

parameter according to equation (9.3):

$$\lambda = \frac{U_{max} - U_{min}}{U_{max} + U_{min}} = \frac{\Delta U}{\Sigma U} \tag{9.3}$$

For a classical mixing layer $\Theta/(\lambda \cdot x) \approx 0.032$ is found [FF90]. This relation is plotted in Fig. 9.4 for the unforced and the forced mixing layer. Starting from $x/(c \cdot \sin(\alpha)) \approx 1.3$ the baseline mixing layer approaches a constant value of $\Theta/(\lambda \cdot x) = 0.037$. The non linear development up to $x/(c \cdot \sin(\alpha)) \approx 1.3$ is attributed to the effect that the vicinity of the wings upper surface has on the initial development of the mixing layer.

The characteristic frequency of a mixing layer f_c is then calculated according to equation (9.4) (see [FF90]) and plotted in Fig. 9.5.

$$f_c \propto \frac{U_{max} + U_{min}}{\Theta} \tag{9.4}$$

Both mixing layers asymptotically reach a value of $f_c = 210\,\mathrm{Hz}$. A variation of the

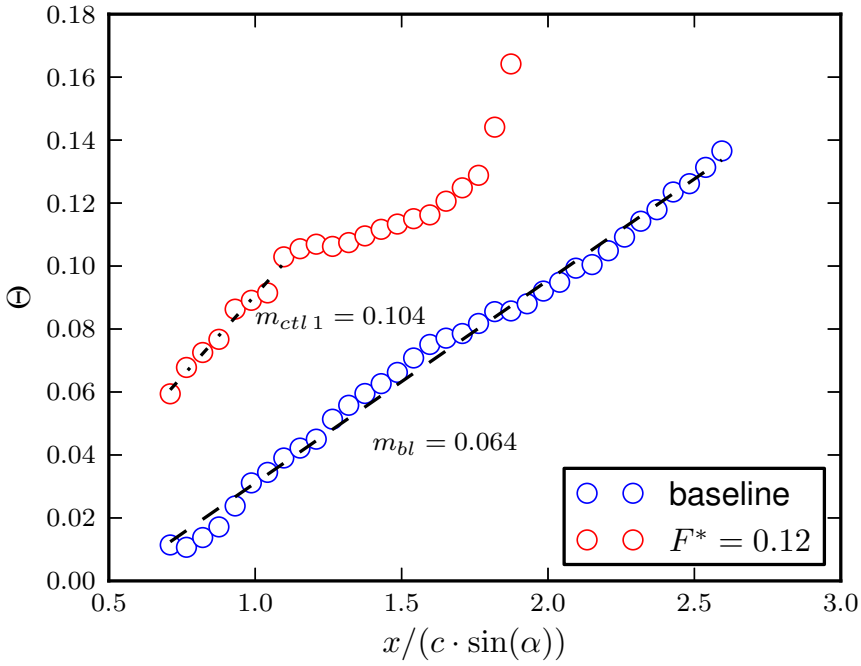

Fig. 9.3: Comparison of shear layer spreading for baseline and control case. Note that Θ is non-dimensionalized by dividing by $c\,\sin(\alpha)$.

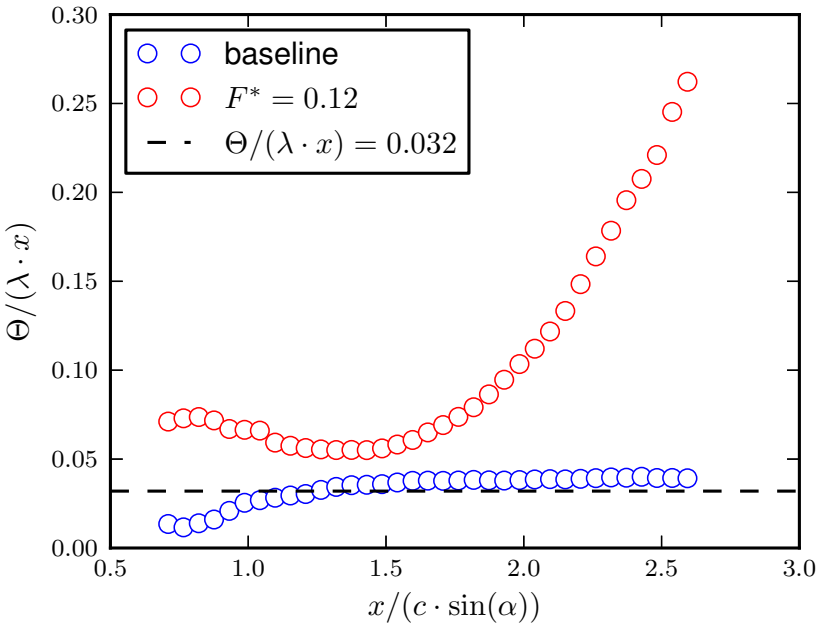

Fig. 9.4: Relation between local shear layer width Θ and downstream distance x for baseline and control case. In the general case $\Theta/(\lambda \cdot x) \approx 0.032$ [FF90]. Note that both Θ and x are non-dimensionalized by $1/(c\ \sin(\alpha)$.

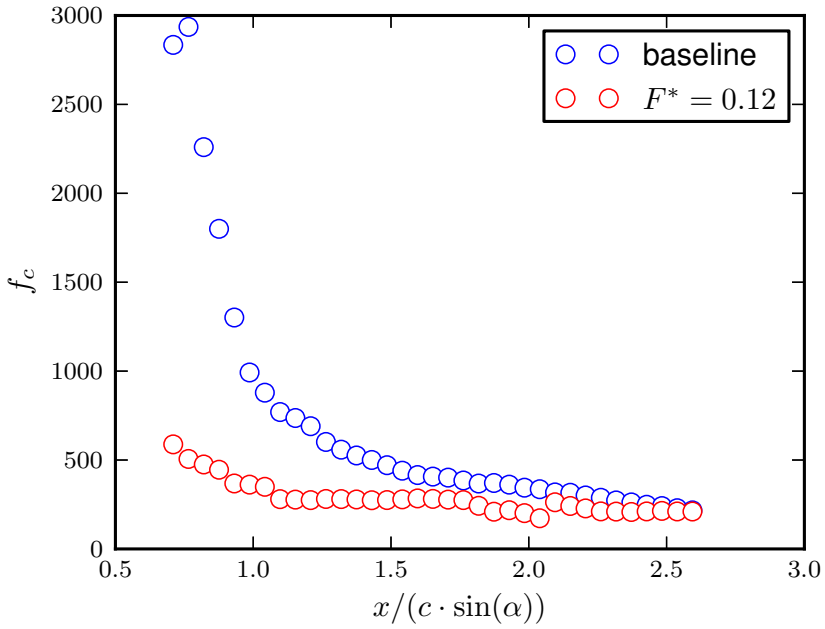

Fig. 9.5: Variation of the characteristic frequency of the two mixing layers $f_c = (U_{max} + U_{min})/\Theta$ with downstream distance.

characteristic frequency over one order of magnitude was observed for the baseline case, while in the control case only a small frequency variation was observed. The characteristic frequencies of the respective shear layers are approximately two orders of magnitude higher than the optimum forcing frequency. It is therefore concluded that the lift-enhancing mechanism in this case is not related to the exploitation of a shear layer instability.

10. FLOW FIELD CHARACTERIZATION

A detailed stereo-PIV study was performed on the 3D wings with the aim of gaining insight into the underlying fluid mechanics and dynamics of the flow control method. Before the discussion of the experimental results a separation classification scheme is described. The baseline and control flow fields are then categorized according to the classification scheme. The effect of pulsed actuation at different modulation frequencies on the flow field is discussed and the flow field dynamics are investigated through a proper orthogonal decomposition. A decomposition of the flow field variables into a mean, a coherent, and an incoherent component was performed and their respective distributions are discussed.

10.1 Experimental Setup for the Stereo PIV Study

The wings were mounted in the same manner as described in chapter 7 (see Fig. 7.1) into the 1.4 m $\times$ 2.0 , m test section of the TU Berlin large wind tunnel (GroWiKa). The PIV system consisted of a high energy Nd:YAG dual laser manufactured by *BigSky* with an energy of 160 mJ per pulse at a wavelength of 532 nm. The laser beam was guided to the test-section by a light-arm which also incorporated the light-sheet optics. Two CCD-cameras with accompanying Scheimpflug-adapters and a resolution of 2048 $\times$ 2048 pixels were used for taking the PIV snapshots of which a total of 942 were captured for each configuration. A 50 mm Canon lens was used on the cameras. The measurement-plane was located at the $y/b_s = 0.5$ position (for the $AR = 2.66$ wing). By adjusting the height of the support arm it was also possible to measure at other span-wise positions. In order to avoid direct reflections from the wing the surface was covered by a fluorescent foil. Bandpass-filters were installed to the cameras which let the 532 nm laser-light pass and blocked the scattered and ambient light. Additionally the light sheet

was aligned tangentially with the wings suction side surface, further resulting in reduced reflections and scatter.

10.2 Separation Classification Scheme

Prior to the discussion of the experimental data a classification scheme for separated flows is introduced. This scheme was adopted from LEDER [Led92], who defined three classes of separated flows, of which only the first two classes (A and B) are relevant for the cases discussed here. The geometric arrangement of the shear layers and the magnitude of the coherent Reynolds stresses are the main characterizing features of the flow. Depicted in Fig. 10.1 are the flow field classes reproduced from LEDER [Led92]. A class A separation is characterized by a one-

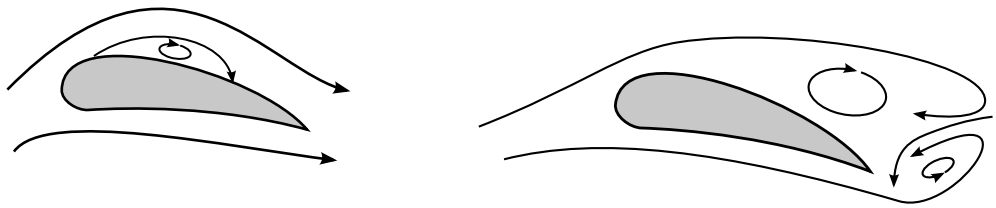

(a) class A: one-sided shear layer, $\alpha < \alpha_{stall}$ *(b)* class B: two-sided shear layer, $\alpha > \alpha_{stall}$

Fig. 10.1: Classification scheme for separated flows on airfoils. Reproduced from LEDER [Led92], p. 44.

sided shear layer which is bounded by a solid wall, for example the surface of a wing (figure 10.1(a)). The flow separates in the leading edge region and reattaches further downstream forming a closed separation bubble. This flow configuration is observed on wings at pre-stall angles of attack, where the flow would undergo a laminar separation, a transition to turbulence, and subsequent turbulent reattachment.

A two-sided shear layer is characteristic for a class B separation (figure 10.1(b)). This flow configuration occurs on wings at post-stall angles of attack where shear layers emanate from the leading and the trailing edge, respectively. These shear layers then interact downstream of the body resulting in a clearly defined shedding frequency and an increase in the Reynolds stress terms by an order of magnitude

compared to a class A separation (Leder [Led92]). Furthermore a detached stagnation point in the time-mean flow field develops downstream of the wing.
This scheme was defined for natural, i.e. uncontrolled flow configurations. In this case the reattachment length of a class B separation is shorter than for a class A separation. The increased Reynolds stress terms result in an enhanced momentum exchange, which reduces the reattachment length. The differences to controlled flow fields will be discussed in the following.

10.3 Qualitative Comparison of Baseline and Control Flow Fields

A qualitative comparison of the two extreme cases, i.e. baseline and control at $F^*_{\text{opt}} = 0.12$, is shown in Fig. 10.2. The wing was an $AR = 2.66$ rectangular planform with a chord length of $c = 0.15\,\text{m}$ operated at $\alpha = 28°$ and $\text{Re} = 18\,000$. The mean in-plane flow field was visualized by a line integral convolution (lic) according to the method described by Cabral & Leedom [CL93]. Additionally the shear layers are emphasized by the in-plane vorticity shown in red (negative) and blue (positive) shades. Comparing the flow field structure in figures 10.2(a) and (b) with the classification scheme introduced above in figures 10.1(a) and (b) the baseline flow field is identified as a class B separation with two shear layers emanating from the LE and the TE, respectively, and a detached stagnation point (white circle). On the other hand the control flow field resembles similarities to a class A separation with its single-sided shear layer, the closed separation bubble, and subsequent reattachment at $x/c \approx 0.83$. Due to the reattachment the velocity-difference between the flow from the upper surface and the lower surface in the trailing edge region is small and therefore the shear layer is not as pronounced as in the baseline case. In the control case the flow also separates from the leading edge. The fluid above the wing now recirculates at a higher velocity and consequently the pressure in this region is reduced. This causes a curving of the leading edge shear layer towards the wing resulting in increased circulation and therefore higher lift coefficients. It is therefore in line with the force measurements that were discussed in chapter 7.

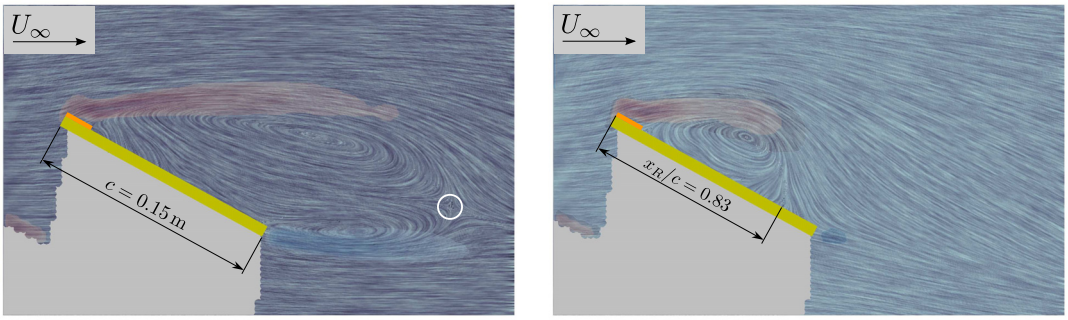

(a) baseline (class B) *(b)* LE control at $F^* = 0.12$ (class A)

Fig. 10.2: Flow-field around $AR = 2.66$ rectangular planform wing visualized using line integral convolution (lic). PIV measurement plane at $y/b_s = 0.5$. Re = 18 000, $\alpha = 28°$.

10.4 Time Mean Flow Field at Varying Actuation Frequencies

To gain insight into the flow field structure at varying actuation frequencies the effect of varying values of F^+ on the flow field structure was studied in more detail. Visualized by the normalized vorticity distribution and the in-plane vector-field in figures 10.3(a)–(g) is the changing of the flow field as the actuation frequency is increased from $F^+ = 0$ (baseline, (a)) via the optimum reduced forcing frequency $F^+_{\mathrm{opt}} = 0.257$ (c) to the highest frequency of $F^+ = 1.0$ (g). Within this sequence Fig. 10.3a and 10.3c correspond to the lic visualization in Fig. 10.2a and 10.2b, respectively. Concentrating on the shear layers it is obvious that the baseline vorticity distribution has the furthest (a) and the control case with $F^+ = F^+_{\mathrm{opt}}$ (c) has the shortest downstream extent. This holds true for both the leading edge and the trailing edge shear layers. For $F^+ > F^+_{\mathrm{opt}}$ the trailing edge shear layers vorticity increases which is due to an increased velocity difference between pressure and suction side flow, caused by a downstream movement of the reattachment location on the pressure side. This is accompanied by a reduced vorticity and an increased distance from the wings surface of the leading edge shear layer. Of note is also the decrease in LE shear layer width as the forcing frequency is increased.

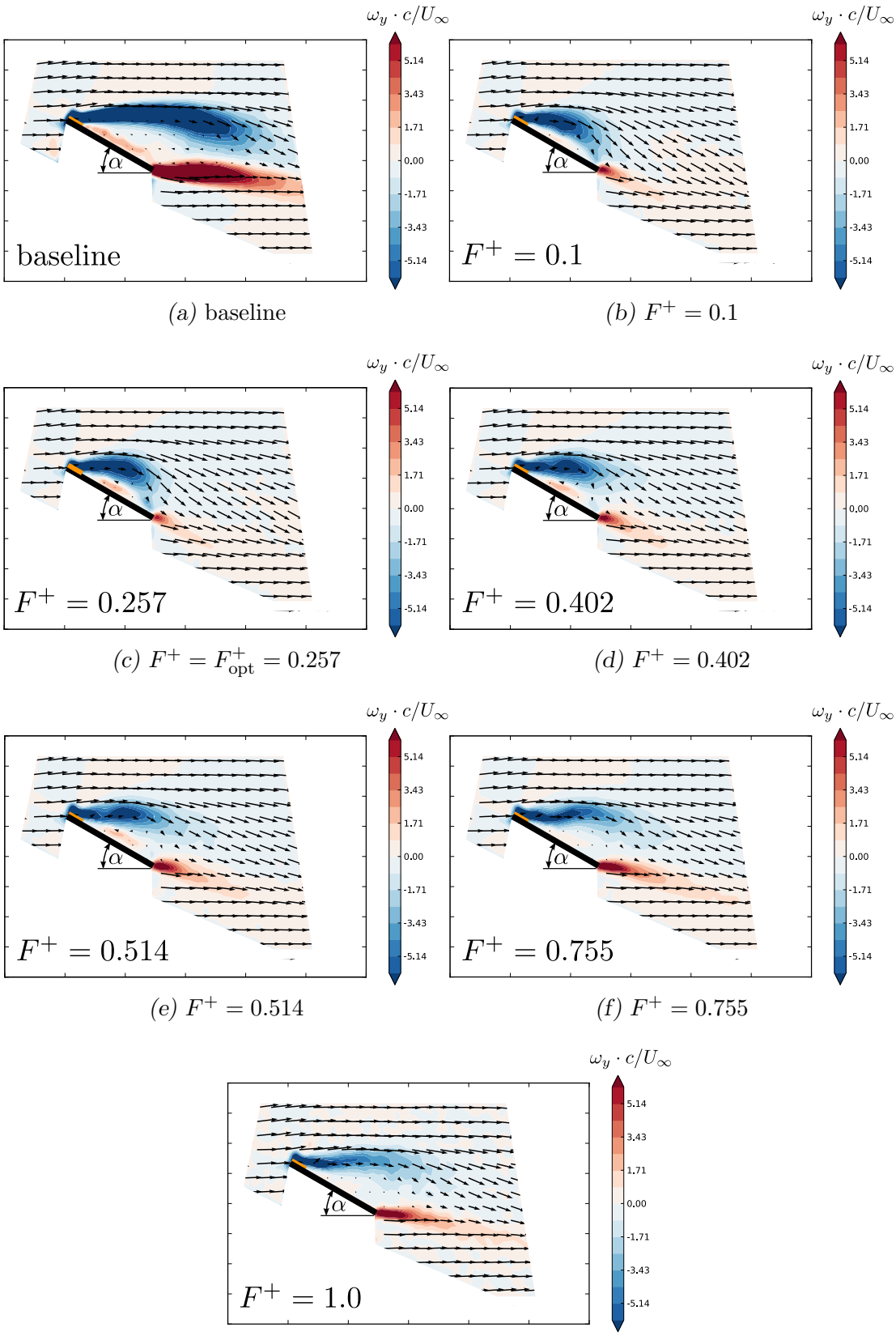

(a) baseline *(b)* $F^+ = 0.1$

(c) $F^+ = F^+_{\text{opt}} = 0.257$ *(d)* $F^+ = 0.402$

(e) $F^+ = 0.514$ *(f)* $F^+ = 0.755$

(g) $F^+ = 1.0$

Fig. 10.3: Flow-field for varying forcing frequencies. AR = 2.66 rectangular planform wing at $\alpha = 28°$, Re = 18 000 with LE actuator.

10.5 Flow Field Decomposition

10.5.1 Background

The introduction of periodic forcing onto the flow field triggers the generation of large coherent structures HUSSAIN [Hus83]. A leading edge actuator would for example initiate the roll-up of span-wise structures. In the case of flow control on wings these structures enhance the mixing between the stagnant fluid immediately above the wing and the more energetic free-stream. In the experimental study of DARABI & WYGNANSKI [DW04] the authors found that consecutive span-wise vortices act as a *vortex pump*, which drives the impulse transport across the shear layer above the wing.

CANTWELL & COLES [CC83] experimentally investigated the flow dynamics in the turbulent cylinder wake and decomposed the Reynolds stresses into a periodic component and a random component.

This decomposition was applied here to the PIV data of the span-wise measurement planes on 3D wings with leading edge control. It was expected that a change in flow control efficiency will be reflected in the topology of the distribution of the Reynolds stresses, especially in the periodic contribution to the Reynolds stress term.

In order to gain insight into the lift-enhancing mechanism of leading edge control and the underlying vortex dynamics the coherent component of the velocity field needs to be investigated. Any instantaneous flow field variable $s(\vec{x},t)$ can be decomposed into a time-mean $\overline{s}(\vec{x})$, a coherent $\tilde{s}(\vec{x},t)$, and an incoherent $s'(\vec{x},t)$ component. This is termed the *triple decomposition*, which is frequently used in the analysis of periodic flow phenomena, REYNOLDS & HUSSAIN [RH72], TELIONIS [Tel81], HUSSAIN [Hus83], LEDER [Led92]:

$$s(\vec{x},t) = \overline{s}(\vec{x}) + \tilde{s}(\vec{x},t) + s'(\vec{x},t) \tag{10.1}$$

The fluctuating components consist of the coherent and the incoherent (i.e. random) velocity. These can be summarized according to (10.2).

$$s^*(\vec{x},t) = \tilde{s}(\vec{x},t) + s'(\vec{x},t) \tag{10.2}$$

For convenience the arguments in brackets are dropped in the further discussions.

Several statistical tools exist to extract the coherent component from the time series of a flow field variable.
Classical tools like the Fast Fourier Transform (FFT) require a rather high temporal resolution of the data samples and long measurement times if low frequencies are to be resolved. It is therefore more suited for LDA, HW, or time resolved PIV measurement techniques. The dominant frequencies with their respective energetic content can then be determined from the Fourier spectrum. A phase average of the flow field variable $\langle s \rangle$ can be easily calculated from the time series.
A straightforward way of determining $\tilde{s}$ with measurement techniques of lower temporal resolution like PIV is to trigger the measurement system on a certain phase of the phenomenon that is to be observed. The coherent component is obtained by subtracting the mean $\overline{s}$ from the phase average $\langle s \rangle$:

$$\tilde{s} = \langle s \rangle - \overline{s} \tag{10.3}$$

The resulting phase average is valid as long as the phase angle can be accurately determined from an additional measurement signal (for example a hot wire placed in the flow) or by prescribing the desired frequency and phase by means of an actuator. Unfortunately it is not always possible to determine the current phase angle by means of a measurement and in natural flows the characteristic frequency is not necessarily constant or the phase coherence is not given over prolonged temporal periods. In order to still obtain a meaningful Fourier spectrum the time series are usually separated into smaller chunks and the spectra are then averaged. For these series a coherent phase relation is assumed. As a result of the then shorter time series for which the FFT is performed the frequency resolution decreases.

A different approach of investigating coherent structures is based upon statistical methods. The Proper Orthogonal Decomposition POD, sometimes called Singular Value Decomposition SVD, or Principal Component Analysis PCA, is a statistical method that is widely used in the investigation of turbulent flows Lumley [Lum67], Berkooz et al. [BHL93], Holmes et al. [HLB98], Tropea et

AL. (eds.) [TYF07]. A POD projects the input data upon a new, energetically optimal basis allowing the identification of patterns within large data-sets. Generally any flow field variable (pressure, concentration, velocity, etc.) can be used to compute a POD. In the analysis of turbulent flows the main interest is in the turbulent kinetic energy k. Therefore, the flow velocity is the variable of choice. A Low Order Model LOM of the flow can now be reconstructed by considering only the most energetic POD-modes (refer to HOLMES ET AL. [HLB98]), a technique that is also used in image compression algorithms. Depending on the energy content of the considered modes only a small number of modes is required to describe the original data-set with only a marginal loss of information in the lower energetic components. At this point it is emphasized that within the scope of this thesis the POD is used solely for the extraction of coherent flow structures – reduced order models are not considered here.

The mathematical background will now be discussed in some more detail following the lines of CHATTERJEE [Cha00] who provides an easy to understand introduction into the topic. For further details the works of TROPEA ET AL. (eds.) [TYF07, chapter 22.4], and HOLMES ET AL. [HLB98] should be consulted.

The general flow field variable $s(\vec{x}, t)$ is to be approximated by a finite sum, incorporating a separation of variables (10.4).

$$s(\vec{x}, t) \simeq \sum_{i=0}^{N} a_k(t) \cdot \Phi_k(\vec{x}) \tag{10.4}$$

As $N \to \infty$ the approximation becomes exact. In case of a discrete, finite data-set such as a sequence of N PIV snapshots, (10.4) is also exact if all snapshots are considered. A number of choices exist for the functions $\Phi_k(\vec{x})$ — Fourier series, Chebyshev polynomials, Legendre polynomials, etc.. The POD offers yet another choice that has certain advantages as discussed in the following. The POD basis functions are orthonormal, they are defined such that the approximation for each $n \leq N$ is optimal in a least squares sense, and the sequence of $\Phi_k(\vec{x})$ is optimal. The last statement means that the first n basis functions give the best possible n-term approximation of the original data-set. Functions with these characteristics are termed the *proper orthogonal modes* of $s(\vec{x}, t)$.

To perform a POD on a data-set consisting of N PIV snapshots the velocity fields are arranged column-wise in the matrix A. In order to reduce the numerical cost it takes to perform the POD a subset of each data-set can be taken. This subset needs to be similar for all snapshots and should include the spatial region of interest. The last requirement can be full-filled for example by considering only regions with a considerable level of turbulent kinetic energy TKE. In practice a singular value decomposition SVD is computed (in this case by calling the python function `numpy.linalg.svd`). The SVD of A is defined as (10.5):

$$A = U\,\Sigma\,V^T \tag{10.5}$$

If A is of size $N \times m$, then U and V are orthogonal matrices of sizes $N \times N$ and $m \times m$, respectively. Σ is a $N \times m$ diagonal matrix with the positive numbers σ_i as diagonal elements and arranged in decreasing order. They are called the singular values of A and their distribution over the mode number is shown in Fig. 10.4 for the cases considered here.
By setting $Q = U\,\Sigma$ (10.5) can be rewritten resulting in (10.6):

$$A = Q\,V^T = \sum_{i=1}^{N} q_i\,v_i^T \tag{10.6}$$

This represents the discrete form of the original equation (10.4). In this case the approximation is exact because of the finite data-set of N PIV snapshots.
A *proper orthogonal mode* of high energetic content, e.g. a large singular value σ, is usually interpreted as a coherent flow structure Oberleithner et al. [OSN+11, p. 18]. The POD can therefore be described as a statistical tool for identifying the dominating, reoccurring structures in a given flow field database, e.g. the large coherent structures.

When a flow configuration is governed by periodic phenomena such as convecting vortices, or precessing vortex cores this will be reflected in the occurrence of so called *corresponding modes*. These mode-pairs are identified by a similar energy content, e.g. compare energy content of the first two modes in Fig. 10.4b. The phase portrait of the two modes is obtained by plotting the temporal coefficient

of one mode over the others. A typical "donut shape" of the phase portrait is indicative of a periodic phenomenon (Oberleithner et al. [OSN+11]). From the phase portrait of the two corresponding modes k and l each of the N snapshots can be associated with a phase angle Ψ_{POD} according to (10.7):

$$\Psi_{\mathrm{POD}} = \arctan\left(\frac{q_l}{q_k}\right) \tag{10.7}$$

This technique of reconstructing the phase angle from corresponding POD modes is described in detail in the works of Oberleithner [Obe12] and Frederich [Fre10]. It allows to associate a phase angle (based on the selected corresponding modes) to uncorrelated PIV snapshots. Note that no frequency information can be extracted with this method. The phase reconstruction technique is utilized here to estimate the coherent component in the unactuated baseline flow field as well as for the control flow fields. It is emphasized that a phase triggered PIV was not performed in this study – all phase information was determined through POD phase reconstruction based on the two modes of highest energy.
When the phase angle is determined the velocity vectors can be split into a mean, a coherent, and an incoherent component by the triple decomposition that was discussed above and resulted in equations (10.1) and (10.2). This was done by sorting the PIV snapshots by increasing phase angle, subtracting $\overline{s}$ to obtain s^*, and then separating the coherent ($\tilde{s}$) from the incoherent, i.e. random (s') component. The separation was done by first interpolating onto equidistant phase angles. A manually tuned low pass filter was then applied to the data to obtain $\tilde{s}$, which was then subtracted from s^* to yield s'.

10.5.2 Data Evaluation

A total of 942 PIV snapshots was used in the calculation of the POD for each of the configurations. From the relative modal energy content shown in Fig. 10.4 it is observed that the respective first two modes contain a significant amount of energy (baseline: 7.7% and 9.0%, control: 10.1% and 11.8%). The first mode would usually represent the mean flow field. Here, the mean velocity field was subtracted from each of the snapshots and therefore the first mode already describes

a variation, e.g. the flow dynamics. Compared to the baseline case it is interesting to note that in the control case mode one and two not only contain more energy, but also the transition to higher modes ≤ 3 is accompanied by a more dramatic reduction in energy. This can be explained by the occurrence of large coherent structures (LCS) as a result of actuation. These structures are highly energetic and are commonly associated with an energy transfer across a shear layer [Hus83].

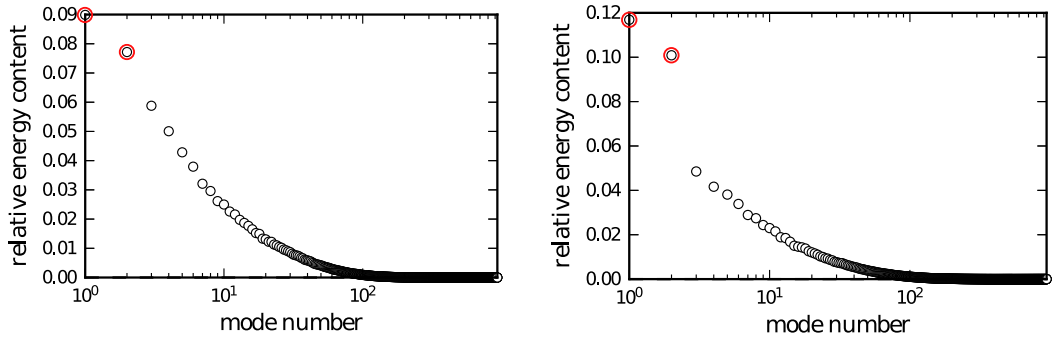

(a) baseline *(b)* $F^* = 0.12$

Fig. 10.4: Energy content over mode number for baseline and $F^* = 0.12$ cases. Phase reconstruction based on first two modes (marked by red circles). Mean flow field was subtracted from POD input data.

In the next step the phases were reconstructed based on the respective first two modes and the flow fields were decomposed into their coherent and incoherent components. With this approach the flow dynamics were studied by comparing the distribution and absolute levels of coherent $\tilde{k}$ and incoherent k' kinetic energy for the baseline case and the different actuation frequencies. The sum of the two, e.g. the total kinetic energy k^*, is calculated from the Reynolds normal stresses according to (10.8).

$$k^* = 1/2 \left(\overline{u^{*2}} + \overline{v^{*2}} + \overline{w^{*2}} \right) \tag{10.8}$$

The flow dynamics were correlated to the characteristic features of the mean flow fields (e.g. see chapter 10.3) and the differences in the spatial distributions of coherent and incoherent kinetic energy are discussed in the context of the literature.

The spatial distributions of k' and $\tilde{k}$ are shown in figures 10.5 and 10.6, respec-

tively. Depicted here in detail is only a comparison of the baseline case with the optimum control case at $F^*_{\text{opt}} = 0.121$. The effects of the other actuation frequencies are summarized in overview plots and will be discussed below.

In the baseline case the incoherent kinetic energy (figure 10.5) reaches its peak values in the shear layers which are emanating from the leading and the trailing edges. It is interesting to note that $\tilde{k}$ is distributed quite differently as shown in Fig. 10.6. Here, the peak values are reached downstream of the wing in an area that is located in-between the two shear layers. Interestingly this area coincides with the detached stagnation point that was observed in the qualitative flow field which was discussed in Fig. 10.2a. This stagnation point periodically moves up and down in transversal direction. The movement is driven by the interaction of the LE and TE shear layers. A similar observation was made by Leder [Led92], who investigated the wake of a sphere. Leders results from LDA measurements confirm that the maximum level of coherent kinetic energy is reached downstream of the body in the vicinity of a detached stagnation point. The author states that a detached saddle-point can be observed in the flow field, which periodically moves up and down between the shear layers.

The re-circulation zone above the wing, in-between the shear layers is characterized by fluid of low energy, e.g. stagnant fluid. This suggests that the vortical structures reside within the shear layers at a distance from the wings upper surface. The respective kinetic energy distributions reveal that the periodic, coherent structure downstream of the wing is more energetic than the structures in the shear layers. In order to get more insight into the flow dynamics time resolved pressure measurements were conducted on a two-dimensional wing (see chapter 8, p. 77 ff.). Periodic fluctuations in the surface pressures were detected. The low frequency pressure signals were all in phase in chord-wise direction, suggesting that a convective shedding of flow structures does not occur in the baseline case (see chapter 8). It is assumed that the global, low frequency pressure fluctuations can be related to the transversal movement of the detached stagnation point, which impresses its pressure signature on the wing.

The following discussion is focused on the control case and the respective distributions of k' and $\tilde{k}$ as depicted to the right in figures 10.5 and 10.6. In contrast to the baseline case coherent and incoherent kinetic energy have similar spatial

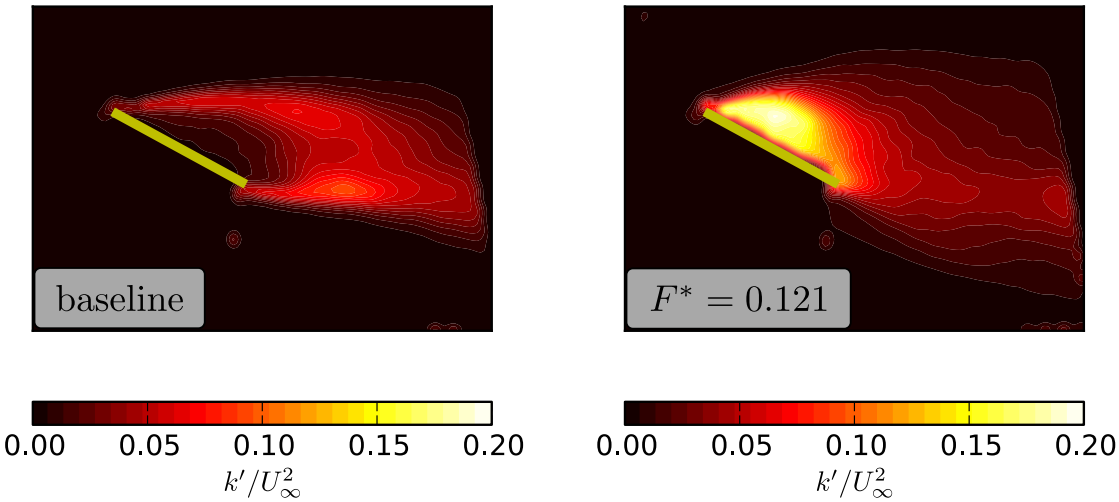

Fig. 10.5: Spatial distribution of normalized incoherent kinetic energy k'/U_∞^2.

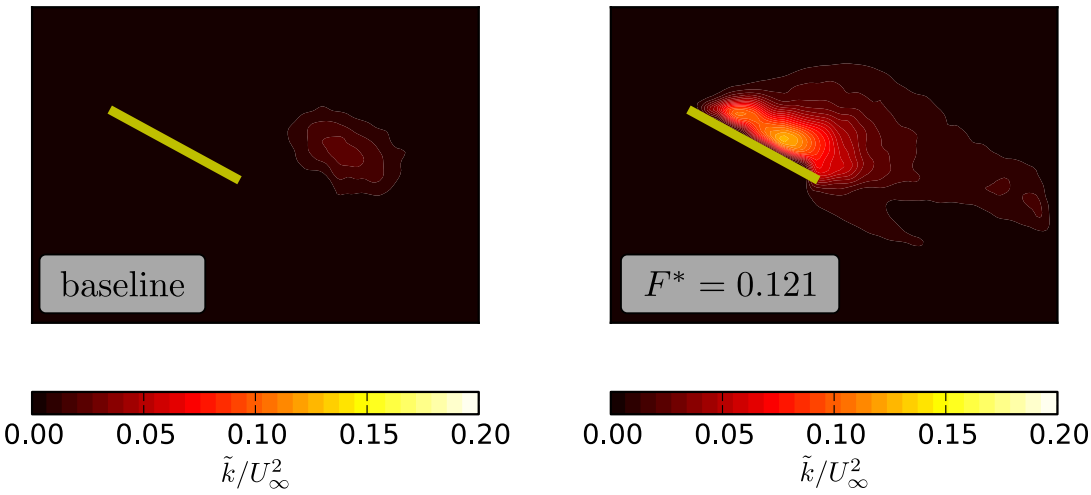

Fig. 10.6: Spatial distribution of normalized coherent kinetic energy $\tilde{k}/U_\infty^2$.

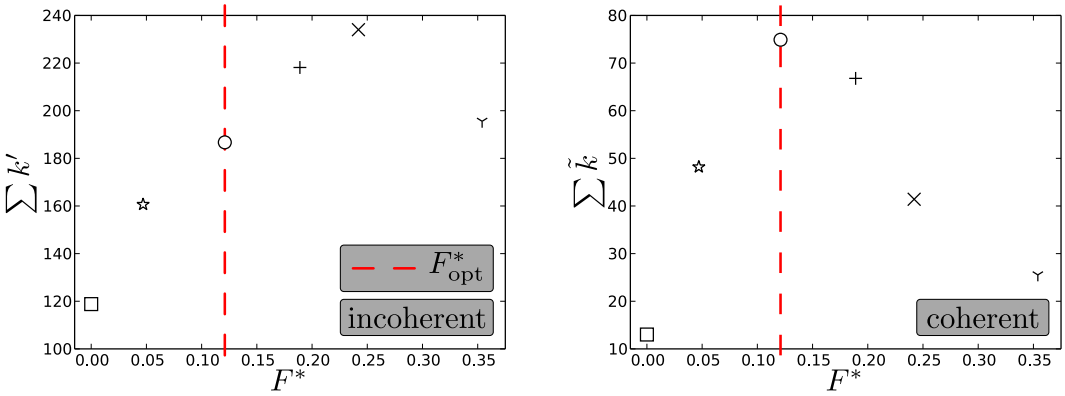

Fig. 10.7: Summed kinetic energy for varying actuation frequencies. Baseline: $F^* = 0.00$.

distributions, reaching their respective peak values in the vicinity of the wings upper surface close to the reattachment point at $x/c_R = 0.83$ (compare to the LIC-visualization in Fig. 10.2b). The high level of $\tilde{k}$ near the wings suction side is indicative of strong, periodically shedding vortical structures. This was confirmed by the time resolved pressure measurements that were discussed above. Here a phase shift between consecutive pressure port signals was observed in the control case, which is indicative of a convective movement of vortical structures in chord-wise direction. The pressure measurements also revealed that the strongest pressure footprint occurs when forcing at F^*_{opt}. This observation is backed by considering the summed kinetic energy, which is shown in Fig. 10.7 for a range of actuation frequencies and the baseline case. The distribution of $\sum \tilde{k}$ shown in the right plot suggests that at F^*_{opt} the vortical structures reach their maximum strength. It is interesting to note that $\sum k'$ increases approximately linearly to peak at a higher frequency of $F^* = 0.242$. The levels of both k' and $\tilde{k}$ and their respective sums are larger in the control cases, which is presumably caused by the actuation itself.

A more detailed view of the spatial distributions of coherent and incoherent kinetic energies is obtained by calculating $\sum_y k$, i.e. the sum along y for constant x/c. The distributions are shown in Fig. 10.8. Similar distributions of k' are obtained for the control cases (right plot). From the leading edge k' increases linearly until a first maximum is obtained at approximately mid-chord. A second, higher max-

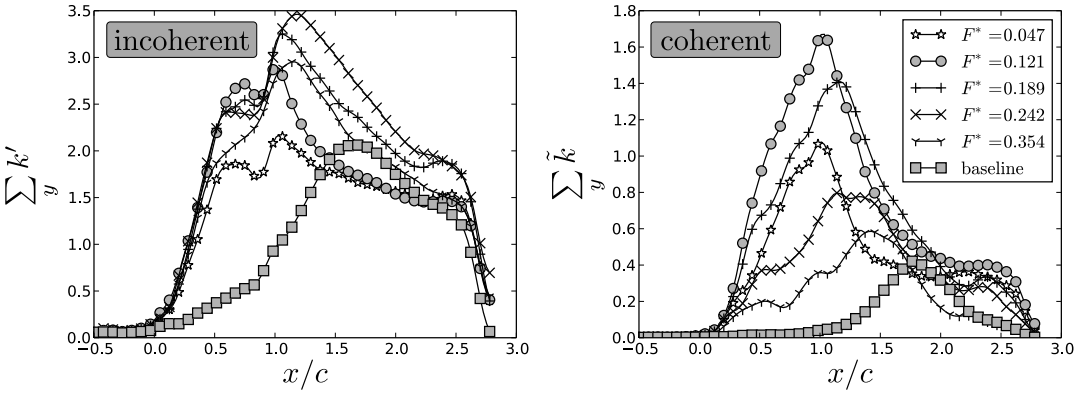

Fig. 10.8: Chord-wise (x/c) distribution of summed kinetic energies for baseline and several control cases.

imum is reached in the vicinity of the trailing edge. The decrease for $x/c > 2.5$ is caused by the boundaries of the PIV-interrogation area and therefore does not have any physical meaning. The baseline case has a distribution that differs from the control cases in the sense, that the initial increase in k' is weaker and a (lower) maximum is reached downstream of the wing at $x/c \approx 1.6$. An interesting observation can be made when considering the coherent kinetic energy distribution in the right plot. The location where the maximum (summed) coherent kinetic energy is reached varies with F^*. At F^*_{opt} the steepest increase in energy is detected and the peak is closest to the leading edge. For $F^* > F^*$opt the peak level decreases and moves further towards the trailing edge. As already mentioned in the discussion of Fig. 10.6 the baseline case has its coherent kinetic energy concentrated downstream of the wing in the vicinity of the detached stagnation point.

10.6 Finite Span Effects

As a result of the finite span and the associated pressure compensation in the wing tip region cross-flows can be observed on the wing. The higher pressure on the lower surface and the lower pressure on the upper surface induce a span-wise directed flow. On the suction side this flow is directed towards the centerline, while on the pressure side it is necessarily directed towards the respective wing tips. A lift increase through flow control increases the circulation about the wing, which increases the driving pressure difference between pressure and suction side. Therefore applying control is expected to increase the crosswise flow component and in fact this can be observed considering Fig. 10.9.

At three span-wise stations the respective crosswise component w/U_∞ of baseline and optimum control are compared. Immediately above the wing the region of crosswise flow is relatively small and concentrated in the leading edge shear layer region. Approximately $1 - 1.5$ chord lengths downstream of the wing large cross-flow regions can be observed. The cross-flow magnitude increases as the measurements plane is moved towards the wing tip, with the largest magnitudes registered in the control case.

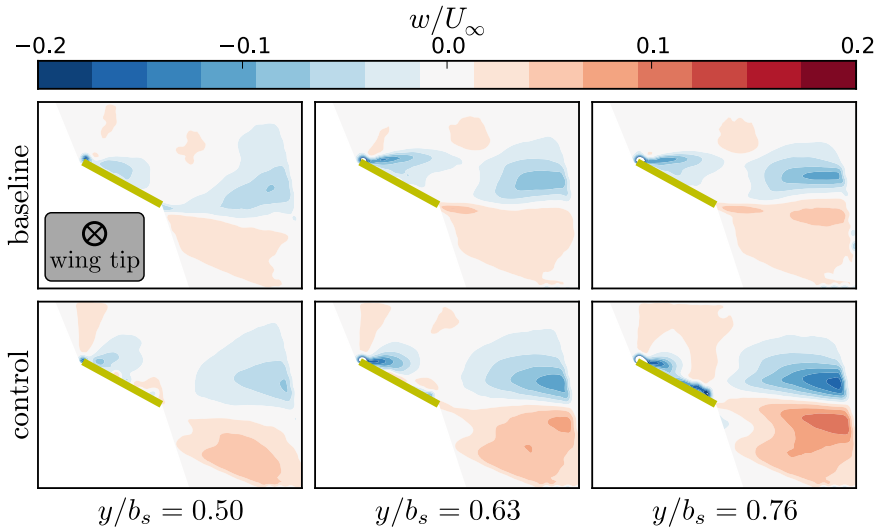

Fig. 10.9: Span-wise development of through-plane velocity component w. $AR = 2.66$ rectangular plan-form 3D wing at $\mathrm{Re} = 17\,000$

11. FREQUENCY SCALING REVISITED

In this chapter the frequency scaling will be re-addressed. By evaluating the available PIV-data it is possible to scale the optimum forcing frequency in yet another way. With this scaling it is possible to clearly classify the flow phenomena involved in the lift-enhancement.

Refer again to Fig. 6.2 in chapter 6.3. It was noted that the frequency scan data obtained at different angles of attack collapse when non-dimensionalized with the wings transverse height for frequencies smaller than the optimum forcing frequency ($F^* \leq F^*_{\mathrm{opt}}$). A similar observation was made by SIGURDSON [Sig95], who studied the separation bubble downstream of the blunt edge of a co-axially aligned cylinder. His study was aiming at a pressure drag reduction. The separating shear layer was periodically forced along the forward circumferential and the reattachment length, bubble height, and base drag were recorded. SIGURDSON observed a clear dependency of the base drag on forcing frequency with a defined minimum at dimensionless frequencies of $0.16 \leq F_{\mathrm{ex}}\, h/U_{\mathrm{s}} \leq 0.4$, with F_{ex} the excitation frequency, h the bubble height, and U_s the velocity at the separation point. When different forcing amplitudes were applied the drag-reduction data collapsed in the sub-optimal forcing frequency range, similar to the observations discussed above in the context of Fig. 6.2. The author proposes a frequency scaling based on the vortex diameter (i.e. the bubble height h), and the velocity at the location of separation U_s. This scaling was originally used by ROSHKO [Ros55] to compare vortex shedding from cylinders of varying cross-sectional shapes, a normal plate, and a 90° wedge.

SIGURDSON found that two inherently different instabilities are involved in the separated flow region downstream of the cylinder face. These are the Kelvin-Helmholtz shear-layer instability and a shedding-type instability of the entire sep-

aration bubble. The author notes that the shedding is *like* von Kármán vortex shedding. The difference is that the vortex interaction is with image vortices due to the presence of the wall and therefore the dimensionless natural shedding frequency is approximately one half of the cylinder shedding frequency.
The optimum frequencies for drag reduction were found to be much lower than the Kelvin-Helmholtz shear layer frequency and two to five times higher than the natural shedding frequency.
It is emphasized that the control goal of SIGURDSON was to reduce the drag of an axially aligned cylinder. The main drag reduction effect was due to a reduction of pressure on the frontal face of the cylinder. Both the control goal and the geometrical configuration are quite different to the flow control study that was conducted within the scope of this thesis. The range of optimum forcing frequencies is therefore different for the two problems. Nonetheless SIGURDSONS work provided important insight into the frequency scaling, and the fluid mechanical mechanisms involved.
Applying the scaling of ROSHKO and SIGURDSON to the flat plate wing with leading edge forcing requires the determination of the velocity at the point of separation U_s from quantitative flow measurements. Refer to Fig. 11.1 which shows the forced mean flow field captured by a PIV measurement that was already discussed in chapter 10.3. The velocity at the point of separation is found to be $U_\mathrm{s} = 3.0\,\mathrm{m/s}$.

Re-scaling the optimum forcing frequency with regard to U_s results in a dimensionless frequency of 0.08. Here it is assumed that $h = c\,\sin(\alpha)$ is a reasonable assumption for the height of the separation bubble.
In fact SIGURDSON [Sig95] in his paper summarized non-dimensionalized shedding frequencies from several different geometries collected from various references. For both free- and wall-bounded separation bubbles the author finds the appropriately scaled dimensionless frequencies to be close to the value of 0.08. It is interesting to note that the data includes not only natural shedding cases but also one case of flow control on a two dimensional LRN(1)-1007 low Reynolds number airfoil at post-stall angles of attack in the range $16° \leq \alpha \leq 30°$. This investigation was conducted by ZAMAN [Zam92], who adapted the aforementioned scaling and realized that the optimum forcing frequency was orders of magnitude lower

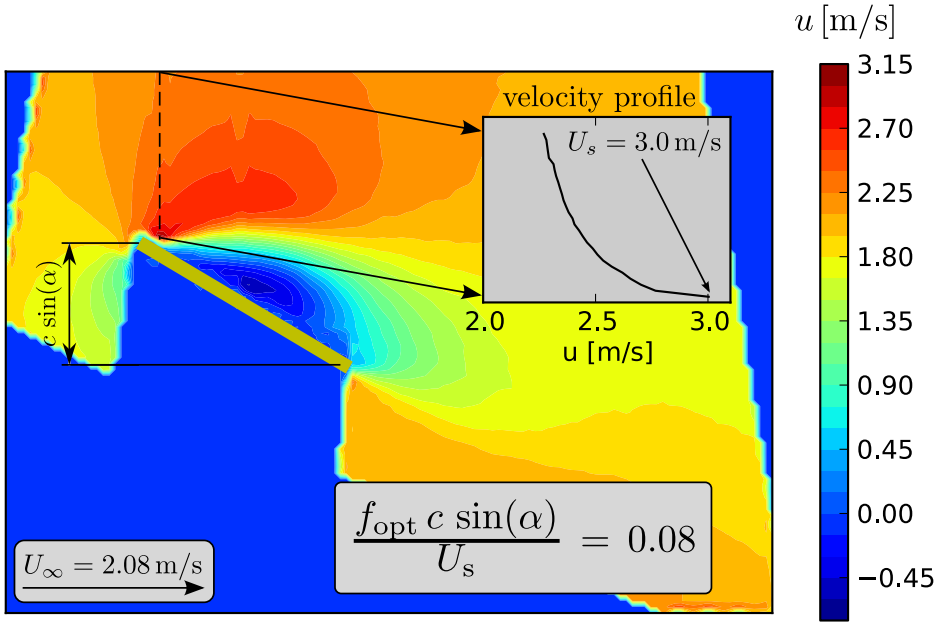

Fig. 11.1: Mean stream-wise velocity component with forcing at F^*_{opt}. Illustrating the determination of separation velocity U_{s}.

than the Kelvin-Helmholtz instability frequency and close to the shedding-type instability frequency. The excitation was introduced externally using an acoustic driver/woofer.

To this point it was merely stated that the optimum forcing frequency *for post-stall angles of attack* is related to the respective bluff body shedding frequency. This was shown above and some insight was obtained in the discussion of the spatial distribution of the coherent kinetic energy in chapter 10.5 and its dependency on the forcing frequency. The reason why the bluff body shedding frequency is the optimum forcing frequency in order to maximize the lift is discussed in more detail in the next chapter. Although the discussion is focused on *flat plate wings* at *post-stall angles of attack* some of the findings might also be applied to wings with airfoil sections as long as they are considered at post-stall angles of attack.

12. BLUFF BODY FREQUENCY FORCING: THE OPTIMUM

A number of authors who investigated flow control at post-stall angles of attack on (flat plate) wings state that *"the optimum forcing frequency is close to the natural bluff body shedding frequency"*. It is felt by this author that this topic has not been discussed to a satisfactory degree. In fact, the optimum forcing frequency for flat plate configurations can be determined by a simple discussion, which is summarized below:

1. Goal: maximize lift.
2. On a flat plate wing lift and drag are coupled through the definition of aerodynamic efficiency $C_L/C_D = 1/\tan(\alpha)$.
3. $\Rightarrow \Delta C_L/C_{L,bl} = \Delta C_D/C_{D,bl}$, or: *lift increase goal* $\equiv$ *drag increase goal*.
4. Bluff bodies generate the largest C_D when periodic vortex shedding occurs (see HUCHO[Huc11], p. 131).

Idea: If we could make our *"wing"* behave like a *"bluff body"* we maximize C_D (and thus C_L via the coupling $C_L/C_D = 1/\tan(\alpha)$).

5. We make the wing behave like a bluff body by forcing the flow field with the respective bluff body frequency...
6. ...and thus maximize C_L.

These points are now discussed in some more detail. Refer again to chapter 5.1, where it was shown that the aerodynamic efficiency of flat plate wings cannot be improved by means of flow control. This is further illustrated in Fig. 12.1. Here the theorem of intersecting lines is applied to the case of *normal force increase* by a factor of x. Increasing the normal force N by, say, 10% results in a 10% increase in

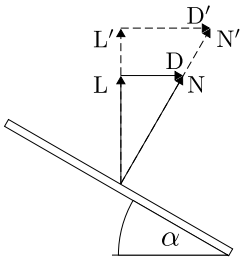

$$\Rightarrow \quad \begin{aligned} N' &= x \cdot N \\ L' &= x \cdot L \\ D' &= x \cdot D \end{aligned} \quad \Rightarrow \quad \boxed{\begin{array}{c} \textit{lift increase goal} \\ \equiv \\ \textit{drag increase goal} \end{array}}$$

Fig. 12.1: Sketch illustrating that maximizing the lift is equivalent to maximizing the drag (under the assumptions discussed above).

lift *and* drag. Lift and drag cannot be modified independently due to the coupling through the definition of aerodynamic efficiency (repeated here for convenience):

$$\frac{C_L}{C_D} = \frac{1}{\tan(\alpha)} \tag{12.1}$$

The subsequent discussion is valid under the following assumptions:

- Infinitely thin flat plate wings.
- Skin friction neglected.
- $\alpha > \alpha_{\text{stall}}$.
- Forcing of flow along leading edge of wing.

Here, post-stall angles of attack implies that in the baseline case there exists an open separation bubble above the wing. This bubble does not close within the chord length of the wing, i.e. the flow does not reattach to the wing.

Considering the definition of C_L/C_D above, the *lift increase goal* is therefore equivalent to a *drag increase goal*. One way of maximizing the drag ($\equiv$ lift) of a "wing" is by forcing it to behave like a bluff body in its state of maximum drag production. Here periodic vortices are shed from the bluff body at a typical bluff body shedding frequency. The low-pressure region of the vortex cores is impressed upon the body, resulting in minimum base-pressure and, therefore, a maximum in drag.

For bluff bodies a number of techniques have been suggested to reduce the drag. These are summarized in the reference work of Hucho[Huc11]. One possible way

is to interfere with the vortex-formation downstream of the body. This can be accomplished, for example, by introducing a splitter plate, that extends downstream from the rear-end of the body (Roshko[Ros55]). The drag-reducing effect is mainly due to a downstream-shift of the vortex-formation. As a result, the vortex-induced low-pressure on the back of the body is reduced, as is the drag. Or, to put in other words, the drag of a body can be increased by moving the shedding vortices closer to the rear-face of the body. This is exactly how the lift is maximized here - by forcing the flow above the wing, at the leading edge, the vortex-formation is triggered close to the body and the vortices can impress their low-pressure cores to the wings upper surface. This argumentation is supported by the distributions of coherent kinetic energy $\tilde{k}$ for baseline and (optimum) control cases that were shown in Fig. 10.6. Note how the region of increased $\tilde{k}$ was shifted from behind the wing to a region immediately above the wing when control was applied at the optimum forcing frequency.

Clearly, the two phenomena: lift-increase on low aspect ratio wings at post-stall angles of attack, and bluff body vortex shedding are closely related. It was shown why the bluff body shedding frequency is indeed the optimum forcing freqeuncy for lift increase in the cases discussed throughout this work.

13. SUMMARY AND CONCLUDING REMARKS

Within the scope of this thesis flow control on low aspect ratio wings was experimentally investigated at Reynolds numbers Re $\leq$ 50 000 and aspect ratios AR ≤ 2.66. The experiments were conducted mainly at post-stall angles of attack of $25° \leq \alpha \leq 31°$. Additionally angle of attack sweeps were performed at the identified optimum forcing frequency. The risk reduction phase studies on semi-span wings of varying aspect ratios provided valuable information about the governing flow control parameters and actuator placement locations. The experience gained within this phase could be directly transferred to the three dimensional wing configurations. The baseline lift curves showed good agreement to published data.

Flow control effectiveness was compared to the respective baseline cases, with the focus on maximizing the obtainable lift increase ΔC_L. A distinct dependency of ΔC_L on the dimensionless actuation frequency F^* was observed, where the optimum forcing frequency was found to be $F^*_{\text{opt}} = 0.12$ for most of the tested configurations. The optimum frequency was found to be much lower than the Kelvin-Helmholtz frequency of the leading edge shear layer. It was rather in the region of the bluff body shedding frequency.

This was further investigated and by scaling the forcing frequency with the separation velocity U_s instead of the free stream velocity U_∞ an optimum dimensionless forcing frequency of 0.08 is obtained. This frequency is typical for the vortex shedding on bluff bodies. A simple set of arguments was given to illustrate why the bluff body shedding frequency is the optimum forcing frequency for lift increase on flat plate wings at post-stall angles of attack.

Genrally only at post-stall angles of attack a positive actuation effect could be observed. The pre-stall lift curves remained unchanged by the (pulsed) actuation – only if the actuator was placed on the trailing edge pressure side, blowing continuously upstream, a pre-stall lift increase effect could be observed. In this case

the actuator acted as a circulation control device and required considerably more power input in order to generate a comparable ΔC_L as compared to pulsed actuation.

The flow dynamics were studied through a detailed PIV study on the three dimensional wings as well as through time resolved pressure measurements on a two dimensional flat plate wing. The dominating coherent structures were identified by applying a proper orthogonal decomposition (POD) to the PIV datasets. Through a triple decomposition and calculation of the turbulent kinetic energy terms the effect of actuation on the dynamic structures in the flow field were studied. In the baseline case high levels of coherent kinetic energy were observed downstream of the wing in the vicinity of a detached separation point. This was interpreted to be caused by an interaction of the leading and trailing edges shear layers, which causes global pressure fluctuations in the flow field around the wing. At the optimum forcing frequency the flow reattached to the wings suction side (in a time-mean sense). This was accompanied by high levels of coherent kinetic energy immediately above the wings upper surface. It was concluded that with each actuation phase a span-wise vortex is generated which grows in size as it is shed downstream by convection with the mean flow. Similarities were drawn with bluff body vortex shedding and drag-reduction techniques on bluff bodies.

A roll control study was conducted on a three-dimensional wing hinged with a rotational degree of freedom along the roll axis. It was shown that hinge-less roll-control is feasible, but the obtainable roll-rates were too low for a direct practical application.

The utilized dielectric barrier discharge (DBD) actuators were found to be ideal for experimental flow control studies at low Reynolds numbers. Their flexibility in placement, geometry, induced blowing direction, frequency range, and amplitude authority are advantageous for investigations covering a wide range of parameter variations. For possible practical applications the durability of the dielectric material needs to be improved and the momentum output should be increased. If an integration into micro air vehicles (MAVs) is envisaged the high voltage (HV) generators need to be miniaturized as well. In order to estimate a Fig. of merit of the flow control scheme the actuator output C_μ was quantified through thrust measurements performed on a laboratory scale. Within the operational limita-

tions of the HV generator and the actuators themselves the effects of geometric electrode arrangement, ionization frequency, and applied peak-to-peak voltage are reported and brought into context with the flow control study on the low aspect ratio wings. It was noted that the typical actuator configuration that was used in the flow control study on the flat plate wings induced a significantly higher momentum than a generic (flat) actuator. The reason was that the actuators electrode was wrapped around the blunt edges of the wing. This affects the electrical field strength downstream of the exposed electrode resulting in larger induced forces and thus momentum.

BIBLIOGRAPHY

[AD59] Abbott, I.H. ; Doenhoff, A.E. von: Theory of Wing Sections. Dover Publications, Inc. New York, 1959

[And05] Anderson, J.D.: Introduction to Flight. McGraw–Hill, 2005

[BB01] Kapitel 10. In: Broeren, A.P. ; Bragg, M.B.: Unsteady Stalling Characteristics of Thin Airfoils at Low Reynolds Number. Progress in Astronautics and Aeronautics, Vol. 195, 2001, S. 191–213

[BHL93] Berkooz, G. ; Holmes, P. ; Lumley, J.L.: The Proper Orthogonal Decomposition in the Analysis of Turbulent Flows. In: Annual Review of Fluid Mechanics 25 (1993), S. 539–575

[BRT+08] Brunton, S.L. ; Rowley, C.W. ; Taira, K. ; Colonius, T. ; Collins, J. ; Williams, D.R.: Unsteady aerodynamic forces on small-scale wings: experiments, simulations and models. In: 46th AIAA Aerospace Sciences Meeting and Exhibit, Reno, NV AIAA-2008-520 (2008)

[BUV+09] Bachmann, M. ; Utehs, S. ; Vey, S. ; Paschereit, C.O. ; Greenblatt, D.: Plasma-Based Active Flow Control on Low Reynolds Number Airfoils. In: 49th Israel Annual Conference on Aerospace Sciences, 4-5 March 2009, Tel Aviv and Haifa, Israel, 2009

[CC83] Cantwell, B. ; Coles, D.: An experimental study of entrainment and transport in the turbulent wake of a circular cylinder. In: Journal of Fluid Mechanics 136 (1983), S. 321–374

[CEW10] Corke, T.C. ; Enloe, C.L. ; Wilkinson, S.P.: Dielectric Barrier Discharge Plasma Actuators for Flow Control. In: Annual Review of Fluid Mechanics 42 (2010), S. 505–529

[Cha00] Chatterjee, A.: An introduction to the proper orthogonal decomposition. In: Current Science 78 (2000), Nr. 7, S. 808–817

[CHP04] Corke, Thomas C. ; He, Chuan ; Patel, Mehul P.: Plasma Flaps and Slats: An Application of Weakly-Ionized Plasma Actuators. In: 2nd AIAA Flow Control Conference, Portland, OR AIAA 2004-2127 (2004), Juni. – scan

[CJPO02] Corke, Thomas C. ; Jumper, Eric J. ; Post, Martiqua L. ; Orlov, Dmitry M.: Application of Weakly-Ionized Plasmas as Wing Flow-Control Devices. In: AIAA conference AIAA 2002-0350 (2002)

[CL93] Cabral, B. ; Leedom, L.C.: Imaging Vector Fields Using Line Integral Convolution. In: Proceedings of the 20th annual conference on Computer graphics and interactive techniques, Anaheim, CA, USA (1993), S. 263–270

[CP05] Corke, T.C. ; Post, M.L.: Overview of Plasma Flow Control: Concepts, Optimization, and Applications. In: 43rd AIAA Aerospace Sciences Meeting and Exhibit, Reno, NV AIAA-2005-563 (2005), S. 1–15

[CPO07] Corke, Thomas C. ; Post, Martiqua L. ; Orlov, Dmitry M.: SDBD plasma enhanced aerodynamics: concepts, optimization and applications. In: Progress in Aerospace Sciences 43 (2007), August, S. 193–217. http://dx.doi.org/10.1016/j.paerosci.2007.06.001. – DOI 10.1016/j.paerosci.2007.06.001

[DG97] Deng, Q. ; Gursul, I.: Vortex breakdown over a delta wing with oscillating leading edge flaps. In: Experiments in Fluids 23 (1997), August, Nr. 4, S. 347–352. http://dx.doi.org/10.1007/s003480050121. – DOI 10.1007/s003480050121

[DW04] Darabi, A. ; Wygnanski, I.: Active management of naturally separated flow over a solid surface. Part 1. The forced reattachment process. In: Journal of Fluid Mechanics 510 (2004), Juli, S. 105–129. http://dx.doi.org/10.1017/S0022112004009231. – DOI 10.1017/S0022112004009231

[DWG11] DeSalvo, M. ; Whalen, E. ; Glezer, A.: High-Lift Enhancement Using Active Flow Control. In: 29th AIAA Applied Aerodynamics Conference, Honolulu, Hawaii AIAA-2011-3355 (2011)

[EBWT96] Ellington, C.P. ; Berg, C. van d. ; Willmot, A.P. ; Thomas, A.L.R.: Leading-edge vortices in insect flight. In: Nature 384 (1996), S. 626–630

[EMFB05] Enloe, C.L. ; McLaughlin, T.E. ; Font, G.I. ; Baughn, J.W.: Parameterization of Temporal Structure in the Single Dielectric Barrier Aerodynamic Plasma Actuator. In: 43rd AIAA Aerospace Sciences Meeting and Exhibit AIAA 2005-0564 (2005), jan. – scan

[EMVF04] Enloe, C.L. ; McLaughlin, T.E. ; VanDyken, R.D. ; Fischer, J.C.: Plasma Structure in the Aerodynamic Plasma Actuator. In: 42nd AIAA Aerospace Sciences Meeting and Exhibit AIAA 2004-0844 (2004), jan. – scan

[FF90] Fiedler, H.E. ; Fernholz, H.-H.: On Management And Control Of Turbulent Shear Flows. In: Progress in Aerospace Sciences 27 (1990), S. 305–387

[FL06] Fish, F.E. ; Lauder, G.V.: Passive and Active Flow Control by Swimming Fishes and Mammals. In: Annual Review of Fluid Mechanics 38 (2006), S. 193–224

[Fre10] Frederich, O.: Numerische Simulation und Analyse turbulenter Strömungen am Beispiel der Umströmung eines Zylinderstumpfes mit Endscheibe, Technische Universität Berlin, Diss., 2010

[GBS11] GBS Elektronik, Dresden: Minipulse 1 HV generator. January 2011. – http://www.gbs-elektronik.de/leistungen/hochspannungspulstechnik/pulsgeneratoren-fuer-spezialanwendungen/

[GGR+06] Goeksel, B. ; Greenblatt, D. ; Rechenberg, I. ; Nayeri, C.N. ; Paschereit, C.O.: Steady and Unsteady Plasma Wall Jets for Separation and Circulation Control. In: 3rd AIAA Flow Control Conference AIAA 2006-3686 (2006), jun

[GGR+08] Greenblatt, D. ; Goeksel, B. ; Rechenberg, I. ; Schuele, C.Y. ; Romann, D. ; Paschereit, C.O.: Dielectric Barrier Discharge Flow Control at Very Low Flight Reynolds Numbers. In: AIAA Journal 46 (2008), Nr. 6, S. 1528–1541

[GKNP08] Greenblatt, D. ; Kastantin, Y. ; Nayeri, C.N. ; Paschereit, C.O.: Delta-Wing Flow Control Using Dielectric Barrier Discharge Actuators. In: AIAA Journal 46 (2008), Juni, Nr. 6, S. 1554–1560. – Technical Note

[GSB95] Gursul, I. ; Srinivas, S. ; Batta, G.: Active control of vortex breakdown over a delta wing. In: AIAA Journal 33 (1995), Nr. 9, S. 1743–1745. – mentioned in DFG proposal

[GSS12] Greenblatt, D. ; Schneider, T. ; Schuele, C.Y.: Mechanism of Flow Separation Control Using Plasma Actuation. In: Physics of Fluids 24 (2012)

[GW00] Greenblatt, D. ; Wygnanski, I.J.: The control of flow separation by periodic excitation. In: Progress in Aerospace Sciences 36 (2000), S. 487–545

[GW08] Greenblatt, D. ; Washburn, A.E.: Influence on Finite Span and Sweep on Active Flow Control Efficacy. In: AIAA Journal 46 (2008), S. 1675–1694

[HB85] Hoerner, S.F. ; Borst, H.V. ; Borst, H.V. (Hrsg.): Fluid-Dynamic Lift - Practical Information on Aerodynamic and Hydrodynamic Lift. 2nd. Liselotte A. Hoerner, 1985

[HLB98] Holmes, P. ; Lumley, J.L. ; Berkooz, G.: Turbulence, Coherent Structures, Dynamical Systems and Symmetry. Cambridge University Press, 1998

[Hol09] Holst, D.: Low aspect ratio wing plasma flow control at low Reynolds-numbers, Berlin Institute of Technology, Institut für Strömungsmechanik und technische Akustik (ISTA), Diplomarbeit, 2009

[Huc02] Hucho, W.-H.: Aerodynamik der stumpfen Körper. Vieweg, 2002

[Huc11] Hucho, W.-H.: Aerodynamik der stumpfen Körper. 2nd. Vieweg + Teubner Verlag, 2011

[Hus83] Hussain, A.K.M.F.: Coherent structures – reality and myth. In: Physics of Fluids 26 (1983), S. 2816–2850

[JCM09] Joe, W.T. ; Colonius, T. ; MacMynowski, D.G.: Optimized Control of Vortex Shedding from an Inclined Flat Plate. In: 39th AIAA Fluid Dynamics Conference, San Antonio, TX, USA AIAA-2009-4027 (2009)

[Led92] Leder, A.: Abgelöste Strömungen – Physikalische Grundlagen. Vieweg, 1992

[Lei06] Leishman, J.G.: Principles of Helicopter Aerodynamics. Cambridge University Press, 2006 (Cambridge Aerospace Series)

[Lin11] Lindner, M.: Kraftmessung an Plasma-Aktuatoren, Technische Universität Berlin, Diplomarbeit, 2011

[LSMM07] Likhanskii, A.V. ; Shneider, M.N. ; Macheret, S.O. ; Miles, R.B.: Optimization of Dielectric Barrier Discharge Plasma Actuators

Driven By Repetitive Nanosecond Pulses. In: 45th AIAA Aerospace Sciences Meeting and Exhibit AIAA 2007-633 (2007), jan

[LSO+07] Likhanskii, A.V. ; Shneider, M.N. ; Opaits, D.F. ; Miles, R.B. ; Macheret, S.O.: Numerical modeling of DBD plasma actuators and the induced air flow. In: 38th AIAA Plasmadynamics and Lasers Conference, Miami, FL AIAA 2007-4533 (2007), jun

[Lum67] Kapitel The structure of inhomogeneous turbulent flows. In: Lumley, J.L.: Atmospheric Turbulence and Radio Wave Propagation. Nauka, Moscow., 1967, S. 166–178

[LZF07] Leven, S. ; Zufferey, J.-C. ; Floreano, D.: A Simple and Robust Fixed-Wing Platform for Outdoor Flying Robot Experiments. (2007), 69–70

[MCW+09] Mabe, J.H. ; Calkins, F.T. ; Wesley, B. ; Woszidlo, R. ; Taubert, L. ; Wygnanski, I.: Single Dielectric Barrier Discharge Plasma Actuators for Improved Airfoil Performance. In: AIAA Journal tba (2009), S. tba

[MD01] Mitchell, A.M. ; Delery, J.: Research into vortex breakdown control. In: Progress in Aerospace Sciences 37 (2001), S. 385–418. http://dx.doi.org/10.1016/S0376-0421(01)00010-0. – DOI 10.1016/S0376–0421(01)00010–0

[MGSW05] Margalit, S. ; Greenblatt, D. ; Seifert, A.. ; Wygnanski, I.: Delta Wing Stall and Roll Control Using Segmented Piezoelectric Fluidic Actuators. In: AIAA Journal of Aircraft 42 (2005), S. 698–709

[MKIS07] Mueller, T.J. (Hrsg.) ; Kellogg, J.C. (Hrsg.) ; Ifju, P.G. (Hrsg.) ; Shkarayev, S.V. (Hrsg.): Introduction to the Design of Fixed-Wing Micro Air Vehicles. AIAA Education Series, 2007

[Mor09] Morse, D.R.: Experiments on a low aspect ratio wing at low Reynolds numbers, Oregon State University, Diss., 2009

[MTS06] Kapitel 2. In: Mueller, T.J. ; Torres, G.E. ; Srull, D.W.: Introduction to the Design of Fixed-Wing Micro Air Vehicles. AIAA Education Series, 2006, S. 39–107

[MTS07] Kapitel 2 Elements of Aerodynamics, Propulsion, and Design. In: Mueller, T.J. ; Torres, G.E. ; Srull, D.W.: Introduction to the Design of Fixed-Wing Micro Air Vehicles: Including Three Case Studies. AIAA Education Series, 2007, S. 39–107

[Mue01] Mueller, T.J. (Hrsg.): Fixed and Flapping Wing Aerodynamics for Micro Air Vehicle Applications. Progress in Astronautics and Aeronautics, Vol. 195, 2001

[Mue06] Kapitel 1. In: Mueller, T.J.: Introduction to the Design of Fixed-Wing Micro Air Vehicles. AIAA Education Series, 2006, S. 1–38

[NCH+07] Nelson, R.C. ; Corke, T.C. ; He, C. ; Othman, H. ; Matsuno, T. ; Patel, M.P. ; Ng, T.T.: Modification of the Flow Structure over a UAV Wing for Roll Control. In: 45th AIAA Aerospace Sciences Meeting and Exhibit AIAA 2007-0884 (2007), jan

[Ng89] Ng, T.T.: On Leading Edge Vortex and its Control. In: AIAA Atmospheric Flight Mechanics Conference, Boston, MA AIAA-1989-3346 (1989), August

[NKRD06] Nagib, H. ; Kiedaisch, J. ; Reinhard, P. ; Demanett, B.: Control Techniques for Flows with Large Separated Regions: A New Look at Scaling Parameters. In: 3rd AIAA Flow Control Conference, 5-8 June 2006, San Francisco, CA AIAA-2006-2857 (2006)

[OAH+07] Orlov, D.M. ; Apker, T. ; He, C. ; Othman, H. ; Corke, T.C.: Modeling and Experiment of Leading Edge Separation Control Using SDBD Plasma Actuators. In: 45th AIAA Aerospace Sciences Meeting and Exhibit AIAA 2007-0877 (2007), jan

[Obe12] Oberleithner, K.: On Turbulent Swirling Jets: Vortex Breakdown, Coherent Structures, and their Control, TU Berlin, Diss., 2012

[OCP06] Orlov, Dmitry M. ; Corke, Thomas C. ; Patel, Mehul P.: Electric Circuit Model for Aerodynamic Plasma Actuator. In: 44th AIAA Aerospace Sciences Meeting and Exhibit, Reno, Nevada AIAA 2006-1206 (2006), Januar

[ONL+07] Opaits, D.F. ; Neretti, G. ; Likhanskii, A.V. ; Zaidi, S. ; Shneider, M.N. ; Miles, R.B. ; Macheret, S.O.: Experimental Investigation of DBD Plasma Actuators Driven by Repetitive High Voltage Nanosecond Pulses with DC or Low-Frequency Sinusoidal Bias. In: 38th AIAA Plasmadynamics and Lasers Conference, Miami, FL AIAA 2007-4532 (2007), jun

[OSN+11] Oberleithner, K. ; Sieber, M. ; Nayeri, C.N. ; Paschereit, C.O. ; Petz, C. ; Hege, H.-C. ; Noack, B.R. ; Wygnanski, I.: Three-dimensional coherent structures in a swirling jet undergoing vortex breakdown: stability analysis and empirical mode construction. In: Journal of Fluid Mechanics 679 (2011), S. 383–414

[PAC+08] Porter, C. ; Abbas, A. ; Cohen, K. ; McLaughlin, T. ; Enloe, C.L.: Spatially Distributed Forcing and Jet Vectoring with a Dielectric Discharge Plasma Actuator. In: 46th AIAA Aerospace Sciences Meeting and Exhibit, Reno, NV AIAA-2008-1374 (2008)

[PC03] Post, M.L. ; Corke, T.C.: Separation Control on High Angle of Attack Airfoil Using Plasma Actuators. In: 41st Aerospace Sciences Meeting and Exhibit, Reno, NV AIAA-2003-1024 (2003), Nr. AIAA 2003-1024

[PC04a] Post, M.L. ; Corke, T.C.: Separation Control on High Angle of Attack Airfoil Using Plasma Actuators. In: AIAA Journal 42 (2004), November, Nr. 11, S. 2177–2184

[PC04b] Post, M.L. ; Corke, T.C.: Separation Control Using Plasma Actuators – Dynamic Stall Control on an Oscillating Airfoil. In: 2nd AIAA

Flow Control Conference, Portland, Oregon AIAA 2004-2517 (2004), Juni. – scan

[PM00] Pelletier, A. ; Mueller, T.J.: Low Reynolds Number Aerodynamics of Low-Aspect-Ratio, Thin/Flat/Cambered-Plate Wings. In: AIAA Journal of Aircraft 37 (2000), Nr. 5, S. 825–832

[RD06] Roth, J.R. ; Dai, X.: Optimization of the Aerodynamic Plasma Actuator as an Electrohydrodynamic (EHD) Electrical Device. In: 44th AIAA Aerospace Sciences Meeting and Exhibit AIAA 2006-1203 (2006), jan

[RH72] Reynolds, W.C. ; Hussain, A.K.M.F.: The mechanics of an organized wave in turbulent shear flow. Part 3. Theoretical models and comparisons with experiments. In: Journal of Fluid Mechanics 54 (1972), S. 263–288

[Rom08] Romann, D.: Plasma Calibration Studies, ISTA, Berlin Institute of Technology, Diplomarbeit, 2008

[Ros55] Roshko, A.: On the wake and drag of bluff bodies. In: Journal of Aerospace Science and Technologies 22 (1955), S. 124–132

[RV12] Rizzetta, D.P. ; Visbal, M.R.: Plasma FlowControl Simulations of a Low-Reynolds Number Low-Aspect-Ratio Wing. In: 50th AIAA Aerospace Sciences Meeting including the New Horizons Forum and Aerospace Exposition, Nashville, Tennessee AIAA 2012-1138 (2012)

[SAMT07] Sosa, R. ; Artana, G. ; Moreau, E. ; Touchard, G.: Stall control at high angle of attack with plasma sheet actuators. In: Experiments in Fluids 42 (2007), S. 143–167

[SG06] Schlichting, H. ; Gersten, K.: Grenzschicht-Theorie. 10th. Springer, 2006

[SGP08] Schüle, C.Y. ; Greenblatt, D. ; Paschereit, C.O.: Combined Plasma and Gurney Flap Flow Control at Very Low Flight Reynolds

Numbers. In: International Conference on Jets, Wakes and Separated Flows (ICJWSF), Berlin, Germany (2008)

[Sig95] Sigurdson, L.W.: The structure and control of a turbulent reattaching flow. In: Journal of Fluid Mechanics 298 (1995), S. 139–165

[SJS06] Santhanakrishnan, A. ; Jacob, J.D. ; Suzen, Y.B.: Flow Control Using Plasma Actuators and Linear/Annular Plasma Synthetic Jet Actuators. In: 3rd AIAA Flow Control Conference, San Francisco, CA AIAA-2006-3033 (2006)

[SLT+08] Shyy, W. (Hrsg.) ; Lian, Y. (Hrsg.) ; Tang, J. (Hrsg.) ; Viieru, D. (Hrsg.) ; Liu, H. (Hrsg.): Aerodynamics of Low Reynolds Number Flyers. Cambridge University Press, 2008 (Cambridge Aerospace Series)

[TC09a] Taira, K. ; Colonius, T.: Effect of Tip Vortices in Low-Reynolds-Number Poststall Flow Control. In: AIAA Journal 47 (2009), Nr. 3, S. 749–756

[TC09b] Taira, K. ; Colonius, T.: On the effect of tip vortices in low-Reynolds-number post-stall flow control. In: 47th AIAA Aerospace Sciences Meeting Including The New Horizons Forum and Aerospace Exposition, Orlando, FL AIAA-2009-376 (2009)

[TC09c] Taira, K. ; Colonius, T.: Three-dimensional flows around low-aspect-ratio flat-plate wings at low Reynolds numbers. In: Journal of Fluid Mechanics 623 (2009), S. 187–207

[Tel81] Telionis, D.P.: Unsteady viscous flows. Springer-Verlag, 1981 (Springer series in computational physics). http://books.google.de/books?id=CTJRAAAAMAAJ. – ISBN 9783540104810

[TM01] Kapitel 7. In: Torres, G.E. ; Mueller, T.J.: Aerodynamic Characteristics of Low Aspect Ratio Wings at Low Reynolds Numbers. Progress in Astronautics and Aeronautics, Vol. 195, 2001, S. 115–141

[TRCW10] Taira, K. ; Rowley, C.W. ; Colonius, T. ; Williams, D.R.: Lift Enhancement for Low-Aspect-Ratio Wings with Periodic Excitation. In: AIAA Journal 48 (2010), Nr. 8, S. 1785–1790

[TYF07] Tropea, C. (Hrsg.) ; Yarin, A.L. (Hrsg.) ; Foss, J.F. (Hrsg.): Springer Handbook of Experimental Fluid Mechanics. Springer, 2007

[Urz03] Urzynicok, F.: Separation Control by Flow-Induced Oscillations of a Resonator, Technische Universität Berlin, Diss., 2003

[Ute10] Utehs, S.: Untersuchung zur Erzeugung einer Volumenkraft durch DBD-Plasma-Aktuatoren, Technische Universität Berlin, Diplomarbeit, 2010

[Vak90] Vakili, A.D.: Review of Vortical Flow Utilization. In: 16th AIAA Aerodynamic Ground Testing Conference AIAA 90-1429 (1990)

[VGNP10] Vey, S. ; Greenblatt, D. ; Nayeri, C.N. ; Paschereit, C.O.: Leading Edge and Wing Tip Flow Control on Low Aspect Ratio Wings. In: 40th Fluid Dynamics Conference and Exhibit, Chicago, Illinois, June 28- July 1 AIAA-2010-4865 (2010)

[VGP11] Vey, S. ; Greenblatt, D. ; Paschereit, C.O.: LOW ASPECT RATIO WING FLOW CONTROL AT MAV REYNOLDS NUMBERS. In: 51st Israel Annual Conference on Aerospace Sciences, Tel Aviv & Haifa (2011)

[Vib12] Tuning-fork Balance. `http://www.vibra.co.jp/global/story/tuning-fork.html`. Version: Nov 2012

[VNPG12] Vey, S. ; Nayeri, C.N. ; Paschereit, C.O. ; Greenblatt, D.: On the Frequency Scaling of the Forced Flow Above a Low Aspect Ratio Wing. In: 50th AIAA Aerospace Sciences Meeting including the New Horizons Forum and Aerospace Exposition, Nashville, Tennessee AIAA-2012-317 (2012)

[VRJM08] Vorobiev, A.N. ; Rennie, R.M. ; Jumper, E.J. ; McLaughlin, T.E.: Experimental Investigation of Lift Enhancement and Roll Control Using Plasma Actuators. In: AIAA Journal of Aircraft 45 (2008), Nr. 4, S. 1315–1321

[Wil96] Williamson, C.H.K.: Vortex dynamics in the cylinder wake. In: Annual Review of Fluid Mechanics 28 (1996), S. 477–539

[WVW91] Wu, J.Z. ; Vakili, A.D. ; Wu, J.M.: Review of the physics of enhancing vortex lift by unsteady excitation. In: Progress in Aerospace Sciences 28 (1991), S. 73–131. http://dx.doi.org/10.1016/0376-0421(91)90001-K. – DOI 10.1016/0376–0421(91)90001–K

[Wyg04] Wygnanski, I.: The Variables Affecting the Control of Separation by Periodic Excitation. In: 2nd AIAA Flow Control Conference, Portland, Oregon AIAA-2004-2505 (2004)

[Zam92] Zaman, K.B.M.Q.: Effect of Acoustic Excitation on StStall Flows Over an Airfoil. In: AIAA Journal 30 (1992), S. 1492–1499

[Zim32] Zimmerman, C.H.: Characteristics of Clark Y Airfoils of Small Aspect Ratios / Langley Memorial Aeronautical Laboratory, NACA-TR-431. 1932. – Forschungsbericht